The role of relative humidity on shallow cumulus dynamics; results from a Large Eddy Simulation model

Simon Looijen Axelsen

April 6, 2005

Abstract

Shallow cumulus clouds play an important role in the vertical transport of heat, moisture and momentum in the atmosphere. However, due to their relatively small horizontal scales they cannot be resolved explicitly in climate or weather forecasting models. The mass flux parameterization is used to solve this problem. Our question is whether atmospheric relative humidity influences the cloud dynamics and hence should be incorporated in parameterizations. To this end we have used a large eddy simulation model (LES) to see how the cloud dynamics are affected when the mean atmosphere specific humidity and mean temperature profiles are changed in such a way that the mean buoyancy remains constant. We have also used the LES model to see what effect the surface fluxes of latent and sensible heat have on the cloud dynamics. In particular, we have varied these surface fluxes such that the surface buoyancy flux, to a good approximation remains identical, i.e. the convective velocity scale is identical.

Our results show that mean atmospheric relative humidity does influence the cloud dynamics. The difference in cloud mass flux between the simulations is primarily determined by the cloud fraction, which is related to the relative humidity; more moisture leads to larger cloud fractions. Cloud vertical velocities need not be scaled; they seem to have the same profiles. More humid environments lead to increased total and liquid water content, increased entrainment and detrainment rates and at the same time more turbulent kinetic energy is generated, thus the buoyancy flux is also affected. When trying to scale the latter quantity following Grant and Lock (2004) we found that the convective available potential energy (CAPE) must be submitted to severe scrutiny since CAPE is largely affected by the mean atmospheric relative humidity.

Contents

Chapter 1

Introduction

1.1 Cloud types

Foreigners coming to Holland often complain about the weather; the summer is chilly, it is often windy, but above all; it frequently rains. Personally I have noticed that during the autumn the following symbols are included in nearly every daily weather prediction: a sun, a sky and some rain. Normally I experience only two of the three weather situations during a day; forecasting the weather is obviously not that easy. Since clouds are the source of precipitation, we would like to know more about clouds, but what are they? A cloud is a visible aggregate of tiny water droplets and/or ice crystals suspended in the atmosphere and can exist in a variety of shapes and sizes. Some clouds are accompanied by precipitation; rain, snow, hail, sleet, even freezing rain. All clouds are not alike, rather they differ substantially.

There are different ways of classifying clouds. One approach refers to their appearance as seen by an observer on the ground. Another approach is based on the dynamic characteristics of clouds. Both approaches uses Latin for labeling purposes. The former classification approach divides clouds into three broad categories. Following Salby (1996), they are (i) stratiform, layered clouds, (ii) cumuliform, piled clouds, and (iii) cirriform, which means fibrous. Below the latter classification will be given, following Houze (1993). The first two cloud types mentioned are high-level clouds (cirriform clouds). Their cloud bases are normally above 6000 meters, I. The next three are found at mid-altitude ('alto' is Latin for high) II, their cloud bases appear between 2000 and 6000 meters. The remaining five have cloud bases found at low-altitude, i.e. up to 2000 meters. Note however, that cumulus and cumulonimbus can become very tall, III.

I

Cirrus: Detached clouds in the form of white, delicate filaments or white or mostly white patches of narrow bands. These clouds have a fibrous appearance, or a silky sheen, or both.

Cirrocumulus: These clouds are thin, white patches of cloud without shading and are composed of very small elements. Their arrangement is more or less regular.

II

Cirrostratus: Transparent, whitish cloud with a smooth appearance, totally or partially covering the sky.

Altocumulus: The color of this type of cloud is gray, white or something in between. They are observed as patches, sheets or layers of cloud and are often accompanied by precipitation.

Altostratus: A cloud type with uniform appearance; the color is grayish or bluish. This type of cloud is usually thin, which allows sunlight to pass through.

III

Nimbostratus: These clouds have a gray appearance, often dark, and often seen to produce rain or snow. 'Stratos' is Latin for layered; the cloud fraction is close to unity; 'Nimbos' means rain.

Stratocumulus: Again a cloud type whose cloud fraction is close to unity. They are gray or whitish or both gray and whitish.

Stratus: The clouds are generally gray and have a fairly uniform base and they may produce drizzle, ice prisms or snow grains. The cloud fraction may also be unity; the difference between stratocumulus and stratus is the cloud optical thickness $,\tau$. We are talking about stratocumulus if $3 \leq \tau \leq 23$ and for $\tau \geq 23$ we are dealing with stratus.

Cumulus: Detached clouds; the cloud fraction is low. They can vertically develop into domes or towers. A more detailed of this specific cloud type is given below, and in section 2 dynamics of cumuli are explained.

Cumulonimbus: These are dense clouds with a considerable vertical extent in the form of a mountain or huge tower. Parts of their upper portion is usually smooth and nearly always flattened. Because of high wind speeds at high altitudes, the clouds will be formed like an anvil. The base is generally very dark and is frequently ragged. This type of cloud is associated with powerful thunderstorms called supercells.
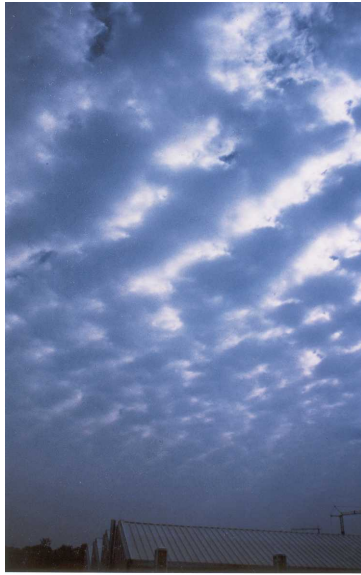
Figure 1.1: Stratocumulus. Taken from http://copernic.udg.es.

1.2 Different clouds in Hadley circulation

Figure 1.2 shows a schematic of the Hadley circulation, which is important in climate studies. Discussing this circulation is out of the scope of this thesis; instead we will for reasons given in section 1.3 turn our attention to two of the three cloud types observed in the Hadley circulation, the cumulus types.

If we subdivide cumuli into two categories by their roots, we count two classes. The idea is as follows: say a parcel ascends undiluted from the surface layer and at some point the parcel forcing exceeds a threshold value*, then deep or shallow convection is initiated. If this criterion is not met, the cumulus cloud must originate from higher levels. The second class thus represents mid-level convection.

The second class, *mid-level convection*, have their roots not in the boundary layer but originate at levels above the boundary layer, often occurring in rain bands at warm fronts and in the warm sector of extratropical cyclones. These convective cells are probably formed by the lifting of low level air until it becomes saturated and the primary moisture source for the clouds is from low-level large-scale convergence (Houze *et al.*, 1976). Often a low-level temperature inversion exists that inhibits convection from starting freely from the surface and therefore convection seems to be initiated by lifting low-level air dynamically to the

---

*For details see www.ecmwf.int/research.

5

Figure 1.2: Schematics of the Hadley circulation.

level of free convection.

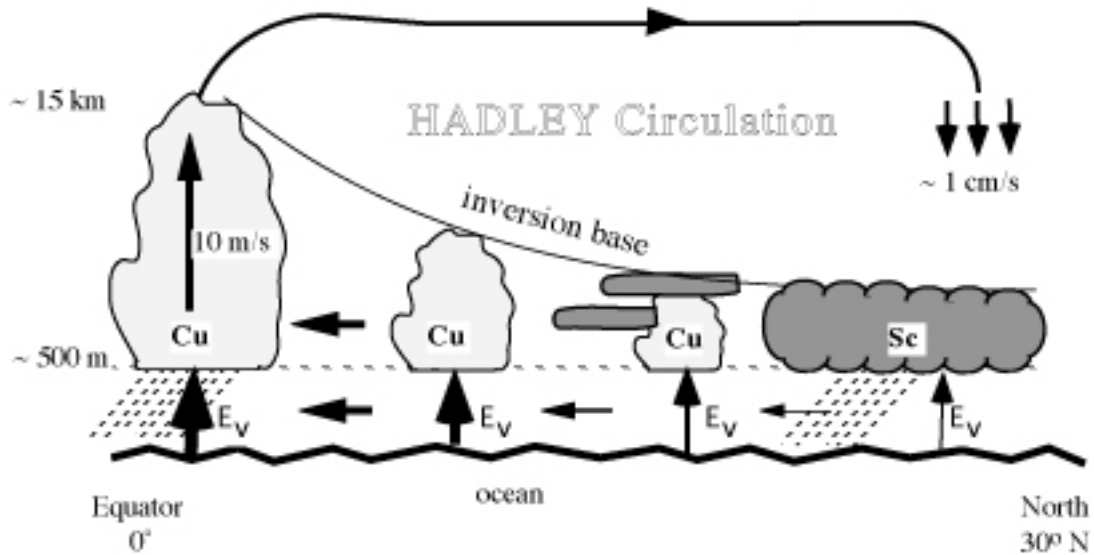*Deep convection*, i.e. deep cumuli, are formed where equatorward flows of latent heat meet. This zone is called the Intertropical Convergence Zone (ITCZ). In this area the clouds can reach heights of more than 10km and these clouds consist for a substantial part of ice particles. Deep cumuli are important in supplying energy to the Hadley circulation.

Shallow cumuli predominantly occurs in undisturbed flow, i.e. in the absence of large-scale convergent flow. Typical examples are trade-wind cumuli under a subsidence inversion, convection occurring in the ridge region of tropical easterly ways. Besides the presence of shallow cumuli in the trade-wind region they can be observed over land during the day-time. This type of convection is effectively controlled by subcloud layer turbulence. In fact, most of the diagnostic studies carried out for trade-wind cumuli show that the net upward moisture flux at cloud base level is nearly equal to the turbulent moisture flux at the surface (Tiedtke, 1989, section 3d). Shallow cumuli enhance vertical transport of heat and moisture, which again is important in large-scale atmospheric dynamics in areas above the oceans. Heat and moisture, in turn, are transported by the trade winds into the ITCZ. Here the moisture is released as latent heat and acts as a building block for deep convection, e.g. Siebesma and Holtslag (1996). Shallow cumulus clouds are the most abundant of all tropical clouds (Johnson *et al.*, 1999), and in the subtropics a sizable fraction of stratocumulus are also underlain and sustained by shallow cumulus convection (Norris, 1999). In terms of climate, the most important role of the cloud layer and its associated turbulent circulations is in buffering interactions between the surface and free

6

atmosphere (Siebesma *et al.*, 2003). Shallow cumuli are locally also of importance; the large-scale subsidence has a drying and warming effect on the boundary layer, which is counteracted by cumuli vertical mixing (Siebesma, 1998; Grant and Lock, 2004).

Tiedtke (1989) distinguished between deep and shallow convection based on moisture convergence and surface evaporation. The distinction has been modified to state that convection is deep if the cloud depth exceeds 200 hPa, and otherwise shallow.

1.3 Focus on shallow cumuli

It is well known that humidity plays an important role in the dynamics of deep cumuli and in stratocumulus. Siebesma and Cuijpers (1995) compared fractional entrainment and detrainment rates (see section 2.4) obtained from large eddy simulation (LES) studies with those used in general circulation models (GCM) and found that the latter models used fractional entrainment and detrainment rates being one order of magnitude too small. Changes were implemented, but still fractional rates are prescribed as either being constant or being a constant at the cloud base and then slightly changes linearly with height. Such a parameterization can be improved.

Derbyshire *et al.* (2004) were the first to evaluate the sensitivity of cumulus convection to humidity in the free troposphere by using cloud resolving models (CRMs). They compared results with single column models (SCMs), hence their humidity profiles were chosen such that intercomparison would be possible, yet realistic. To the best of our knowledge, such sensitivity tests have not yet been carried out for shallow cumulus.

Based on the works of Grant and Brown (1999), Grant and Lock (2004) proposed for the buoyancy flux in the cloud layer a scaling based on CAPE, the mass flux at the cloud base and the cloud depth[†]. However, the effects of humidity are not incorporated, but as we will show, humidity plays a role on the dynamics of clouds.

1.3.1 Research aim

The aim of this research is to better understand how atmospheric relative humidity affects the entrainment rate in shallow cumuli. We hypothesize that

1. The relative humidity is important as one can argue that in a drier atmosphere the breakup of clouds will be more rapid and formation of clouds will be suppressed.

[†]See sections 2.3 and 3.5

2. The surface moisture flux is important since it is reasonable to assume that changes in this property determines how much condensational heat can be released.

3. Based on our simulations, which should bring insight into the two above mentioned arguments, we will try to figure out if the scaling proposed by Grant and Lock (2004) works and try to figure out why (not).

In the remainder of this thesis we will discuss cumulus cloud dynamics and how they are treated in GCMs (section 2). In section 3.1 the LES model is discussed followed by some notes on BOMEX, which serves as our reference case. In chapter 4 the setup of the sensitivity studies are presented with results, and in chapter 5 we discuss some results. Finally, in chapter 6 the conclusions are summarized and recommendations are given. This thesis makes vast use of classical thermodynamics, which is given in appendix A. The governing equations as used in the LES model are explained in detail in appendix B.

Chapter 2

Cumulus

In this section we will turn our attention to cumulus cloud dynamics. We desire to give a non-mathematical description, but concepts such as stability and buoyancy can only be understood with the aid of thermodynamics. Readers familiar with such can go to section 2.2.

2.1 Variables and equations

In appendix A and B the variables, governing equations and some derivations are described in detail. Below we list the variables frequently used in the remainder of this thesis.

Consider a control volume consisting of a mixture of dry air and water vapor. Ice particles could also be included but they are not abundant in shallow cumulus clouds and will therefore be excluded in this study. The ratio of the water vapor to the total mass is called the water vapor content and is denoted by q_v. Similar ratios can be defined for liquid water content and total water content, q_l and q_t, respectively. The latter quantity is the sum of liquid water content and water vapor, $q_t = q_v + q_l$.

To incorporate the effect of moisture on the density, the virtual temperature, T_v, is often used.

$$T_v = T[(1 - (1 - \frac{R_d}{R_v}q_v) - q_l]^* \quad . \tag{2.1}$$

The virtual temperature is the temperature that dry air must have to equal the density of moist air at the same pressure. For instance, unsaturated moist air is less dense than dry air at the same temperature and pressure, resulting in a higher virtual temperature.

The temperature of an air parcel changes when displaced vertically; pressure effects cause

---

*See appendix B for definitions of c_p, R_d and R_v

the parcel to expand or compress. For this reason meteorologists also work with potential temperature, which is defined as the temperature an air parcel would have if it were expanded or compressed adiabatically from its existing pressure to a reference pressure. An adiabatic process is a process in which there is no heat exchange between a parcel and its surrounding. Mathematically the potential temperature and the virtual potential temperature are written

$$\theta = T \left(\frac{p_0}{p} \right)^{R_d/c_p} \quad \text{and} \quad \theta_v = T_v \left(\frac{p_0}{p} \right)^{R_d/c_p} \quad . \tag{2.2}$$

The reference pressure, p_0, is generally taken as 1000 hPa, which is the pressure near the earth's surface. In addition, we shall use the liquid potential temperature, which on approximated form reads

$$\theta_l = \theta - \frac{l_v q_l}{c_p \Pi} \quad \text{where} \quad \Pi = \left(\frac{p}{p_0} \right)^{R_d/c_p} \quad , \tag{2.3}$$

ℓ_v and c_p are the latent of evaporation and heat capacity at constant pressure, respectively. The strength of the liquid potential temperature is that it for adiabatic processes is conserved, even under phase transformation.

2.2 A cumulus cloud is born

Let us first start by looking at how shallow cumulus clouds develop. In absence of precipitation, these clouds are also referred to as fair-weather cumulus.

It is commonly known that lighter fluids lay on top of heavier ones. When air near the earth's surface due to solar warming or stronger evaporation becomes warmer or moister than the atmosphere above, its density will be lower than the air above it. So-called thermals will start rising from the surface. A thermal is in fact a large eddy. How far a thermal will rise depends on the density of the surrounding air. The environment, which is just the ambient air, has a density which is determined by temperature and moisture. One variable that incorporates both temperature and moisture is the virtual temperature, T_v. We will now in two regions have a look at an unsaturated air parcel ascending from the surface. The first region is the subcloud layer; we assume that the parcel is ascending adiabatically, i.e. no mixing with the environment. We also assume that the air parcel immediately adapts to the new pressure. It is straight forward to choosing a temperature and water vapor content for a parcel such that the parcel has a lower virtual temperature than the environment,

i.e. being denser, and whereby its ascent is suppressed. This is an uninteresting case; we shall rather focus on the case where the parcel's virtual potential temperature exceeds that of the environmental. At the surface the particle will start ascending, following the dry adiabatic temperature lapse rate, Γ_d. The temperature lapse rate is simply the rate of change of temperature with respect to height[†]. When the environmental virtual potential temperature lapse rate becomes positive, the parcel's virtual potential temperature will equal the environmental virtual potential temperature at some point. In figure 2.1 the virtual potential temperature of the air parcel is plotted along with virtual potential temperature of the environment. Before we continue the discussion on the rising air parcel, please note the following: Firstly, in a stably stratified atmosphere the virtual potential temperature increases with height. At night there is no input from the sun, rather energy is emitted by means of longwave radiation. This ensures that the heaviest air remains at the surface, which is a stable stratification. Secondly, if the atmosphere is unstable, i.e. if the atmosphere is top-heavy, the virtual potential temperature decreases with height. This is the case during day time when air close to the ground is more rapidly warmed up by the sun. Finally, we say the atmosphere is vertically well mixed if the virtual potential temperature is approximately constant with height. The different layers are sketched in figure 2.1. Figure 3.5 also depicts the three different cases.

Let's now return to our ascending parcel. If the virtual potential temperature of the environment and parcel are equal, the parcel is said to be neutrally buoyant. This level is referred to as the 'level of neutral buoyancy' (LNB). At this stage the particle has no preferred vertical direction. Well, that is not completely true; during its ascent the parcel has obtained vertical momentum, i.e. it shoots through the LNB. Its virtual potential temperature has become less than that of the environment, and its vertical ascent is therefore forced to a halt. The area in which the parcel now is, is called the convective inhibition (CIN), see figure 2.3. However, if its vertical velocity is sufficiently large it reaches the height at which the water vapor pressure equals the saturation pressure and becomes saturated[‡]. This level is called the lifting condensation level (LCL) and denotes the base of the cloud; the parcel has now become a cloud parcel. The rising air parcel has reached the second region; the cloud region. The virtual potential temperature for an ascending *saturated* parcel is not constant with height because phase change takes place. Moist air condenses whereby heat is released, which is why the θ_v lapse rate increases with height.

[†]In this report the lapse rate of a quantity ψ is given by $\Gamma_\psi = -\frac{\partial \psi}{\partial z}$.

[‡]A parcel becomes saturated when the partial water vapor pressure, e equals the saturation pressure, e_{sat}, i.e. $e/e_{sat} = 1$. The latter equation can be approximated by $q_v/q_{sat} = 1$ where q_v and q_{sat} are the specific humidities for water vapor and saturated vapor, respectively
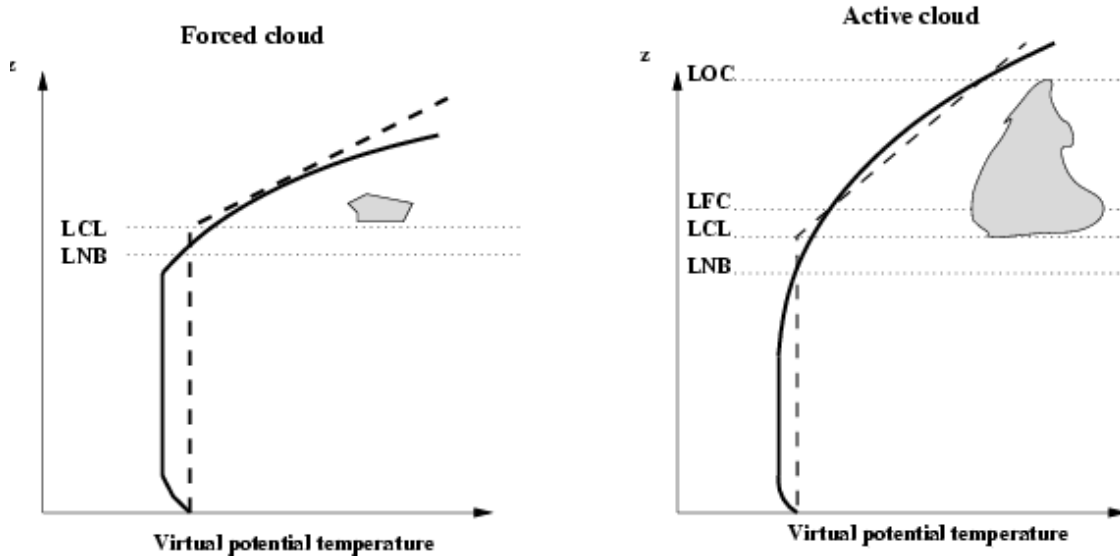
Figure 2.1: Depiction of a forced and an active cloud. In both cases the environment (fine line) is just above the surface unstably stratified and then vertically well mixed. In the situation on the left, above the mixed layer a stable stratification is found. In the right panel above the well mixed layer is a conditionally unstable layer, i.e. the mean lapse rate of the rising parcel is larger than the environmental lapse rate and smaller than the wet-adiabatic lapse rate. Before reaching the conditionally unstable layer, the virtual potential temperature is conserved following a dry adiabatic lapse rate but this changes when the parcel the lifting condensation level (LCL). At this level clouds form and heat due to condensation is released, not to the environment, rather the heat is kept within the parcel causing it to be warmer than the environment. In the domain between the the limit of convection (LOC) and level of free convection (LFC) the parcel has a higher virtual potential temperature than the environment. This virtual potential temperature excess leads to production of vertical momentum. At the LOC the θ_v of the parcel and environment are once more equal. LOC defines the top of the conditionally unstable layer.

The wet adiabatic lapse rate is also shown in figure 2.1. Note that the wet-adiabatic lapse rate, applies to a parcel that does not mix with its environment and that the total water content, q_t, and the liquid potential temperature, θ_l, therefore are assumed constant. The further evolution depends on the environmental lapse rate:

If the wet-adiabatic lapse rate of the environment is larger than that of the parcel, the parcel will at all levels above LNB remain heavier than its surroundings and finally it will start sinking. The resulting cloud is called a forced cloud and the atmosphere is absolutely stable.

If on the other hand the lapse rate of the environment at some height is smaller than

the parcel's lapse rate, the parcel will again be positively buoyant. The requirement for getting to this level, called the level of free convection (LFC), is that the parcel has gained sufficient vertical momentum when it rose from the LNB to the LFC. The parcel is now lighter than its surroundings and is free to ascend further. However, this cannot go on forever; at the limit of convection (LOC) the parcel is again neutrally buoyant. It can again overshoot this level and enter the inversion layer. This is the boundary layer's "lid" and is very stable. The level at which the parcel again starts to descend dictates the cloud top. A cloud formed following the second description is called an active cloud.

What it all boils down to, is whether the rising parcel keeps ascending as a consequence of being positively buoyant with respect to the environment. It can be shown that this is the case if the lapse rate of the particle is larger than the wet adiabatic lapse rate and at the same time less than the dry adiabatic lapse rate.

Cumulus clouds are patchy clouds, like plumes rising in the skies. The amount of time the ascending parcel can remain in a free convective state, i.e. how long it can continue to rise, depends on the forcing of the thermal. The closer to the equator the larger the forcing. The tallest cumulus clouds are found at these latitudes. However, according to the classification above, such tall clouds are no longer called cumulus but cumulonimbus. This is due to the fact that their vertical sizes are well beyond the typical boundary layer depth.

The patchy structure implies that the mean relative humidity (RH), which is defined as the ratio of the actual water vapor pressure to the saturation vapor pressure, is below 100 per cent[§]. To see this, picture a control volume containing some cumulus clouds. Inside the clouds RH=100%, but since averaging over the control volume implies counting in areas with no clouds, the relative humidity is lowered.

2.3 Convective Available Potential Energy (CAPE) and buoyancy

Cumulus clouds do not only consist of ascending cloud parcels. In the core of the cumulus cloud the parcels are ascending due to the fact that they are positively buoyant. The buoyancy force is the force arising from the fact that the cloud parcel is lighter than its

---

[§]$e/e_{sat} \approx q_v/q_{sat} < 1$

Figure 2.2: Cumulus. Taken from www.capetownskies.com.

surroundings and is normally given by

$$b = g\frac{\theta_{v,\text{core}} - \overline{\theta_v}}{\overline{\theta_v}} \quad ,$$

where $\theta_{v,\text{core}}$ and $\overline{\theta_v}$ denote the parcel's and the slab averaged virtual potential temperatures, respectively. The convective available potential energy (CAPE) is used to estimate the vertical velocity at the cloud top, as obtained through acceleration throughout the cloud. Holton (1992) describes CAPE as follows: *CAPE provides a measure of the maximum possible kinetic energy that a statically unstable parcel can acquire (neglecting effects of water vapor and condensed water on the buoyancy), assuming that the parcel ascends without mixing with the environment and instantaneously adjusts to the local environmental pressure.*

CAPE, denoted by an A, is given by the vertical integral of the buoyancy force, bounded by limits between which the buoyancy force is positive, see the striped area in figure 2.3. Mathematically, CAPE is given by

$$A = \frac{g}{\overline{\overline{\theta_v}}} \int_{\text{LCL}}^{\text{LOC}} (\theta_{v,core} - \overline{\theta_v}) dz \tag{2.4}$$

CAPE represents conversion of potential energy into kinetic energy; the typical velocity scale, w_{CAPE}, can be defined by assuming that all the potential energy is converted into kinetic energy. Often (e.g. Holton, 1992) the following definition is used:

$$w_{CAPE} = (2 \cdot CAPE)^{1/2} \tag{2.5}$$

14
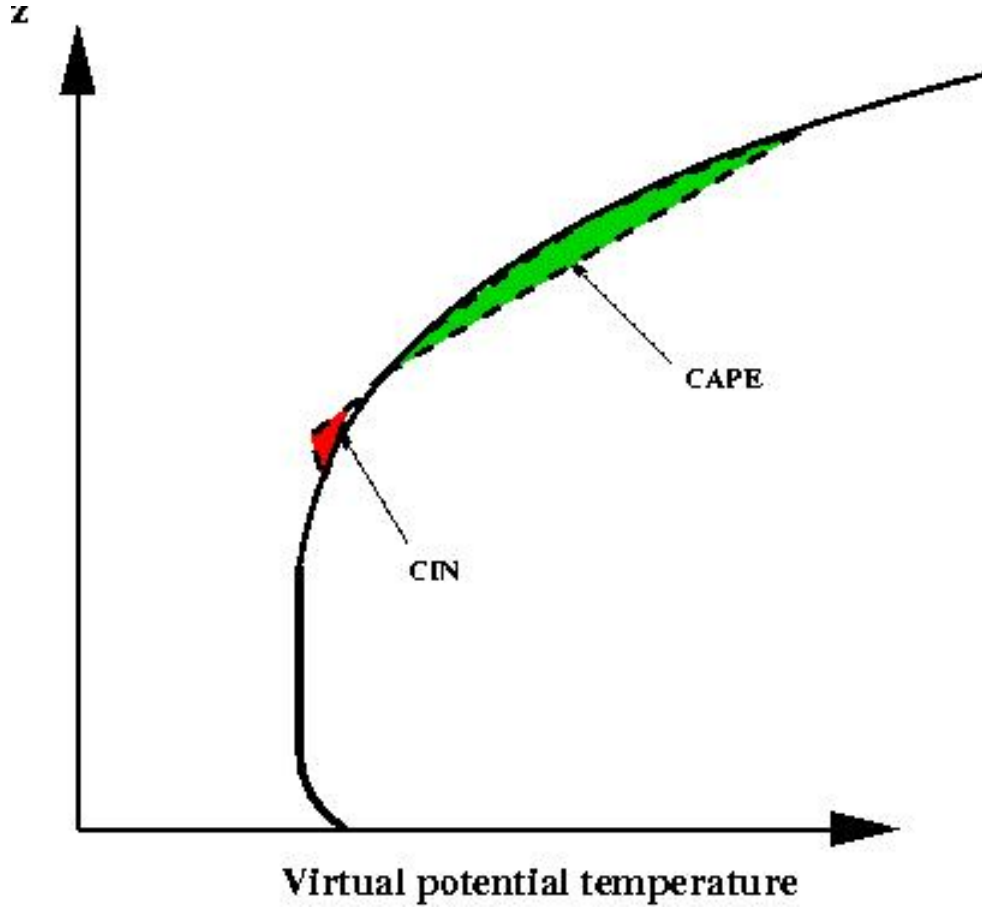
Figure 2.3: The virtual potential temperature for an adiabatically rising parcel (dashed) and its environment (solid). The striped and dotted areas denote CAPE and CIN, respectively.

This can readily be derived from the following

$$\frac{\mathrm{d}w}{\mathrm{d}t} = w\frac{\partial w}{\partial z} = \frac{\partial(\frac{1}{2}w^2)}{\partial z} = b \Rightarrow$$
$$\frac{1}{2}w^2 = Bdz \quad .$$

Here we assume $\partial/\partial t = 0$ and no horizontal advection of vertical velocity. Instead of integrating to the limit of convection (LOC), we can integrate to any arbitrary height $\tilde{z}$, yielding the vertical velocity scale at that height.

$$w_{\tilde{z}} = \sqrt{2A} \quad . \tag{2.6}$$

So far we have looked at undiluted cloud particles, whose trademark is that they are positively buoyant. Paluch (1979) argued that mixing of cloud and environmental air

15

happens at the cloud top, but more recently Raga *et al.* (1990) have showed that lateral mixing occurs at all levels across the cloud boundaries. At the cloud edge cloud particles thus may mix with the environment and loose their buoyancy. When mixing, particles undergo evaporative cooling and may even become negatively buoyant with respect to the clear environment, which is termed 'buoyancy reversal'. Bretherton *et al.* (2003) shows that for a conditionally unstable atmosphere, mixing fractions[¶] exist for which mixed parcels will be negatively buoyant with respect to the environment. Lateral mixing of cloud air with the environment makes the CAPE approximation less useful.

2.4   Cumuli in General Circulation Models

In operational weather prediction models and climate models, hereafter referred to as general circulation model (GCM), typical grid distances vary between 10 and 100 km. The maximum horizontal length scale for cumuli, on the other hand, is of the order of a kilometer. Obviously, the resolution of GCMs is too coarse and the solution is to parameterize cumulus clouds in GCMs. This means for instance that instead of explicitly calculating the cloud fraction, reflected radiation etc, some (empirical) formula fitted to the observations is used. Different types of parameterizations have been proposed; the way we will follow, is the massflux approach as used by Siebesma and Cuijpers (1995) and Bretherton *et al.* (2003). This involves coupling a simple cloud model to an algorithm for specifying an upward massflux through the cloud base. The latter authors investigated to which extent this approach is valid. The basic assumption behind the massflux approach is that the vertical turbulent transport can be described in terms of cumulus updrafts and compensating environmental subsidence.

The vertical turbulent flux of an arbitrary field ψ can be split into three parts

$$
\begin{aligned}
\overline{w'\psi'} = {} & \sigma(1-\sigma)(w_c - w_e)(\psi_c - \psi_e) \\
& + \sigma\overline{w''\psi''}^c \\
& + (1-\sigma)\overline{w''\psi''}^e \quad .
\end{aligned}
\tag{2.7}
$$

$0 \leq \sigma \leq 1$ is the cloud fraction and w_c and w_e are the vertical velocities of the cloud and environment, respectively. The overbar denotes slab-averaging over the entire domain or, with superscript, over the cloud (environment). The last two term represents the sub-plume fluxes; they are due to the contributions of perturbations with respect to the conditionally

---

[¶]The mixing fraction χ defines the ratio of the environmental air m_e to the total air mass $m_c + m_e$, i.e. $\chi = m_e/(m_c + m_e)$

sampled mean (see section C).

The massflux is now defined as

$$M_c \equiv \sigma(w_c - \overline{w}) = \sigma(1 - \sigma)(w_c - w_e) \quad . \tag{2.8}$$

More formally, the massflux should be multiplied by the density of air but since the density in the planetary boundary layer is approximately constant we will for the sake of notation leave it out.

As stated above, what goes up inside the cloud must come down on the outside. This is ensured by the continuity equation, which for the massflux is given by

$$\frac{\partial M_c}{\partial z} = -\frac{\partial \sigma}{\partial t} + E - D \quad . \tag{2.9}$$

Here E and D are the lateral entrainment and detrainment rates, respectively. The fractional entrainment and detrainment rates, ϵ and δ are respectively given by

$$\epsilon = \frac{E}{M_c} \quad \text{and} \quad \delta = \frac{D}{M_c} \quad .$$

Lateral entrainment is defined as a one-way process in which environmental air is laterally entrained into the updraft at some specified rate per unit height, regardless of the buoyancy of any intermediate mixtures produced (Arakawa and Schubert, 1974). In the massflux approach the tendency equation for the mean of an in-cloud quantity, ψ_c, can be written

$$\frac{\partial(\sigma \psi_c)}{\partial t} = -\frac{\partial(M_c \psi_c)}{\partial z} + E\psi_e - D\psi_c + \sigma S_{\psi,c} \quad , \tag{2.10}$$

where $S_{\psi,c}$ is a source / sink term. Assuming that the source / sink term is zero, $S_{\psi,c} = 0$, that the temporal change of the in-cloud mean is very small, $\partial(\sigma \psi_c)/\partial t \approx 0$, and that in equation (2.9) the cloud fraction does not change with time, $\partial \sigma/\partial t = 0$, we can obtain the following two expressions for the fractional entrainment and detrainment rates, respectively

$$\frac{E}{M_c} \equiv \epsilon = -\frac{\partial \psi_c/\partial z}{\psi_c - \psi_e} \tag{2.11}$$

which when inserted in equation (2.9) and assuming $\partial \sigma/\partial t = 0$ yields

$$\frac{D}{M_c} \equiv \delta = \epsilon - \frac{\partial \ln M_c}{\partial z} \tag{2.12}$$

Several entrainment parameterizations based upon some form of the cloud kinetic energy budgets have been proposed. Grant and Brown (1999) suggested to use the following fixed entrainment rate for the whole cloud layer

$$\epsilon = C_E \frac{A}{M_b Z_{cld}}$$

17

where C_E represents the fraction of the TKE production that is available for entrainment. $C_E \in [0,1]$ is a constant to be determined and M_b is the massflux at the cloud base, and A is the convective available potential energy. By using the Met Office Large Eddy Simulation (LES) model, they found a typical value for C_E to be 0.03. Results from LES simulations show, however, that C_E decreases with height. Siebesma (1997) suggested to write the fractional entrainment rate as

$$\epsilon = \frac{1}{w_c} \left(\frac{\partial w_c}{\partial z} \right)$$

which is derived from the mass-continuity equation and ignores variations in density and assumes the cloud fraction to be constant with height. Gregory (2001) suggested to parameterize the entrainment rate in the following way:

$$\epsilon w_c^2 = C_\epsilon a g \overline{\left[\frac{T_c - T_e}{T_e} - q_l \right]}^c$$

where a is a constant.

Siebesma *et al.* (2004) discuss problems in transferring findings of Single Column Models (SCM) / Cloud Resolving Model (CRM) / Large Eddy Simulation (LES) studies to GCMs. The problems are partly due to the fact that feedback processes may be switched off in SCMs/CRMs/LESs and that the latter use prescribed large-scale conditions that may be non-representative for both the real and model atmospheres.

Next, the GCMs may give faulty results. For instance, Siebesma *et al.* (2004) reports that for longwave radiation in some of the models involved in EUROCS[||] under-predict both cloud fraction and cloud amount in the stratocumulus regions while the situation is opposite in the trade wind region and the tropics where cloud fraction and cloud amount are over-predicted by most models. This illustrates why parameterizations need to be improved and we hope that our research can help the improvement progress.

[||]EUROpean Cloud Systems Study, see also www.knmi/samenw/eurocs

Chapter 3

A Large Eddy Simulation Approach to BOMEX

3.1 Large Eddy Simulation

As mentioned in the introduction, thermals have different length scales, ranging from the Kolmogorov microscale $O(1\text{mm})$ to the scale of the boundary layer $O(1\text{km})$. In an ideal world, the governing equations could be simulated using direct numerical simulation (DNS). However, that requires $1000 \cdot 1000 \cdot 1000^{1000} = 10^{15}$ gridpoints (x-direction $\times$ y-direction $\times$ depth) for simulating a column of air with unit area and a height of 1 km. Even the best computers in the world are incapable of performing such a simulation. The solution is to look at large-scale eddies. As it turns out that, in general, turbulent flows distinguish themselves by the specific structure of the larger scale eddies because those large scale eddies are sensitive to their particular environment and especially to the buoyancy forcing. Moreover, they are responsible for the bulk of the transport of heat, momentum and moisture. The smaller scale eddies, on the other hand, are generally assumed to behave independently. The idea is thus to choose the grid spacing small enough such that the largest eddies are explicitly resolved and the small scale processes are parameterized. This method is termed Large Eddy Simulation (LES).

3.1.1 Notation

From cloud data, either numerical or from observations, usually a slab-averaged mean and a in-cloud mean are computed. To better understand the difference, imagine that we sample values for a quantity ψ inside and outside a cloud. For $\psi = w$ this is pictured in figure 3.1;

19

the mean vertical velocity inside the cloud, w_c, is different from the mean vertical velocity of the environment, w_e. Perturbations with respect to the mean in-cloud value are denoted
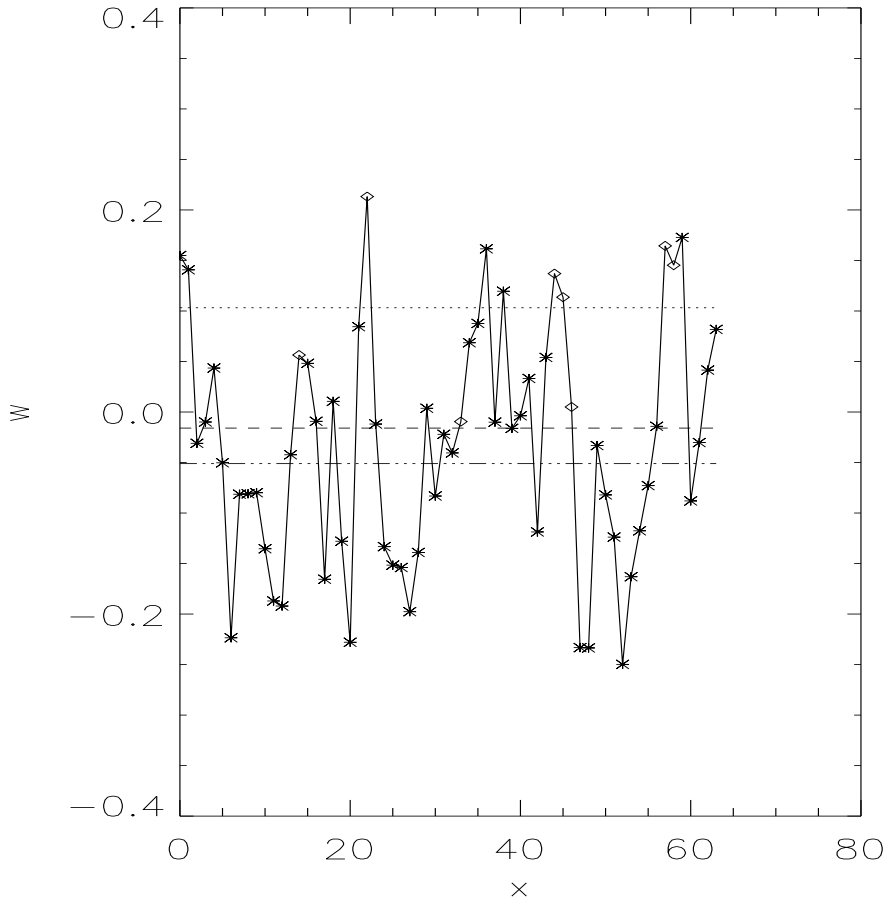

Figure 3.1: An example of the vertical velocity field at one height, and one latitude only. Data are from our LES simulation of BOMEX (see below). Cloud points are denoted by diamonds, environment point by stars. The dotted line is the cloud-mean vertical velocity, the dotted-dashed line is the environmental mean and the dashed line is the slab-averaged value. Note that in order to show a two dimensional plot we had to choose one single latitude. This implies that averaged values are not slab-averaged, rather latitudinally averaged (in contradiction to normal .

by w'', and w' denotes deviations with respect to the slab-averaged mean.
We distinguish between resolved and subgrid scales. The resolved part of an arbitrary variable ψ is denoted by $\langle \psi \rangle$; subgrid terms are denoted by a double prime. Only fluxes

have subgrid component. Slab-averaged fluxes are denoted by an overbar. With this
notation, the horizontally averaged vertical flux at an arbitrary height, is given by

$$\overline{w'\psi'} = \frac{1}{N_x N_y} \sum_i^{N_x} \sum_j^{N_y} \left(w_{ij} - \overline{w}\right)\left(\psi_{ij} - \overline{\psi}\right)$$

where the summation is performed over a horizontal plane with $N_x N_y$ grid points and the
indexes i, j denote the respective values of w and ψ at the gridpoints.

3.1.2 Equations

After having discussed different variables, we have finally arrived at our most important
tools; the governing equations. They are explained in detail in appendix B. The filtered
LES equations are

$$\frac{\partial \langle \psi \rangle}{\partial t} + \frac{\partial (\langle u_i \rangle \langle \psi \rangle)}{\partial x_i} = -\frac{\partial \langle u_i'' \psi'' \rangle}{\partial x_i} + S_\psi \tag{3.1}$$

$$\frac{\partial \langle u_i \rangle}{\partial t} + \frac{\partial (\langle u_i \rangle \langle u_j \rangle)}{\partial x_j} = g \frac{\langle \theta_v \rangle - \overline{\theta_v}}{\overline{\theta_v}} \delta_{i3} - \frac{\partial \langle \pi \rangle}{\partial x_i} - \frac{\partial \tau_{ij}}{\partial x_j} \quad . \tag{3.2}$$

where $\langle u_i'' \psi'' \rangle$ indicate correlations due to fluctuations on subgrid scales, i.e. scales smaller
than the grid distance. In equation (3.1) ψ can represent the total water specific humidity
q_t, or the liquid water potential temperature θ_l. u_i are the three components of the velocity
vector $\vec{u} = (u, v, w)$, π is the modified pressure, τ_{ij} the stress tensor, g is the gravitational
constant, and θ_v and $\overline{\theta_v}$ are the virtual potential temperature of a parcel and of the mean
state, respectively. Equation (3.2) is the filtered Navier-Stokes equation. Filtered means
that the equations are discretized, i.e. at each grid point for the large eddies the prognostic
equations for θ_l, q_t (u, v, w) and continuity are solved together with the ideal gas law.
Properties on the yet smaller, unresolved scales include the viscous dissipation, which is
negligible small outside the viscous sublayer near the surface. The stress tensor in equation
(3.2) is given by

$$\tau_{ij} = \langle u_i'' u_j'' \rangle - \frac{2}{3} \delta_{ij} \langle e \rangle \tag{3.3}$$

$$\langle e \rangle = \frac{1}{2} \langle u_k'' u_k'' \rangle \quad , \tag{3.4}$$

where $\langle e \rangle$ is a subgrid turbulent kinetic energy term or also called generalized subgrid
normal stresses in this case.

3.2 Closure

The purpose of using an LES model is to resolve the largest eddies and use parameterization for the smaller ones. Generally, a set of n equations can only be solved if we have n unknowns; no more, no less. When gathering information from measurement campaigns, we usually get more data than necessary; the set of equations is said to be overdetermined. If on the other hand we have less equations than variables, we need to make some approximations in order to solve the set of equations; i.e. we make approximations in order to close the set of equations.

The last term on the right hand side of equation (3.2) is the stress tensor τ_{ij}, which needs to be parameterized and is done by first order closure:

$$\tau_{ij} = -K_m \Big(\frac{\partial \langle u_j \rangle}{\partial x_i} + \frac{\partial \langle u_i \rangle}{\partial x_j} \Big) \tag{3.5}$$

Here K_m is a scalar with units m^2s^{-1}. For positive K_m, equation (3.5) implies that the flux flows down the local gradient of u_i and u_j. This closure approximation is often called gradient transport theory or K-theory. The first term on the right of equation (3.1) represents a subgrid flux and first order closure is also applied here:

$$\langle u_j'' \psi'' \rangle = -K_\psi \Big(\frac{\partial \langle \theta_l \rangle}{\partial x_j} \Big) \quad . \tag{3.6}$$

ψ can either be one of the two conserved quantities θ_l or q_t. K_m and K_ψ are functions of position and are determined from subgrid turbulent kinetic energy (TKE) and a length scale l. The prognostic equation for the subgrid TKE is given by:

$$\frac{\partial \langle e \rangle}{\partial t} + \langle u_j \rangle \frac{\partial \langle e \rangle}{\partial x_j}$$
$$= \frac{g}{\theta_v} \langle \theta_v'' u_i'' \rangle \delta_{i3} - \tau_{ij} \frac{\partial \langle u_i \rangle}{\partial x_j} - \frac{\partial}{\partial x_j} \Big[\frac{1}{2} \langle u_i'' u_j'' u_i'' \rangle \Big] \quad . \tag{3.7}$$
$$- \frac{1}{\rho_0} \frac{\partial \langle p'' u_i'' \rangle}{\partial x_i} + \frac{\partial}{\partial x_j} \Big[\nu \langle u_i'' \frac{\partial u_i''}{\partial x_j} \rangle \Big] - \nu \Big\langle \Big(\frac{\partial u_i''}{\partial x_j} \Big)^2 \Big\rangle$$

The two terms on the left are the only terms that can be calculated directly. On the right hand side terms are closed using K-diffusion in the following way

$$\langle u_i'' \psi'' \rangle = -K_{\langle \psi \rangle} \frac{\partial \langle \psi \rangle}{\partial x_i}$$
$$K_\psi = \sqrt{\langle e \rangle} l$$

where l is a length scale often related to a representative grid mesh size, see VanZanten (2000). The turbulent kinetic energy depends on position thus does the diffusion coefficient first introduced in equation (3.5) also depend on position.
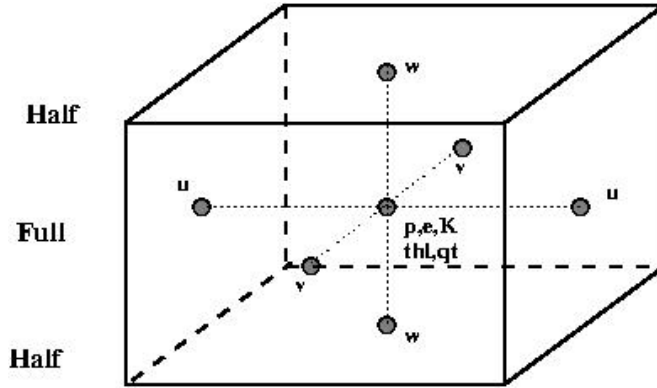
Figure 3.2: Control volume depicting where different quantities are calculated.

3.3 Numerics

The horizontal domain in our simulations is split in 64×64 grid elements and the distance between two successive grid points is 100 meters. In the vertical there is a total of 75 levels with a grid distance of 40 meters. Now consider a control volume as depicted in figure 3.2. The resolved horizontal velocity components are defined on the sides of the control volume. In the center of the grid box the resolved pressure, subgrid turbulent kinetic energy, liquid water potential temperature, the specific humidity and exchange coefficients are calculated. At the bottom of the control volume the resolved vertical velocity are computed. Quantities in the center of the box are said to be computed at full level. Half level, quantities are computed in between the full level quantities, see also figure B.1. For instance, the vertical velocity is computed at the bottom of the control volume and is thus a half-level quantity.

In numerical computations special care has to be taken for computations at the edges of the domain. For instance, when computing the horizontal gradient at the boundary, the value of a non-existing control domain is needed, see figure 3.3. One way to solve this problem is to let the domain be periodic, $\psi_{i,y_N} = \psi_{i,y_1}$, where N is the highest index in the y-direction. When imposing periodic boundary conditions, the stability criteria of the numerical computation can be found[*]. Finally, at the surface and at the model top, the resolved vertical velocity is set equal to zero. Perturbations in the mean fields propagate by means of gravity waves. These gravity waves also travel upward and to ensure that they are not artificially reflected at the model top, a sponge layer is present at the model top.

---

[*]Durran (1998) gives a thorough introduction to numerical geophysical fluid dynamics
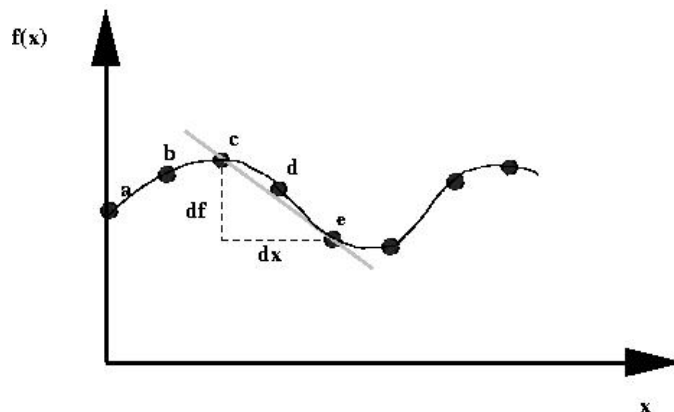
Figure 3.3: The (centered) gradient at point d is determined by df and dx computed from neighboring gridpoints. Cyclic boundary values removes the problem of constructing a gradient in point a.

3.4 Barbados Oceanographic and Meteorological Experiment

When the Barbados Oceanographic and Meteorological Experiment (BOMEX) was announced, it was unprecedented in size and sophistication and was to that date the most difficult single effort undertaken to understand the weather (Carter, 1969). It costed 18-million dollars and made use of eight satellites, 24 aircrafts, ten ships and a dozen instrumented buoys.

The experiment was a part of the Global Atmospheric Research Program (GARP) and the goal of BOMEX was to gain new understanding of the interaction of the air and tropical oceans, which is important in determining the atmospheric circulation. BOMEX aimed at investigating in detail the exchange of energy between ocean and atmosphere and the vertical and horizontal spreading of these energies. The spreading is important to understand since the earth absorbs most of its energy at low latitudes but emits energy at all latitudes. During BOMEX, which took place during May and June 1969, four ships formed the corners of an square with a perimeter of about 500 km. Observations on temperature, humidity, wind velocity, cloudiness, etc were made. In the analysis of the budgets of mass, water vapor and heat, the boundary layer up to approximately 4000 meters (700 mb) was divided into four sublayers (Holland and Rasmusson, 1973; Nitta and Esbensen, 1974). These four layers are the mixed layer, the cloud layer, the inversion layer and a layer from the inversion top to the 700 mb level. The analysis showed that under well-developed trade-

wind conditions with little cloud activity, there is horizontal divergence in mixed layer and cloud layer. The horizontal divergent layer is separated by the trade-wind inversion from a convergent layer above.

3.5 Simulation of BOMEX

Siebesma and Cuijpers (1995) used an LES model to simulate observations as obtained from the third phase of BOMEX. Averaging observations from the four ships was not feasible since the temporal and spatial variations of the fields were such that no inversion could be seen. Instead they therefore chose to simulate the mean profile of one individual ship. They used a computational domain of 6.4×6.4 km^2 in the horizontal and 3 km in the vertical. At each grid point they solved a set of prognostic equations. The variables are the three components of the velocity field $\vec{u}$, the liquid water potential temperature θ_l, the total water specific humidity q_t, and the TKE. Initial profiles from BOMEX can be found at www.knmi.nl/ siebesma/gcss/bomex.html and a thorough description of BOMEX is given by Holland and Rasmusson (1973) and Nitta and Esbensen (1974).

In our simulations we have used the same model but set the relatively small radiative forcing to zero. This change is responsible for small differences. In figure 3.4 we compare the cloud fraction and the cloud vertical velocity, the cloud decomposition has been applied. We see that the radiative forces do influence the outcome of both quantities, but the extrema are the same. In figure 3.4(b) the flucutations in the cloud top are due to the low number of statistical points.

3.6 Turbulent fluxes in cumulus cloud layers

For $i = 3$, the last term on the right hand side of equations (3.1)-(3.2) constitute the vertical fluxes of temperature, water and momentum, respectively. Let's try to picture what a flux is: say that a particle at height z_1 has a property ψ' with respect to the slab-averaged value $\overline{\psi}\big|_{z_1}$ at that height. Due to turbulent fluctuations in w', the particle may be displaced upward or downward depending on the sign of w'. If the particle is displaced upward to height z_2, it will bring with it the quantity ψ'. Unless $\psi' = \overline{\psi}\big|_{z_2}$ the mean value for ψ at height z_2 is thus changed. Before discussing the physical meaning of $\overline{w'\psi'}$, $\psi \in \{\theta, q_i, u_i\}$ we have to introduce the tendency equation

$$\frac{\partial \overline{\psi}}{\partial t} = -\frac{\partial \overline{w'\psi'}}{\partial z} + S_\psi \quad , \tag{3.8}$$

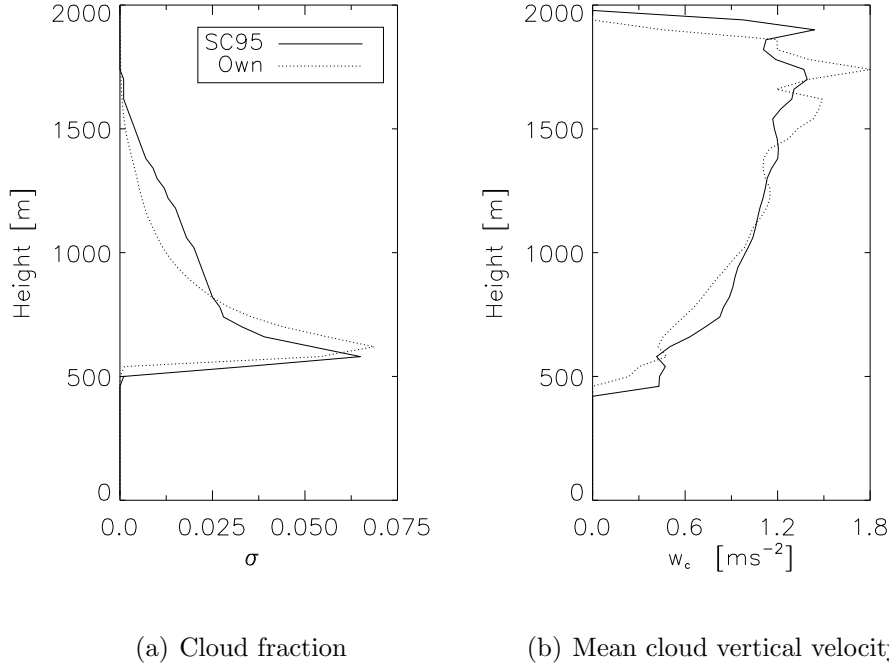(a) Cloud fraction　　　　　　(b) Mean cloud vertical velocity

Figure 3.4:　Results from Siebesma and Cuijpers (1995) compared to own results; (a) cloud fraction and (b) the cloud vertical velocities, both under the cloud decomposition. Time averaged over the third hour, see page 28 for motivation. Line styles according to legends.

where S_ψ represents the net of sources and sinks, and we have neglected mean advection. In case of no sources and sinks this equations states that the temporal change in the mean of variable ψ is related to the vertical gradient of the flux $\overline{w'\psi'}$. For instance, if the flux is positive but constant with height, then obviously what is 'lost' to heights above will also be gained from lower height. Logically this means that the net effect vanishes.

Explaining the vertical flux of potential temperature, $\overline{w'\theta'}$, is the best facilitated by using an example. In figure 3.5 three different potential temperature profiles are sketched. In the first case, a particle originating from a lower height will have the same potential temperature as the environment at its new height. If on the other hand the atmosphere is unstably stratified, the particle displaced upward will at the new level be warmer than the environment. In the last case, a cold particle is pushed up into a warmer environment. This stipulates how turbulent motion can affect the mean temperature; properties are transported from one level to another and its effect is to smoothen the temperature profiles.
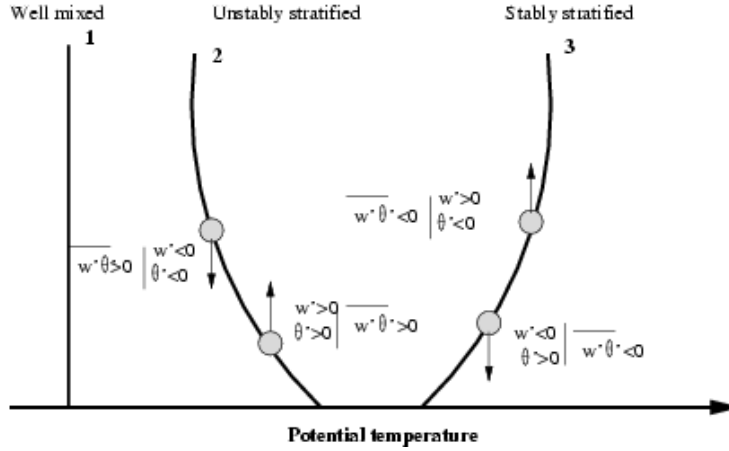
Figure 3.5: Three different temperature profiles; a well mixed (1), an unstably stratified (2) and a stably stratified (3) atmosphere.

Momentum fluxes are relevant to the subgrid TKE; the three fluxes $\overline{u_i' u_j' \delta_{ij}}$ constitute the transport of (co)variance, which is related to the subgrid TKE, see equation (3.4). The vertical velocity variance $\overline{w'w'}$ in clouds is larger than outside the clouds (e.g. Rodts, 2001), which implies that clouds more effectively dissipate energy.

Lastly we notice that $\overline{w'\theta_v'}$ in the subcloud layer, i.e. $q + l = 0$, has contributions from the temperature- and moisture fluxes, i.e.

$$\overline{w'\theta_v'} \approx (1 + 0.61\overline{q})\overline{w'\theta'} + 0.61\overline{\theta}\;\overline{w'q'}$$

This flux constitutes the supply of buoyancy.

Chapter 4

Setup of sensitivity experiments

In this section two different sets of simulations are described. In each set, we start by explaining the initial profiles followed by the results, which are analyzed in chapter 5.

Since the massflux is determined by the product of the mean in-cloud vertical velocity w_c, and the cloud fraction σ, we will focus on these quantities and also the quantities that determine w_c and σ. The cloud vertical velocity is well related to the buoyancy, θ_v, and likewise is the velocity variance $\overline{w'w'}$, which in the cloud layer is the dominant contribution to the turbulent kinetic energy, produced by the buoyancy flux $\overline{w'\theta_v'}$. For convenience, when we hereafter refer to the cloud velocity we implicitly refer to the vertical velocity, both notations will be used interchangeably. Likewise, when talking about the massflux we refer to the vertical massflux of clouds. Of the quantities specifying the cloud fraction we will focus on the total and liquid water content, q_t and q_l, fractional entrainment and detrainment rates, ϵ and δ, total water flux $\overline{w'q_t'}$, and the relative humidity RH.

The outputs from the LES model are averaged over 10 minutes. Especially fluxes vary notably in 10 minutes and to reduce such fluctuations we have averaged the profiles over one hour; unless stated otherwise the averaging takes place over the third hour. The motivation for this choice is that during the two first hours there is a large spin-up and when running the model for too long the $\overline{\theta_v}$ profiles start diverging.

Sampled results like the cloud fraction and massflux are only meaningful in the cloud domain. In order to better compare these results we have plotted such quantities with a vertical offset; i.e. we have vertically displaced the profiles in such a way that the cloud bases from the different simulations all coincide. At the cloud top the cloud dynamics are less reliable because of few sampled points so when using a vertical offset we only show the first 1000 meters of the cloud layer and the zero-level denotes the cloud base.

Siebesma and Cuijpers (1995) argued that the cloud core decomposition gives the best

turbulent flux approximations. Our analysis will be based on both the cloud and cloud core decompositions but unless the cloud core decomposition results bring different results from the cloud decomposition, only the latter will be shown. Note that when using such sampling we denote cloud mean values by a subscript, for instance is the mean cloud vertical velocity denoted w_c.

4.1 Humidity effect

4.1.1 Initialization

The driving force of cumulus clouds is the buoyancy, which is determined by the temperature, water vapor and liquid water content. We are interested in studying how a drier atmosphere, though with an unchanged mean buoyancy with respect to BOMEX, influences rising thermals. To this end we changed over the entire vertical domain the initial total water content profiles and adjusted the potential temperature accordingly; the virtual potential temperature remains unchanged if a lower (higher) q_t is accompanied by a higher (lower) θ according to

$$ \mathrm{d}\theta = \frac{-\varepsilon\theta\mathrm{d}q_t}{(1 + \varepsilon q_t + \varepsilon\mathrm{d}q_t)} \quad , \tag{4.1} $$

where $\varepsilon = 0.61$, dq_t and $d\theta$ are changes in total water content and potential temperature, respectively. To see how this expression comes about, let $\theta_{v,B}$ and $\theta_{v,H}$ be the virtual potential temperatures of BOMEX and the sensitivity case, respectively. They read

$$ \theta_{v,B} = \theta_B(1 + \varepsilon q_{t,B}) \quad \text{and} \quad \theta_{v,H} = (\theta_B + \mathrm{d}\theta)\left[1 + \varepsilon\left(q_{t,B} + \mathrm{d}q_t\right)\right] $$

Equating these two expressions yields

$$ -\mathrm{d}\theta - \varepsilon q_{t,B}\mathrm{d}\theta - \varepsilon\mathrm{d}q_t\mathrm{d}\theta = \varepsilon\theta_B\mathrm{d}q_t $$

which reduces to (4.1). Note that the initial profiles prescribe unsaturated conditions, i.e. $q_l = 0$, hence $q_v = q_t$. Figure 4.1 shows the initial q_t and θ profiles. In this set of experiments, 7 sensitivity simulations were carried out. However, two of these yielded forced cloud (dq_t=-1.5 and -3g kg^{-1}, respectively) and one resulted in a stratocumulus cloud deck (dq_t=+1.5g kg^{-1}). These three simulations will not be treated in the remainder of this report. The initial change in q_t ranges from -0.4g/kg to 0.7g/kg with an accompanying change in θ ranging from 0.07K to -0.13K. More details are given in table 4.1.
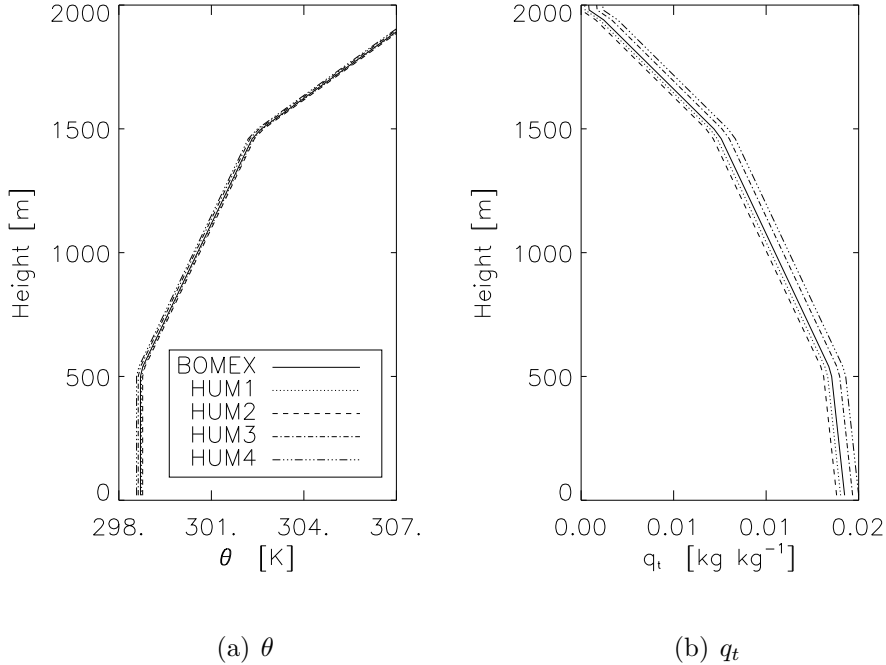
(a) θ (b) q_t

Figure 4.1: Initial profiles of θ, (a), and q_t, (b). Line styles according to legend.

4.1.2   Results from changing humidity

We begin by displaying the cloud fraction σ; figure 4.2 shows that simulations with more humid initialization profiles have cloud forming at lower heights and grow taller. Note also that the maximum cloud fractions of the different simulations differ only slightly. The setup was such that when we made the atmosphere more humid we also lowered the temperature, i.e. we brought the mean atmosphere closer to saturation. Intuitively this should lead to more total and liquid water content. Figures 4.3(a) and 4.3(c) verify our assumption. A change of initial mean total water content prevails after three hours of simulation. The profiles in the cloud layer have crept a bit toward each other, though. This we can explain by looking at the tendency equation for the total water content flux, see figure 4.3(b). In the subcloud layer the $\overline{w'q_t'}$ profiles coincide whereas in the cloud layer they diverge significantly. The driest cases have the steepest vertical gradient of $\overline{w'q_t'}$ in the cloud layer, i.e. the time rate of change of $\overline{q_t}$ is the largest. The larger $\overline{w'q_t'}$ fluxes in the cloud layer are due to q_t differences in the subcloud layer; the moist cases produce moist thermals that bring about large $\overline{w'q_t'}$ fluxes in the cloud layer. The fact that the $\overline{q_t}$ profiles

30

Name	Description	dθ [K]	dq_t [g/kg]
BOMEX		0	0
Hum1	Drier and warmer	0.04	-0.2
Hum2	Drier and warmer	0.07	-0.4
Hum3	More humid and colder	-0.13	0.4
Hum4	More humid and colder	-0.07	0.7

Table 4.1: Description of the simulations included in the set of humidity experiments.

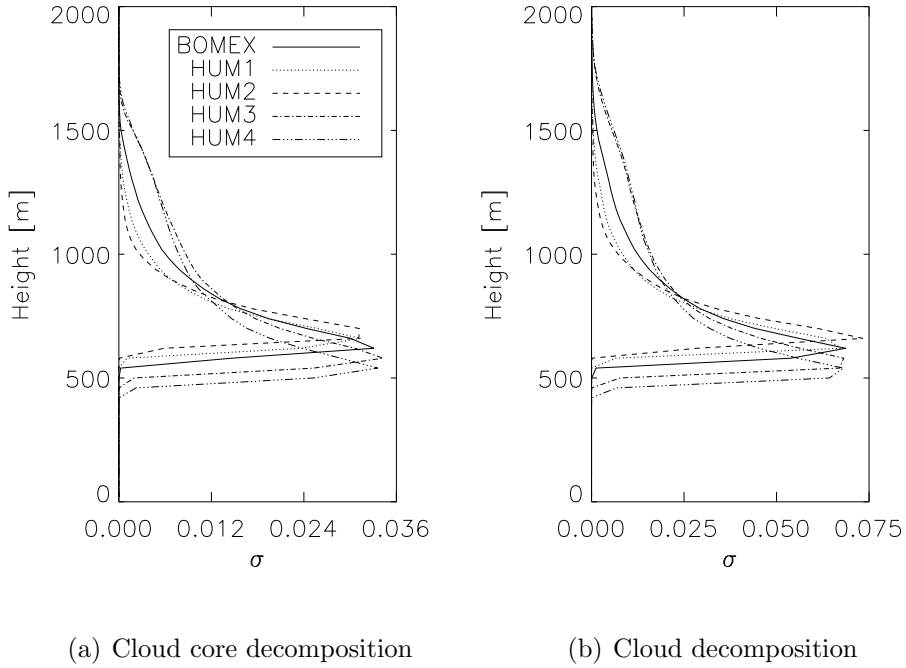(a) Cloud core decomposition   (b) Cloud decomposition

Figure 4.2:   The slab-averaged profiles of the cloud fraction using cloud core decomposition (a), and the cloud decomposition (b). Profiles averaged over the third hour. Line styles according to legends.

converge suggests that the cloud dynamics force the state of the cloud layer toward the BOMEX state. The effect of an initial increase in mean q_t is displayed very well in figure 4.3(c); the slab-averaged profiles of the liquid water content, $\overline{q_l}$, differ significantly. The saturation water content is the explanation; we have increased $\overline{q_t}$ and at the same time

lowered the mean temperature, i.e. the atmosphere is closer to saturation.

Now having covered the cloud properties that follow from intuition we go on to the key element in this research; namely the buoyancy. We stress again that the initial mean buoyancy profiles were the same as for BOMEX and if the mean buoyancy solely dictates all cloud dynamics then the $\overline{\theta_v}$ profiles after three hours of simulation should all coincide. In figure 4.4 the slab-averaged virtual potential temperature, $\overline{\theta_v}$, and the virtual potential temperature flux, $\overline{w'\theta_v'}$, are plotted. The figure shows that the buoyancy profiles have changed after three hours of simulation, hence implying that CAPE does not determine the cloud dynamics alone. During the two first hour of simulation the atmosphere is in a spin-up state and simulating longer will make these profiles diverge more, hence our choice of time averaging. The driest cases have the highest excess mean virtual potential temperature with respect to BOMEX. The driest case has also the steepest vertical $\overline{\theta_v}$ gradient in the lower part of the cloud layer. We have calculated $\frac{\partial \overline{\theta_v}}{\partial z}$ for Hum2, BOMEX and Hum4 for the bottom part of the cloud layer ($\sim$200 meters deep). They are 2.1Kkm^{-1}, 1.6Kkm^{-1} and 1.6Kkm^{-1}, respectively. This shows that, albeit small, the vertical gradients of $\overline{\theta_v}$ differs from simulation to simulation and that the driest case has the less conditional unstable configuration; a rising parcel is said to be conditionally unstable if its virtual potential temperature lapse rate is between the dry and wet adiabatic lapse rate, i.e. if $\Gamma_{\mathrm{dry}} > \Gamma > \Gamma_{\mathrm{wet}}$. Typical values for these lapse rates under adiabatic conditions are 10Kkm$^-$ and 5Kkm^{-1}, respectively. Obviously there is a large difference between those highly idealized rising parcels and the true atmosphere; we elaborate more on this issue in section 5.3. The vertical flux of virtual potential temperature, $\overline{w'\theta_v'}$, is proportional to the buoyancy flux, which powers the development of clouds. In the sub-cloud layer the $\overline{w'\theta_v'}$ fluxes do not coincide; we note that the moist simulations have the steepest gradients in this layer, i.e. during the third hour of simulation more 'cloud fuel' (whereby we picture the buoyancy to be the cloud engine) is pumped into the cloud region. This difference in supply of 'cloud fuel' explains why the $\overline{\theta_v}$ profiles do not coincide; at the cloud base the buoyancy flux has a minimum whereafter it remains negative in a thin layer. In that thin vertical domain a rising cloud parcel is in the CIN domain; the vertical velocity is positive but negatively buoyant with respect to the environment. The more humid simulations have larger maximums in the cloud layer and their $\overline{w'\theta_v'}$ profiles are less dampened. This dampening, i.e. the profiles going to zero with height, is related to the production of turbulent kinetic energy. The $\overline{\theta_v}$ profiles for the most humid simulations are less curved because turbulence has caused the profiles to be smoothened out in the vertical.
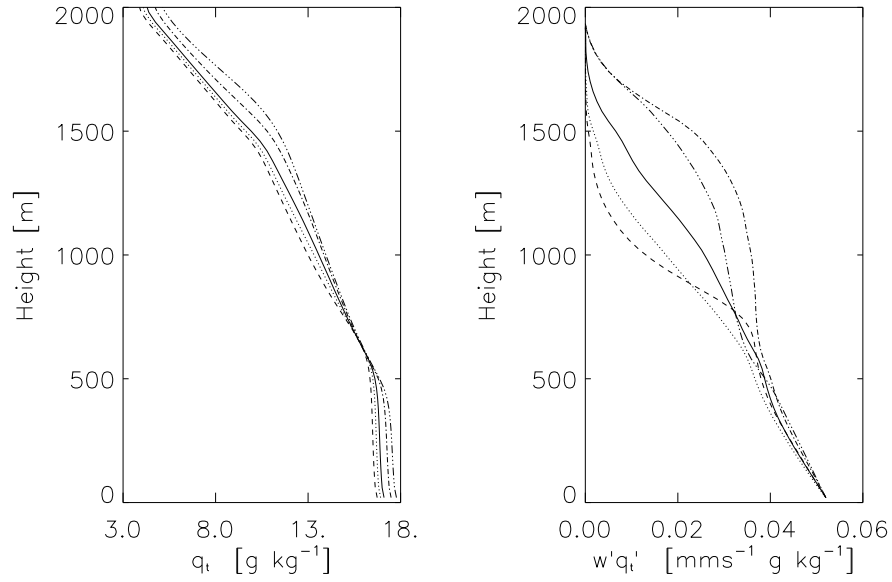
(a) $\overline{q_t}$

(b) $\overline{w'q_t'}$
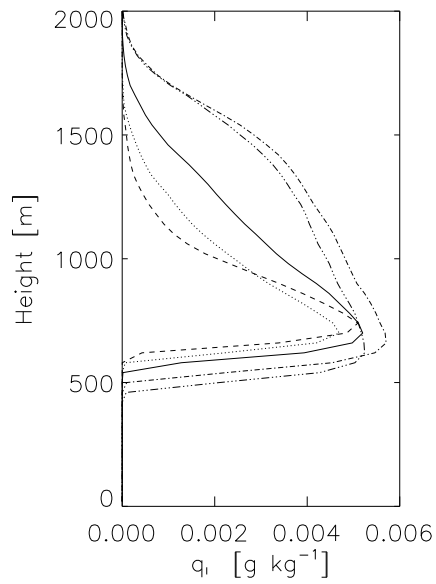
(c) $\overline{q_l}$

Figure 4.3: The slab-averaged profiles of (a) the total water content $\overline{q_t}$, (b) the total water content flux $\overline{w'q_t'}$, and (c) the liquid water content $\overline{q_l}$. Line styles as in 4.2(a).

33

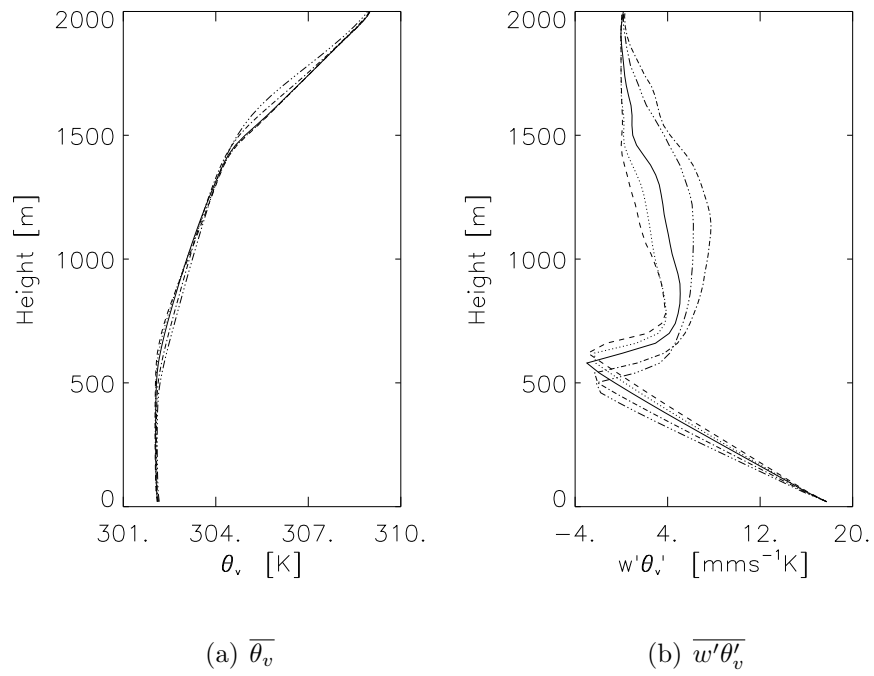(a) $\overline{\theta_v}$ (b) $\overline{w'\theta'_v}$

Figure 4.4: The slab-averaged virtual potential temperature $\overline{\theta_v}$ (a) and virtual potential temperature flux, $\overline{w'\theta'_v}$ (b). Line styles as in figure 4.2(a).

If turbulence is responsible for smoothening out the $\overline{\theta_v}$ profiles then we must expect of the TKE to increase with increased mean atmospheric humidity; figure 4.5 shows that this is indeed the case. The terms $\overline{u'_k u'_k}$ ($k = 1, 2, 3$) are velocity fluctuation variances and their sum is the turbulent kinetic energy. From the large (resolved) scale, energy is passed on to small scale eddies. This is the energy cascade,which works as a brake on the in-cloud vertical velocity and hence also on the massflux. From figures 4.5(a)-4.5(d) we see that the three contributions to the TKE are of the same order. The figure indicates that the velocity variances in all directions are of the same order of magnitude. The most humid simulations generate more TKE, which over a depth of $\sim$1000 meters in the cloud layer stays constant. This constancy is also found in all three $\overline{u'_k u'_k}$ terms.

Turbulence is the physical mechanism behind lateral entrainment and detrainment, ϵ and δ, respectively. The fractional entrainment and detrainment rates of θ_l are calculated by equations (2.11) and (2.12), respectively, and are shown in figure 4.6 with a vertical offset. Both cloud and cloud core decompositions are shown. Instead of using the one hour time averaged values we have computed the entrainment using the ten minute averaged values six times and then averaged. Evidently the smaller the TKE the smaller ϵ becomes. The way θ_l in the cloud is sampled (at each level where there is no cloud θ_l is set to zero) causes numerical problems when calculating $\frac{\partial \psi_c}{\partial z}$ in equation (2.11); the vertical gradients blow up at the cloud base and cloud top. Due to the way of sampling we also get $\frac{\partial \psi_c}{\partial z} < 0$, which implies that the entrainment rate becomes negative. This is not physical and hence only positive entrainment rates are plotted and values around cloud top and base are left out. The results clearly show that the humidity of the atmosphere influences ϵ and δ; the driest simulations have the lowest entrainment rates and hence the largest detrainment rates. To use a more intuitive example, picture at the cloud edge a cloud parcel which has a low liquid water content. When mixing with the environment this small amount of q_l easily evaporates and thus leads to a larger detrainment rate.

We have finally arrived at the mean cloud vertical velocity, which multiplied by the cloud fraction gives the cloud massflux. In figure 4.7 these latter three quantities are shown with a vertical offset. It is remarkable how the vertical velocity profiles coincide in the lower part of the cloud layer. When applying the cloud core decomposition the w_c-profiles coincide even better (not shown). Since the w_c-profiles coincide so well the differences in massfluxes must primarily be ascribed to the differences in cloud fraction, which is also confirmed by the figure. The velocity fluctuations in the top part of the cloud layer is attributed to the low number of cloud points in the sample.

So far we have concluded that the mean buoyancy profiles do not coincide after three hours of simulation and that the massflux is influenced by the mean atmospheric relative

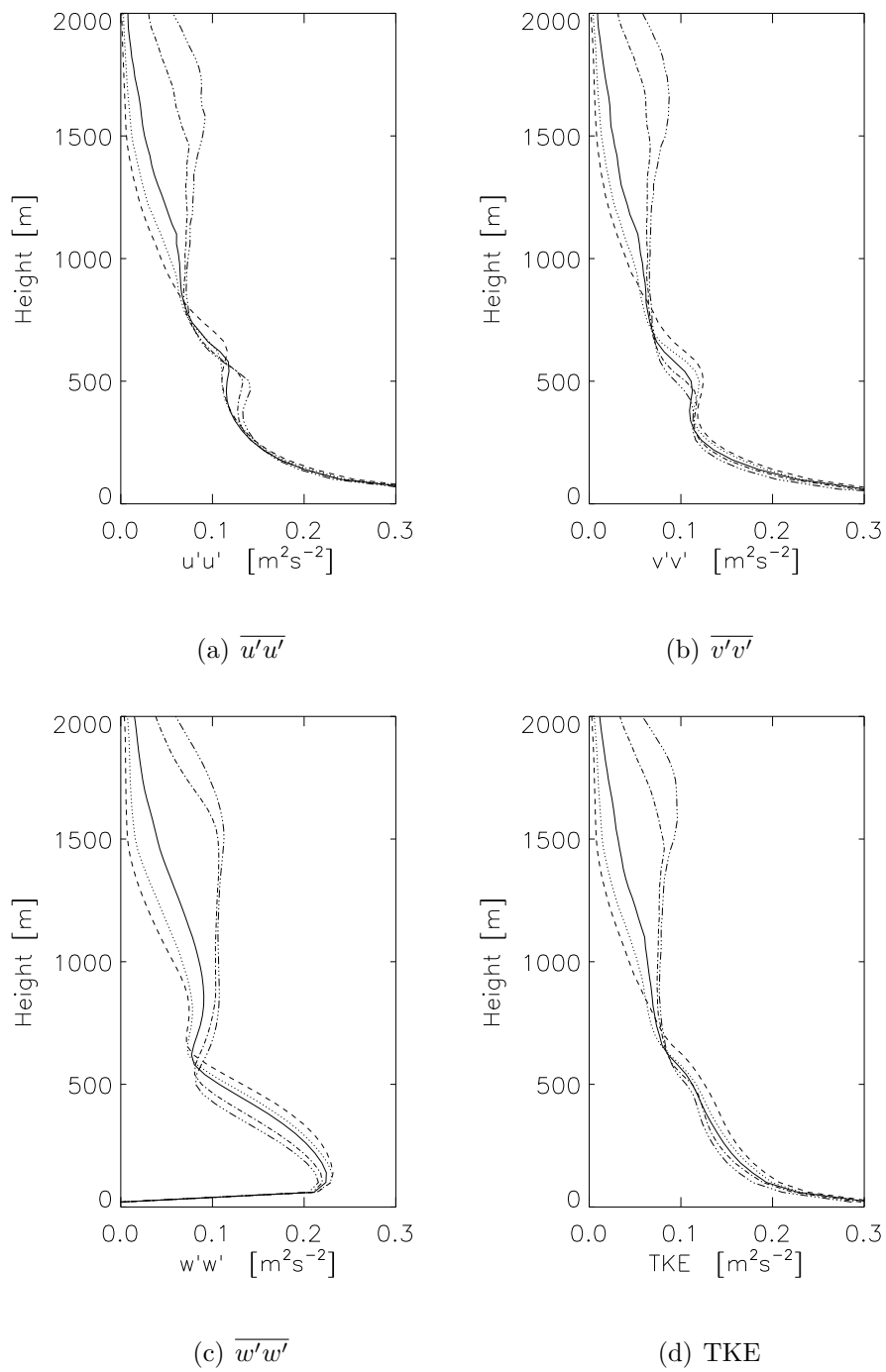(a) $\overline{u'u'}$

(b) $\overline{v'v'}$

(c) $\overline{w'w'}$

(d) TKE

Figure 4.5: The $\overline{u'u'}$ (a), $\overline{v'v'}$ (b) and $\overline{w'w'}$ (c) contributions to the TKE (d). Line styles as in figure 4.2(a).
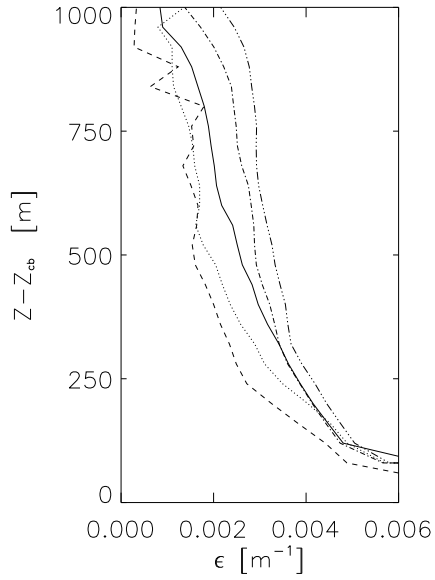
(a) Cloud decomposition
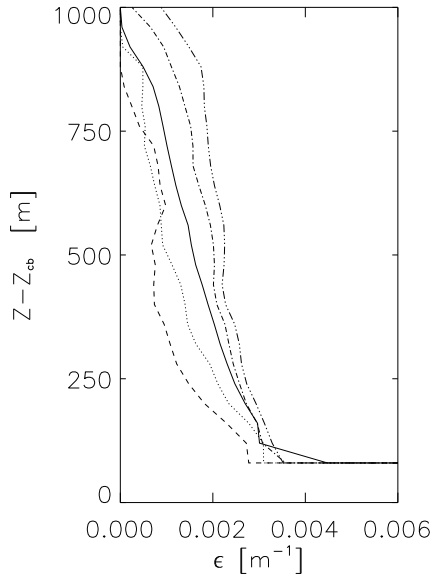
(b) Cloud core decomposition
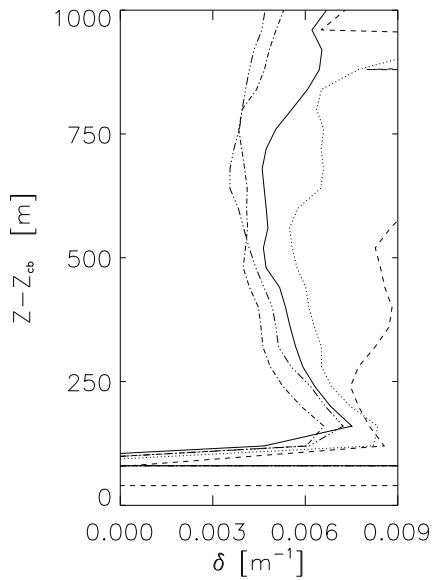
(c) Cloud decomposition
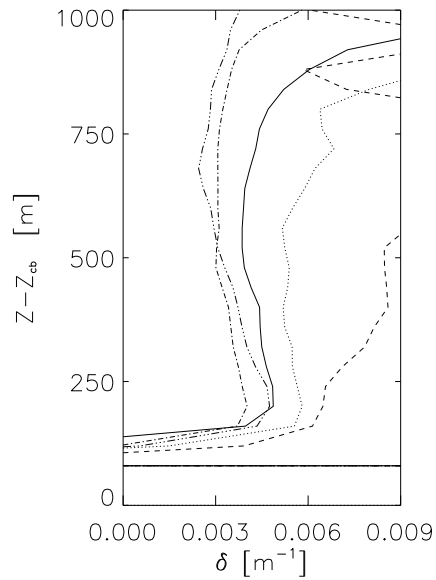
(d) Cloud core decomposition

Figure 4.6: The fractional entrainment rate ϵ using the cloud decomposition (a) and cloud core decomposition (b) together with fractional detrainment rate δ with the same decompositions, (c) and (d) respectively. See text for remarks on time-averaging. Line styles as in figure 4.2(a).

(a) Mean cloud velocity w_c (b) Cloud fraction σ (c) Cloud massflux M_c
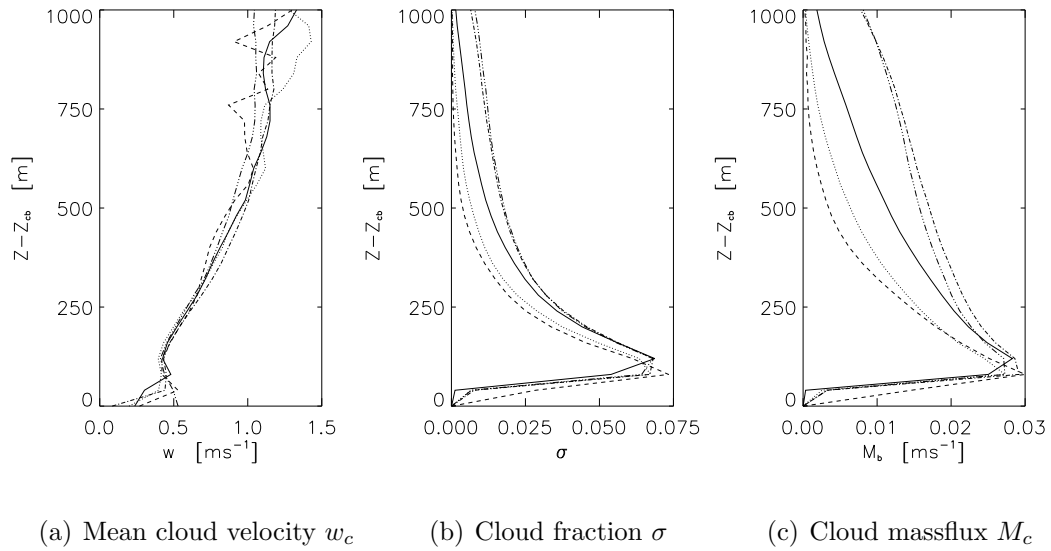
Figure 4.7: The vertical velocity (a), the cloud fraction (b) and the massflux (c). Cloud decomposition with an offset has been used. Legends as in 4.2(a).
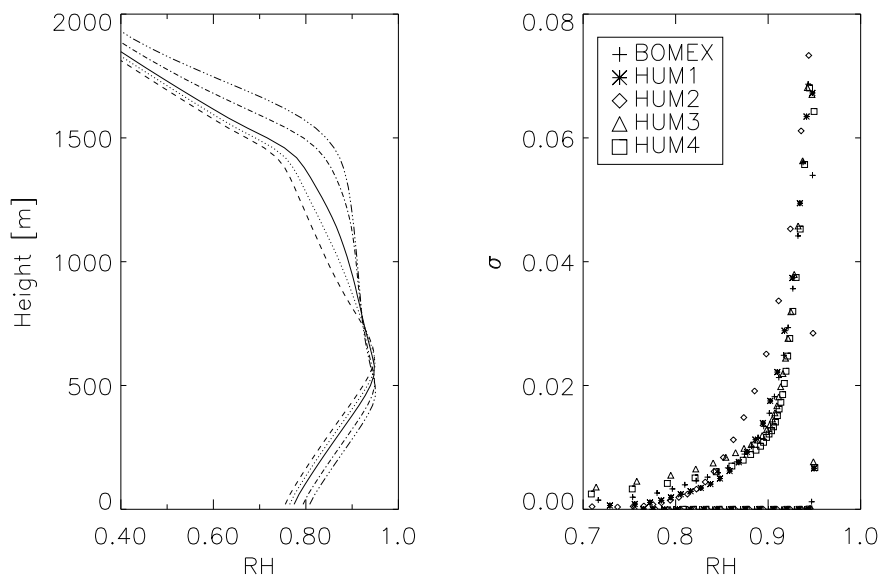
(a) Slab-averaged relative humidity   (b) RH vs σ

Figure 4.8:   The slab-averaged relative humidity (a) and cloud fraction as function of relative humidity (b). In the latter subplot the points with high RH but zero cloud fraction are points just below the cloud base. The three outlyers laying clustered together around $RH = 0.95$ are points exactly at the cloud base. Line styles as in figure 4.2(a) and symbols according to legends.

humidity, RH. The latter property is a measure of cloud forming probability. The slab-averaged relative humidity is plotted figure 4.8(a). When increasing the initial total water content we should intuitively expect of the cloud forming probability to increase. A scatter plot of RH versus σ is shown in figure 4.8(b). The plot shows a sharp increase in cloud fraction when the relative humidity exceeds 90%. In the relative humidity domain shown, the symbols from the different simulations can be connected by a line; a polynomial line should do the job. In that way σ can be parameterized. This may be of interest in GCMs since the vertical velocity profiles coincide to a good degree, the mass flux is a function of σ, which in turn is a function of RH. We note furthermore that at high relative humidities the figure shows points with no cloud fraction. These are the points just below cloud base, i.e. just below the zero-level in subplot (a). The three outlyers clustered around $RH = 0.95$ are points exactly at the cloud base. According to the figure, the most humid simulations have low cloud fractions relative to the RH; those points are however points near the cloud top where the relative humidity is high, yet the cloud fraction is small.

4.2   Surface flux effect

4.2.1   Initialization

In the subcloud layer the convective scaling velocity is given by

$$w_*^3 = 2.5 \frac{g}{\overline{\theta_v}} \int_{\text{Surface}}^{\text{Cloud base}} \overline{w'\theta_v'} dz \quad , \tag{4.2}$$

(see Grant and Lock, 2004), who also uses this quantity when trying to scale the buoyancy flux. In operation models, such as European Center for Medium range Weather Forecasting (ECMWF), use the convective scaling velocity in cloud parameterizations but is it influences by the surface fluxes? The virtual potential temperature flux is controlled by the potential temperature flux and the moisture flux, also called the sensible heat and latent heat flux, respectively:

$$\overline{w'\theta_v'} = (1 + \varepsilon\overline{q_v})\overline{w'\theta'} + \varepsilon\overline{\theta}\,\overline{w'q_t'} \quad .$$

The idea behind this set of simulations is to see how the surface conditions can alter the cloud dynamics; we have changed the surface flux of water vapor $\overline{w'q_t'}_0$ (remember that $q_t = q_v$ under unsaturated conditions) and adjusted the surface flux of potential temperature $\overline{w'\theta'}_0$ in such a way that the virtual potential temperature flux at the surface, $\overline{w'\theta_v'}_0$, is unchanged with respect to the reference case. Subscript 0 denotes surface value. Since $\overline{w'\theta_v'}$ decreases linearly this implies that w_* is kept constant. The relative change in

$\overline{w'q'_{v0}}$ is in the range -60% and 40% (see table 4.2 for more details.) The flux of water vapor will affect the water vapor available for condensation. We hypothesize that an increase in $\overline{w'q'_{t0}}$ will lead to an increase in water vapor, which upon condensation will release heat and make the air parcel ascend.

Name	Description	$\overline{w'q'_{t0}}$ [ms^{-1} (kg·kg^{-1})]	$\overline{w'q'_{t0}}/\overline{w'q'_{t0,B}}$	$\overline{w'\theta'}_0$ [ms^{-1}K]	$\overline{w'\theta'}_0/\overline{w'\theta'}_{0,B}$
SF1	Reduced latent heat flux	2.08 10^{-5}	40%	0.01364	170.5 %
SF2	Reduced latent heat flux	4.16 10^{-5}	80%	0.00988	123.5 %
SF3	Increased latent heat flux	6.24 10^{-5}	120%	0.00614	76.6 %
SF4	Increased latent heat flux	7.27 10^{-5}	140%	0.00426	53.3 %

Table 4.2: Description of the simulations included in the set of modified surface fluxes. The subscripts 0 and B denote surface level and BOMEX, respectively.

4.2.2 Results from modified surface fluxes simulations.

When increasing the surface latent heat flux we expect more condensation and hence and increase in cloud fraction. The results, shown for both the cloud and cloud core decomposition in figure 4.9, confirm our assumption. When increasing the surface latent heat flux, the cloud base is lowered and the maximum cloud fraction is also affected. There is a difference between the two decompositions; figure 4.9(a) shows that the cloud core is significantly affected; the maximum is almost halved.

Not only the cloud fraction is affected by an increased $\overline{w'q'_{t0}}$; a higher total water content is found at all levels, in particular in the subcloud layer, see figure 4.10(a). Note that unlike the previous set of simulations, the initial $\overline{q_t}$ profiles are identical to that of the reference case; the differences seen after three hours of simulation are attributed to the changed surface latent heat flux. The differences of in-cloud q_t are almost constant throughout the cloud layer (not shown). The flux of total water content, $\overline{w'q'_t}$, has a negative vertical gradient, i.e. $\partial \overline{q_t}/\partial t > 0$ throughout the subcloud and cloud layer. The net effect of turbulence is thus to wetten the above laying levels; humidity is transported with thermals to the cloud layer and outside the clouds there is a compensating large-scale subsidence bringing down dry air. Only for SF1 does the gradient change sign; it is practically zero. As expected, an increase in $\overline{w'q'_{t0}}$ results in more water vapor being condensed, see figure 4.10(c). Not only is the initial mean buoyancy for all simulations the same; the initial humidity and

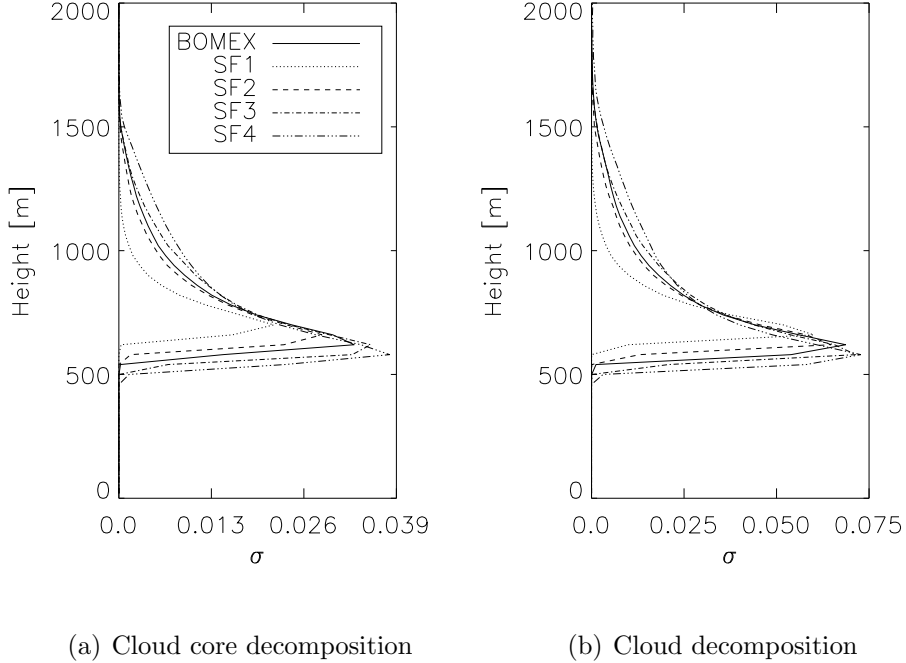(a) Cloud core decomposition (b) Cloud decomposition

Figure 4.9: The slab-averaged profiles of the cloud fraction. Increases in the surface latent heat flux results in lower cloud base and thicker clouds. The maximum cloud fraction, found at cloud base, also increases. Time averaged over the third hour. Line styles according to legend.

temperature profiles are identical as well, so can we expect of the mean buoyancy profiles after three hours of simulation to coincide? The result is shown in figure 4.11(a) together its vertical flux. The profiles from the different simulations coincide very well. An increase in surface latent heat flux yields a larger flux in the cloud layer, i.e. the supply of fuel to the cloud-engine is larger. This is shown in figure 4.11(b). In the lower part of the cloud layer, the tendency of $\overline{\theta_v}$ is negative, i.e. the fuel to the cloud engine is decreasing, see figure 4.11(b). In the top part of the cloud layer the tendency becomes positive. $\overline{w'q'_{t0}}$ clearly influences the buoyancy flux and hence also the TKE, which is shown in figure 4.12, together with its contributors.

The contributors to the TKE are of the same order and in the sense that an increase in $\overline{w'q'_{t0}}$ leads to increased liquid water content, the TKE for the largest $\overline{w'q'_{t0}}$ are as in the humidity set the largest. Unlike the other set, the TKE does in no simulation remain constant throughout a part of the cloud.

(a) $\overline{q_t}$

(b) $\overline{q_l}$
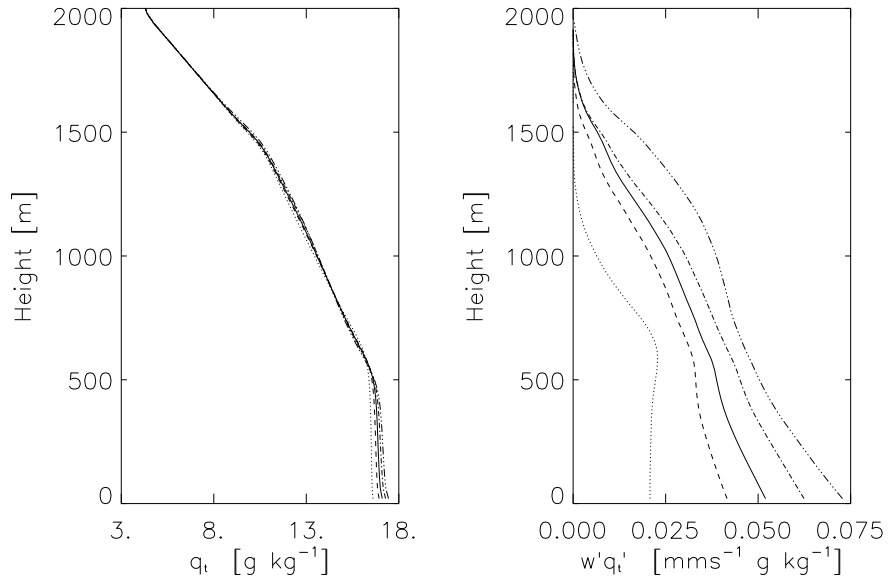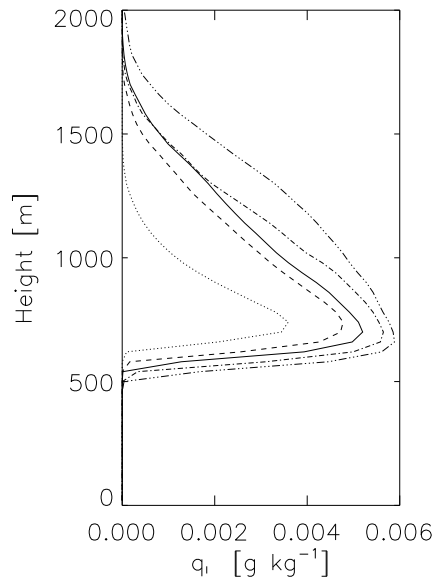
(c) $\overline{w'q'_t}$

Figure 4.10: As figure 4.3. Line styles as in 4.9(a). Line styles as in figure 4.9(a) and symbols according to legends.

(a) $\overline{\theta_v}$ (b) $\overline{w'\theta_v'}$
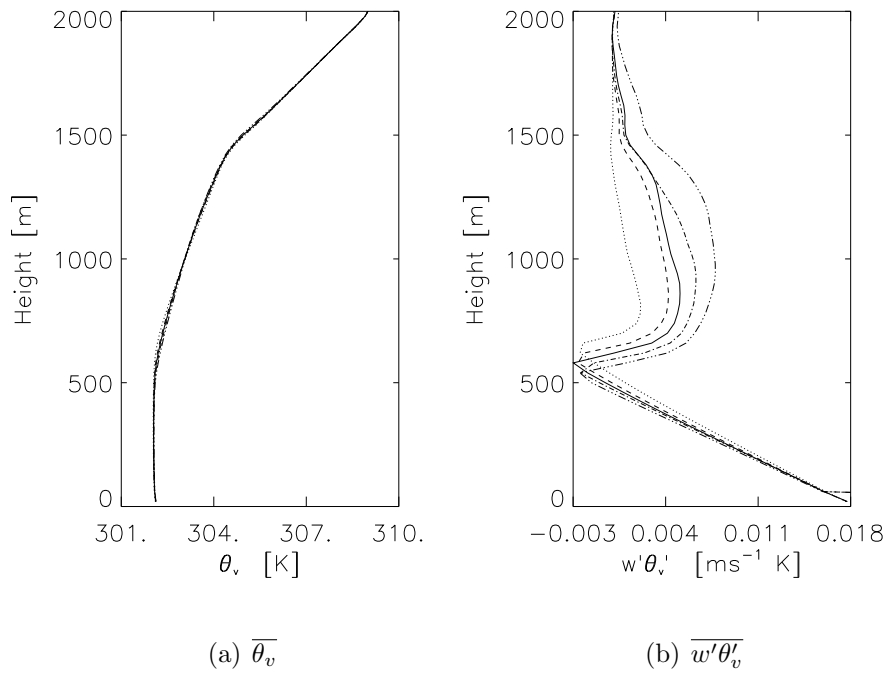
Figure 4.11: (a) The slab-averaged virtual potential temperature profiles for changed surface fluxes. The profiles coincide very well. In the simulations with an increased $\overline{w'q_{t0}'}$ the subcloud layer is warmer than in the other runs. From the middle of the cloud layer and above, the picture is opposite. (b) The turbulent flux of virtual potential temperature $\overline{w'\theta_v}$. Line styles as in figure 4.9(a).

(a) $\overline{u'u'}$

(b) $\overline{v'v'}$

(c) $\overline{w'w'}$

(d) TKE
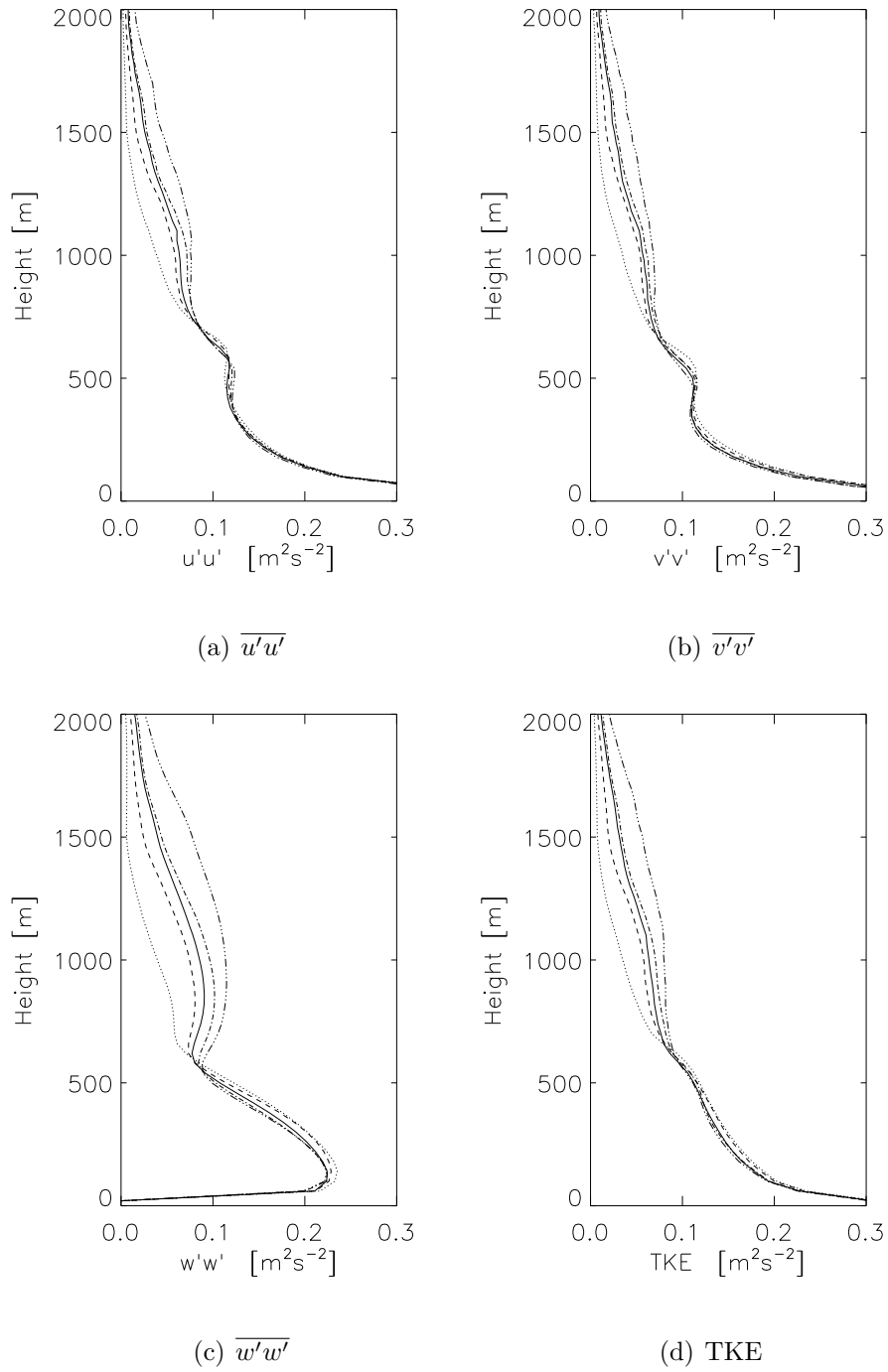
Figure 4.12: Velocity fluctuation variances, (a)-(c) and the TKE (d). Line styles as in figure 4.9(a).
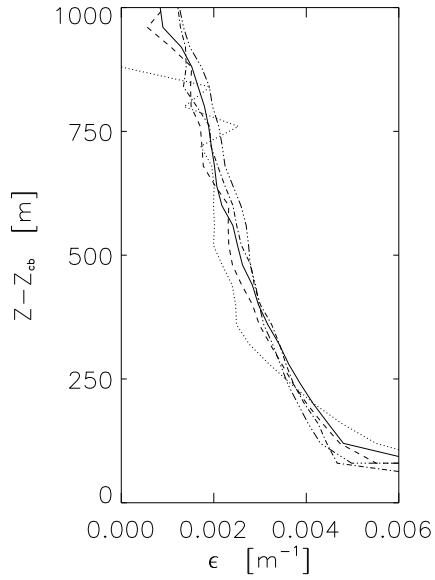
(a) Cloud decomposition
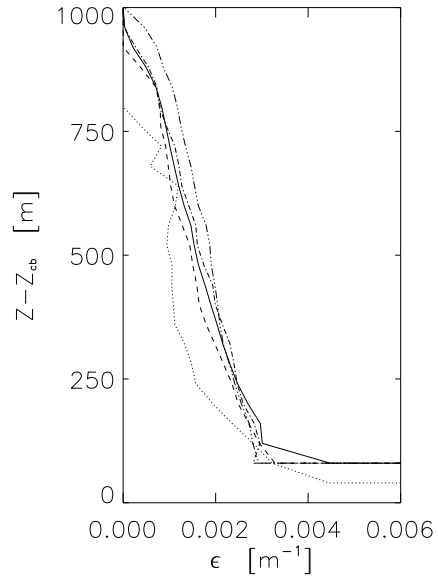
(b) Cloud core decomposition
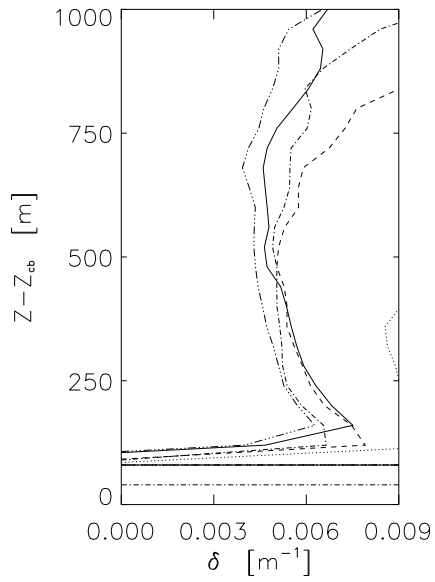
(c) Cloud decomposition
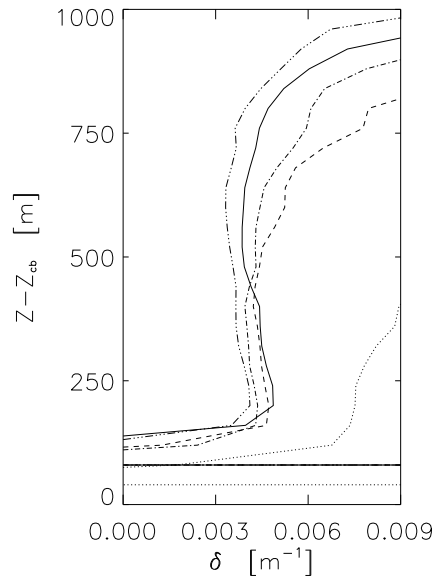
(d) Cloud core decomposition

Figure 4.13: As in figure 4.6. Remarks regarding computation also given in section 4.1.2. All legends as in (a).

(a) In-cloud vertical velocity   (b) Cloud fraction   (c) Cloud mass flux
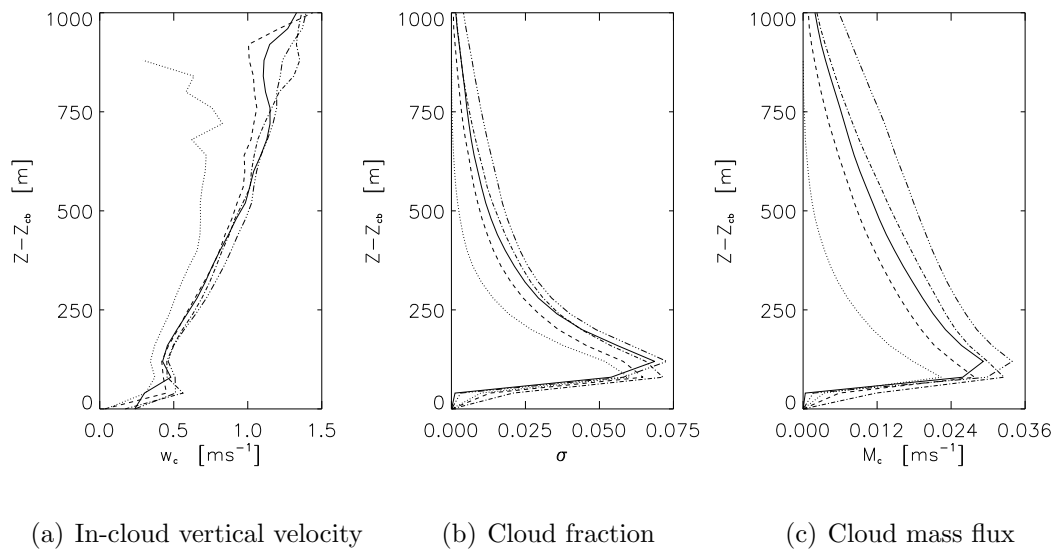
Figure 4.14:   As in figure 4.7. Line styles as in figure 4.9(a).
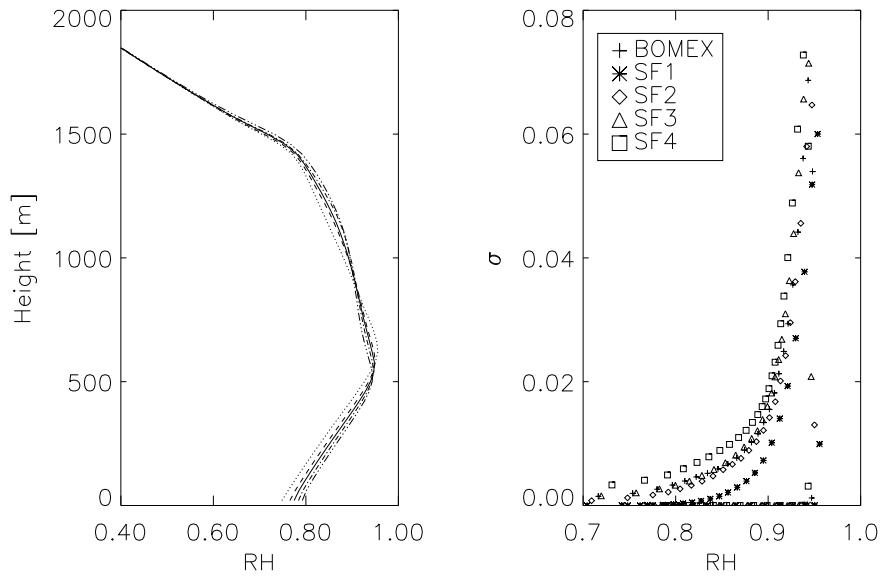
(a) Slab-averaged relative humidity

(b) RH vs σ

Figure 4.15:   As figure 4.8.

Just as in the previous set of simulations, the drier the atmosphere is the lower the TKE becomes, which we expect to see in the fractional entrainment and detrainment rates, shown in figure 4.13. ϵ and δ of θ_l are for both cloud and cloud core decomposition plotted with a vertical offset. The figures show the same results as in the other set of simulations; a lower latent heat flux at the surface leads to a drier atmosphere which yields a smaller ϵ. This reduction is not as large as in the previous set, though; altering the surface fluxes does not strongly affect ϵ. The same simulations produce larger detrainment rates.

This set has with respect to the previous set shown that altering the surface fluxes does not influence the cloud dynamics as much as altering the mean humidity and temperature. The entrainment and detrainment rates together with the buoyancy should affect the cloud massflux and cloud vertical velocities, respectively. We have already presented the cloud fraction, but let us now combine them and look at our main objective, namely the cloud massflux. The vertical offset seems to make all the w_c-profiles coincide and thus the different profiles of M_c must be attributed mainly to the cloud fraction. Figure 4.14 shows the cloud massflux using the cloud decomposition and we see substantial differences between the simulations. We can conclude that knowing w_* is not enough in cloud parameterization, the surfaces fluxes can be altered such that w_* is unchanged and yet the cloud dynamics clearly differ.

Above we have shown that we by changing surface fluxes can affect σ, which we want to relate to the relative humidity, which is shown in figure 4.15. As expected, the relative humidity increases when $\overline{w'q'_{t0}}$ is increased; more humidity is supplied from the surface. Also shown is the scatter plot of RH versus σ. FS1, which has a severely reduced $\overline{w'q'_{t0}}$, has the lowest values of σ vs RH.

Chapter 5

Analysis

5.1 Probability density functions

We are not only interested in slab-averaged quantities. For instance, the higher in the atmosphere the fewer cloud points are counted, which is reflected in the cloud fraction. But what is not reflected are fields, such as the θ_l- and q_t fields, of the individual clouds. One way to investigate these fields is to look at individual points and to see how many points are within one specific temperature interval or q_t interval, i.e. we will use individual gridpoints to make probability density functions, PDFs. The results we present are, unless stated otherwise, based on in-cloud values. This implies that a sampling criteria has been imposed; we have chosen the cloud decomposition. Since we at this stage are only interested in fluctuations we have subtracted the slab mean. An example better explains what we are doing; for an arbitrary quantity ψ, we look at its value in gridpoint (i, j) and subtract the slab-averaged mean, i.e. we evaluate $\psi_{i,j} - \overline{\psi} = \psi'_{i,j}$ (remember that a single prime denotes deviation from the slab mean, see section 3.1.1). The value of the grid point is only used in the PDF if it contains liquid water. The cloud mean will be denoted by a subscript, e.g.

$$\psi'_c = \frac{\sum\limits_{i,j} \left(\psi_{i,j} I_{i,j} - \overline{\psi} \right)}{\sum\limits_{i,j} I_{i,j}} \quad , \tag{5.1}$$

where $I_{i,j} = 1$ if the gridpoint contains liquid water and zero otherwise. Based on these grids we will also calculate cloud variances. A remark on the PDFs: the values of ψ can span a large range and the number of cloudy points is rather scarce hence choosing too small intervals will lead to meaningless PDFs. The PDFs will also be meaningless if the intervals are chosen to be too coarse; to intercompare different PDFs we had to fix the number of

intervals and we had to compromise on the number of intervals to ensure that they were neither to coarse nor to fine, which however sometimes leads to non-Gaussian distributions. Furthermore, the fields are strongly dependent on time so we used the instantaneous fields, which are written for each 15 minutes, to make the PDFs that we finally time-averaged for the third hour.

5.1.1 PDF at different heights

In figure 5.1 the PDF of fluctuations for the following in-cloud quantities are shown; θ_l', θ_v', w' and q_t'. The PDFs are based on data from the BOMEX simulation; the PDF from three different heights are shown.

The cloud mean values and variances will support the graphs and are given in table 5.1.

		800 m	1000 m	1200 m
θ_l'	Mean [K]	-5.75E-01	-8.47E-01	-1.16E+00
	Var [K]^2	2.17E-02	4.30E-02	7.65E-02
θ_v'	Mean [K]	7.13E-02	1.44E-02	-9.95E-02
	Var [K]^2	4.80E-02	6.71E-02	9.31E-02
w'	Mean [(ms^{-1})]	7.40E-01	1.01E+00	9.66E-01
	Var [(ms^{-1})]^2	4.53E-01	7.74E-01	1.20E+00
q_t'	Mean [(kg kg^{-1})]	1.42E-03	1.76E-03	2.21E-03
	Var [(kg kg^{-1})]^2	1.23E-07	1.73E-07	2.36E-07

Table 5.1: The mean and variance of in-cloud θ_l', θ_v', w' and q_t' values. These values correspond to figure 5.1. All data taken from the BOMEX simulation.

For convenience we have only included three heights but calculations at other heights have been made to confirm the trends:
The in-cloud fluctuations of θ_v show both positive and negative values. The PDFs are at higher heights shifted toward lower values and the cloud mean at some point even becomes negative; this happens at a height of about 1200 meters. The fact that the mean decreases supports the theory of buoyancy reversal; at some height the cloud parcels on average become negatively buoyant due to evaporative cooling. Figure 5.1(c) shows that the in-cloud fluctuations of the vertical velocity also attain both positive and negative signs. The variance of both θ_v' and w' confirm that the PDFs broaden with height. As a consequence of
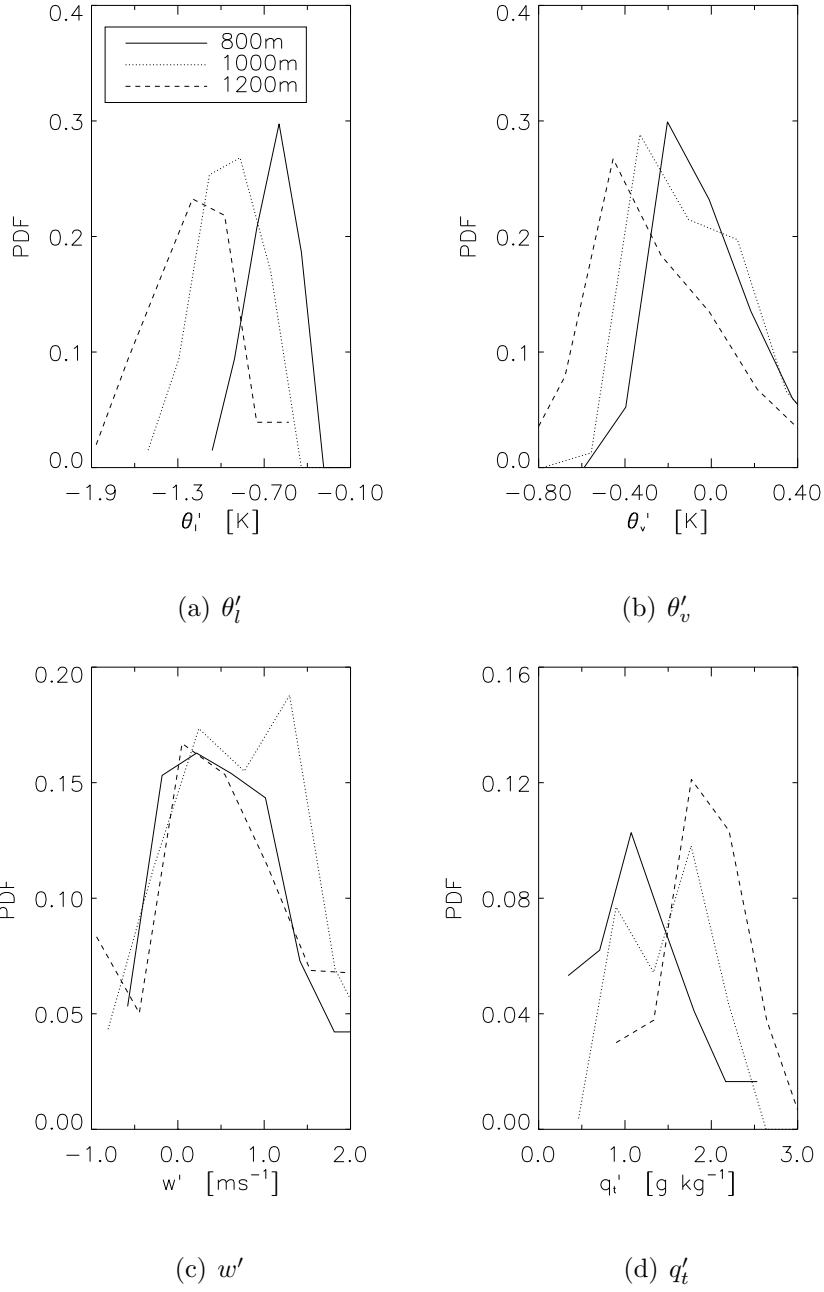
Figure 5.1: Time averaged PDFs of θ_l', θ_v', w' and q_t' using data from BOMEX. The three graphs show PDFs at three different heights; 800, 1000 and 1200 meters, respectively. The values have been connected with a line. A Gaussian form is recognized. Line styles according to legends.

the broadening, a larger fraction of the particles will with increasing height be negatively buoyant and hence obtain negative vertical velocities. The readers familiar with the LES model might want to compare the values of w'_c with those shown in figure 4.7(a). However, in slab-averaged vertical velocity is largely determined by the incloud vertical velocity; $\overline{w} \sim w_{;c}$ but not completely. There is a discrepancy, which we have further explored in this section.

The PDFs of θ'_l and q'_t all have the same sign. The negative sign of the former indicates that the liquid potential temperature is lower than that of the environment. This implies that either the cloud potential temperature is lower than that of the environment, or q_l is greater in the cloud, or both. Certainly, $q_t = 0$ in the environment, but mean values of θ' are all negative (not shown). This shows that clouds are colder than their environments. The PDFs also that they become even colder with height. The variance also increases with height, i.e. the distribution function becomes wider. q'_t, on the other hand, is in the cloud always positive. The fact that the clouds are colder and have higher q_t than the environment is also expected; lower temperatures and more q_t is essential for cloud forming.

Interesting for weather forecasting models is to know the q'_t distribution for the *whole* grid together with saturation water content q_{sat} and temperature; they determine how likely cloud formation is. An illustration is shown in figure 5.2; say we at an arbitrary level have a saturation water content q_{sat}, and a total water content $\overline{q_t}$, with fluctuations q'_t, from which we make a PDF. Assuming the temperature over the horizontal grid is constant, above one critical value, $q_{t,crit} = q_{sat}$, the plume gets saturated and a cloud is formed. Thus the longer the tail of the PDF the larger the chance of cloud forming is. Figure 5.2(a) illustrates how two different PDFs can yield two different chances of cloud forming. Neglecting the temperature effects on q_{sat} should be avoided; compared to their environment clouds have lower temperatures, which in turn brings down q_{sat}. Figure 5.2(b) shows a real PDF of q'_t using the whole grid from BOMEX at 800, 1000 and 1200 meters. The graphs clearly get narrower with height, i.e. the chance of cloud forming decreases.

5.1.2   PDF of different simulations

We can also look at differences in fluctuations between the different simulations; the same quantities as in figure 5.1 are used, and are shown in figure 5.3. For the sake of convenience we only intercompare the following simulations: BOMEX, Hum2, Hum4, SF2 and SF3 at one height; 1000 meters.

The θ'_l fluctuations are related to the humidity of the atmosphere. The graph, supported

(a) Illustration
    (b) Real
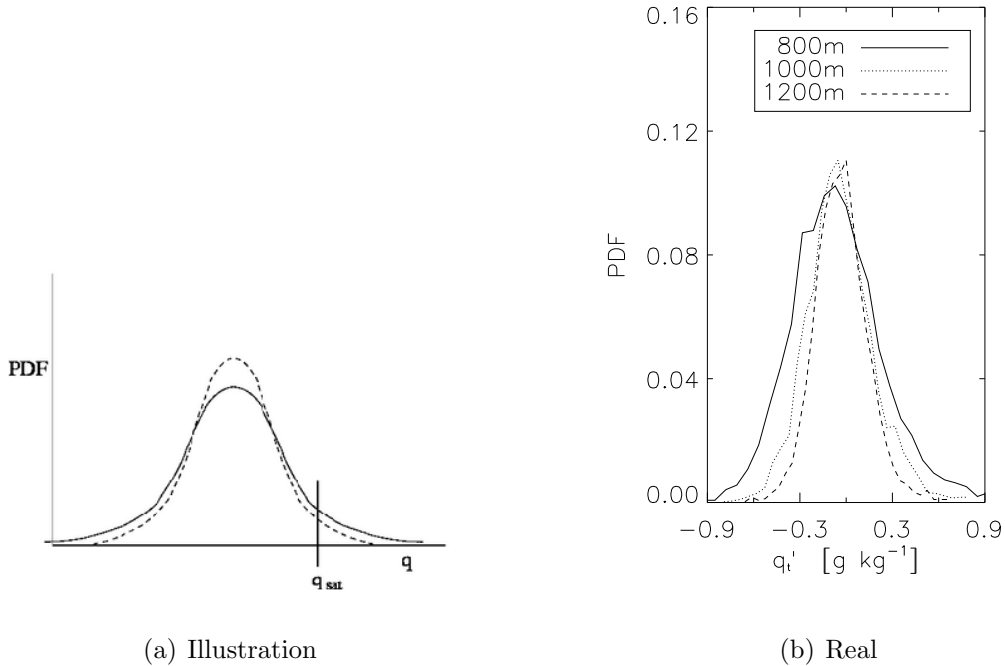
Figure 5.2: (a) Two arbitrary PDFs of slab-averaged q_t. The chance of cloud forming is given by the probability given to the right of the thin solid line, i.e. the full thick line predicts larger chances of cloud forming. In (b) a real example of the slab-averaged q_t, taken from BOMEX, is shown. Line styles according to legends.

by table 5.2, shows that the in-cloud mean $\theta'_{l,c}$ of the driest simulations are the most negative with respect to their environments. As expected, the $\theta'_{l,c}$ values for all simulations are negative. Interestingly we also note that the variance for all simulations are larger than that for BOMEX. Expecting of a dry atmosphere to have only a few energetically rising plumes (having low θ'_l) with many cloud points nearly being environmental points (θ'_l close to that of the environment) would yield a large variance. This is contrary to what we find; Hum2 and SF2, which are the driest simulations, have smaller variances than Hum4 and SF4. The trick is to look at the in-cloud mean together with the variance; when subtracting the standard deviation from $\theta'_{l,c}$ we get lower values for the driest simulations.

The PDF of $\theta'_{v,c}$ makes it a bit hard to distinguish which case has the lowest $\theta'_{v,c}$. With aid of table 5.2 we see that there is no straight forward relationship between atmospheric humidity and $\theta'_{v,c}$. Again we apply the trick of subtracting the standard deviation from the in-cloud mean. For all simulations that operation gives negative values. With respect to the other simulations, the θ'_v field of Hum2 clearly has more negatively buoyant points but we cannot draw any further conclusions.

(a) θ'_l

(b) θ'_v

(c) w'

(d) q'_t

Figure 5.3:   Same as figure 5.1 except for different simulations. Only one height, 1000 meters, is shown. Line styles according to legends. Mean values and variances are given in table 5.2.

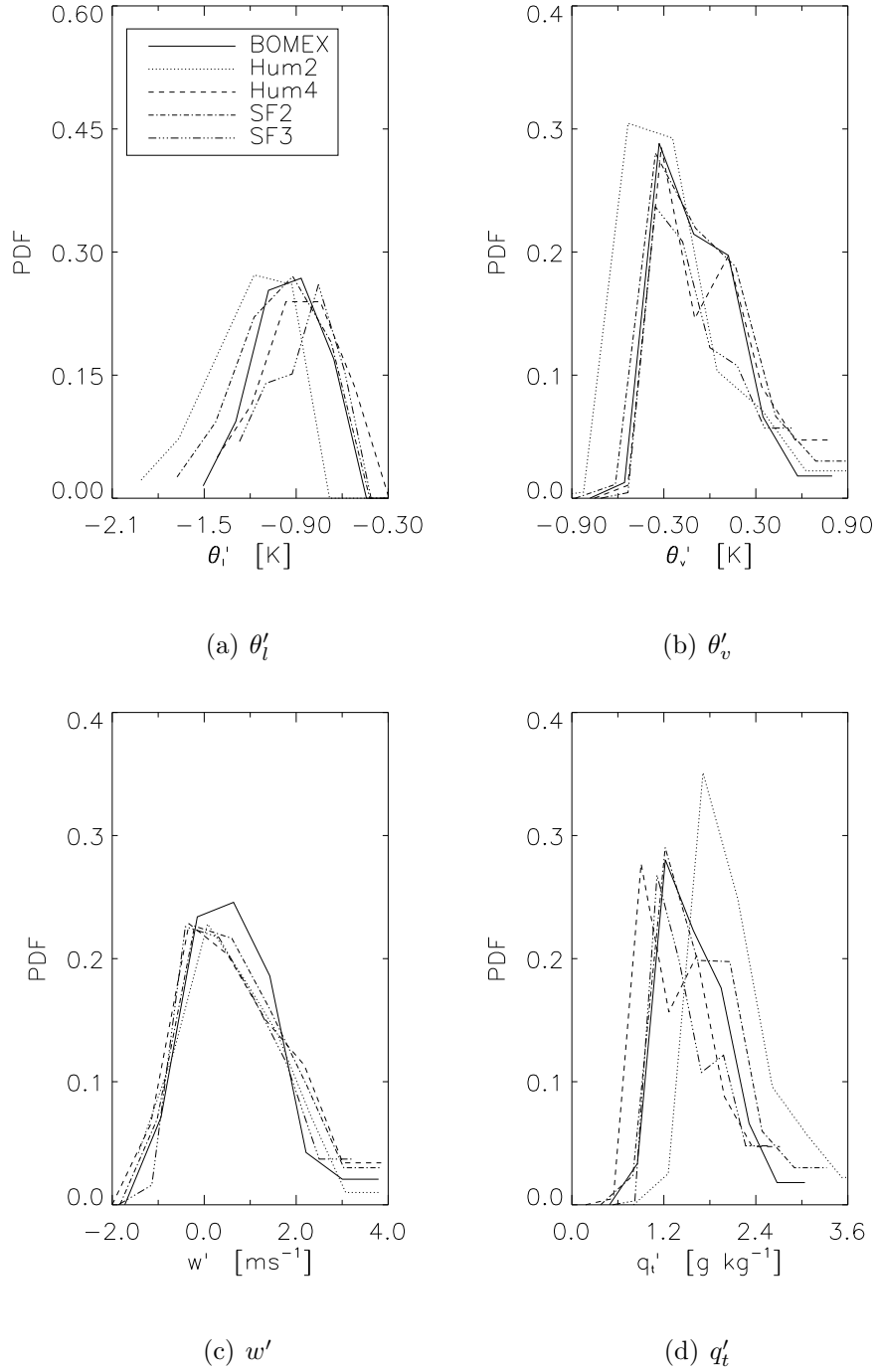The PDFs of in-cloud vertical velocity fluctuations w', do not reveal much, neither does table 5.2. The in-cloud fluctuations of total water content are, as expected, well related to the initial profiles. Both Hum4 (more humid) and SF3 (larger $\overline{w'q'_{t0}}$) have smaller $q'_{t,c}$ and vice versa for Hum2 and SF2. If the mean initial q_t values are increased, a larger $q'_{t,c}$ would intuitively be expected. However, one should not forget that the slab mean has been subtracted, i.e. the denominator in equation 5.1 is smaller.

We conclude this section by raising a question concerning the distribution function in general. For θ'_v and w' we have found that the variances are of the same order as the mean value itself. The PDF look Gaussian but with a variance of the same order a flat PDF is expected. The two other variables, θ_l and q_t, are conserved variables and do not produce variances on the same order as their mean values. The question is thus; can we prescribe a Gaussian PDF for non-conserved variables?

		BOMEX	HUM2	HUM4	SF2	SF3
θ'_l	Mean [K]	-8.47E-01	-1.10E+00	-7.91E-01	-9.00E-01	-7.91E-01
	Var $[\text{K}]^2$	4.30E-02	5.56E-02	6.49E-02	6.33E-02	4.67E-02
θ'_v	Mean [K]	1.44E-02	-9.88E-02	7.17E-02	5.89E-02	9.63E-03
	Var $[\text{K}]^2$	6.71E-02	9.67E-02	8.83E-02	9.57E-02	7.95E-02
w'_c	Mean $[(\text{ms}^{-1})]$	1.01E+00	9.76E-01	1.06E+00	1.05E+00	9.17E-01
	Var $[(\text{ms}^{-1})]^2$	7.74E-01	9.00E-01	1.04E+00	1.02E+00	8.92E-01
q'_t	Mean $[(\text{kg kg}^{-1})]$	1.76E-03	2.31E-03	1.59E-03	1.87E-03	1.70E-03
	Var $[(\text{kg kg}^{-1})]^2$	1.71E-07	2.32E-07	2.53E-07	2.50E-07	2.22E-07

Table 5.2: Same as table 5.1 but for different simulations. All values at 1000 meters.

5.2 Virtual potential temperature

We have initialized $\overline{\theta_v}$ the same in all our simulations and we will now look at the virtual potential temperature after two hours of simulation time using the same simulations as in the previous section, i.e. BOMEX, Hum2, Hum4, SF2 and SF3. In figure 4.4(a) and 4.11(a) their $\overline{\theta_v}$ profiles are shown; it can be seen that the simulations from the humidity set diverge more. For the four simulations mentioned above we have calculated the virtual potential temperature for an adiabatically rising parcel, $\theta_{v,ad}$. To this end we used the ten

56

minutes averaged values of θ_l, Q_t and pressure to computed the adiabatic virtual potential temperature, which we in turn averaged over the third hour. The results are shown in figure 5.4. These profiles should be seen in contrast with the slab-averaged profile; as an example the $\overline{\theta_v}$ profile from BOMEX has been plotted as well. The figures indicates that
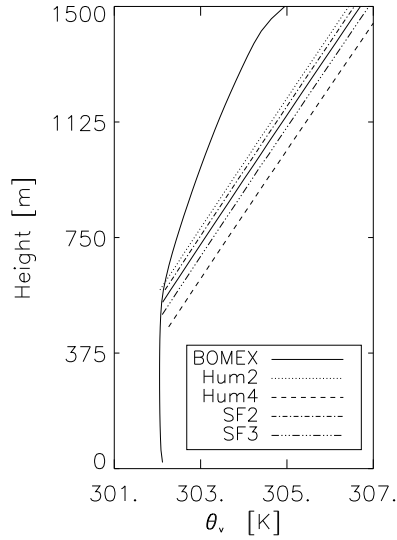
Figure 5.4: The virtual potential temperature for an adiabatically rising parcel. To bring these profiles into context the slab-averaged virtual potential temperature for BOMEX is plotted as well. All profiles averaged over the third hour, see text for more information. Line styles according to legends.

the differences in vertical gradients of $\theta_{v,ad}$ are vanishingly small. However, the figure also suggests that CAPE is very sensitive to the cloud base, see also below. But for now we will turn our attention the effect lateral mixing has on the virtual potential temperature of a rising parcel.

Buoyancy reversal will become more and more prominent with height. In figure 5.5(a) the respective $\theta_{v,c}$ values are subtracted from the slab-averaged virtual potential temperature. Buoyancy reversal, i.e. $\overline{\theta_v} > \theta_{v,c}$, increases with height. Lastly, to get a better idea on how prominent the downdraft region of a cloud is, we have plotted the ratio of downdraft to total cloud points, 5.5(b). The lines coincide very well and we note with interest that the fraction $\sigma_{\text{down}}/\sigma_{\text{cloud}}$ stays approximately constant throughout the whole cloud layer. We will not elaborate further on this point but have included it since it may be of interest in cloud parameterization.
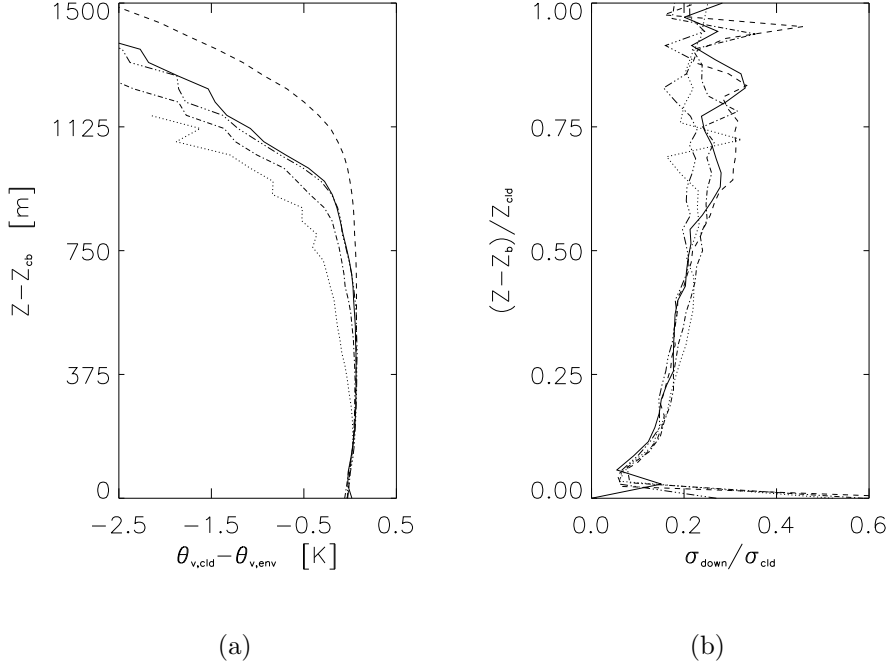
Figure 5.5: The cloud mean virtual potential temperature minus the slab-averaged value, $\theta_{v,c} - \overline{\theta_v}$, plotted with a vertical offset, (a). Also shown is the ratio of downdrafts to cloud points scaled with cloud depth, (b). Line styles as in 5.4.

We now combine CAPE and buoyancy reversal and have a critical view on the buoyancy flux: according to Grant and Lock (2004) the buoyancy flux can be scaled with a factor

$$\sqrt{\frac{M_b}{w^*}} \frac{M_b A}{z_{cld}} \quad , \quad w^* = (M_b A)^{1/3} \quad , \tag{5.2}$$

where M_b is the massflux at the cloud base, w^* is the velocity scale for turbulent fluctuations (Grant and Lock, 2004), and z_{cld} the cloud depth. In our simulations the cloud depth, z_{cld}, was approximately constant and by choosing the initial $\overline{\theta_v}$ to be the same we have aimed at keeping CAPE, A, the same too. This implies that the proposed scaling is determined by the cloud massflux at the cloud base, M_b. The relevance of the buoyancy flux is that it is proportional to the virtual potential temperature flux, which is important in determining how tall clouds grow. In the cloud layer this flux is also the main production term of TKE, which is important for turbulent transport. This makes scaling the buoyancy flux so desirable.

In figure 5.6 we show the unscaled and scaled buoyancy flux. Note that we so far have referred to $\overline{w'\theta'_v}$ as the buoyancy. Strictly speaking this is the virtual potential temperature flux, which is the buoyancy flux times g/θ_0; the buoyancy flux being denoted $\overline{w'b'}$. The scaling profiles are time averaged buoyancy flux profiles divided by time averaged scaling factors; first we calculate the scaling factors using the ten minutes averaged values and subsequently time average them for the third hour. On inspection of figures 5.6(a) and
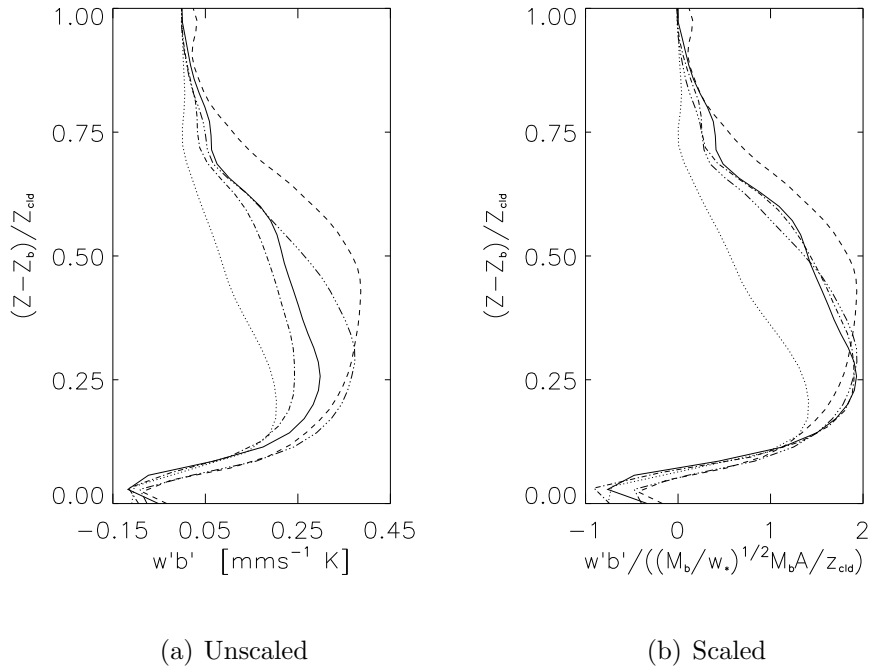
(a) Unscaled   (b) Scaled

Figure 5.6: The buoyancy flux unscaled (a) and scaled (b) according to Grant and Lock (2004). Line styles as in figure 5.4.

5.6(b) we see that the unscaled buoyancy flux profiles do not diverge more than when the scaling has been applied. Figure 5.6(a) shows that the buoyancy flux can differ as much as by a factor of 2 between Hum2 and Hum4 whereas figure 4.7(c) shows that at the cloud base the mass flux for these two experiments is approximately the same. Furthermore, the profiles do not even have the same form, which indicates that it is not possible make the profiles coincide simply by multiply them with some constant. With our results the scaling proposed by Grant and Lock (2004) does not work and the responsible factors are the cloud fraction and difference in virtual potential temperature between environment

and cloud parcel.

In figure 5.6(b) the scaled buoyancy flux profiles for BOMEX, SF2 and SF3 lie closer than the unscaled profiles. We believe that the explanation lies in the cloud fraction; in section 4.2.2 we saw that the cloud fraction of these three profiles are very much similar. But that is not the case for the two humidity simulations, e.g. figure 4.2(b). Thus the cloud fraction is an important, yet not the sole factor in the buoyancy flux. Assume that the tophat approach, $\overline{w'\theta'_v} = M_c(\theta_{v,c} - \overline{\theta_v})$, works. This formula shows that the difference between cloudy and environmental virtual potential is also important.

5.3   Remarks on CAPE

The in-cloud vertical velocity is directly related to the massflux. We therefore desire to scale the in-cloud vertical velocity. CAPE is a good candidate, but does it provide a good scaling and should we really try to estimate the maximum in-cloud vertical velocity by looking at an adiabatically rising parcel? Let us start with the last part of that question; in equation (2.4) the integrant $\theta_{v,c} - \overline{\theta_v}$, together with the vertical distance to be integrated over, LOC-LCL, determines the CAPE. If the parcel is rising adiabatically the CAPE is given by the striped area of figure 2.3. We will call this the adiabatic CAPE. If we on the other hand use the actual $\theta_{v,c}$ as obtained through sampling, CAPE will differ. We have also computed this CAPE in the domain where the cloud is positively buoyant with respect to the environment; hereafter called the 'true CAPE'. In figure 5.7 the θ_v profile of an adiabatically ricing parcel, $\theta_{v,ad}$, is plotted together with $\overline{\theta_v}$, $\theta_{v,\text{core}}$ and $\theta_{v,\text{cloud}}$. The latter two are the cloud-averaged virtual potential temperature under the cloud core and cloud decomposition, respectively. Data from experiments Hum2 and Hum4 have been plotted and only from the cloud base to a height of 1500 meters. The area between the profiles of $\theta_{v,ad}$ and $\overline{\theta_v}$ represents the same as the striped area in figure 2.3 and clearly differs substantially from the area between the $\theta_{v,\text{core}}$ profile and the environment. In figure 5.7(a), $\theta_{v,\text{cloud}}$ exceeds $\overline{\theta_v}$ only in a small fraction of the cloud and produces a CAPE much less than that of the adiabatically rising parcel.

Another critical remark about the adiabatically computed CAPE is that under discretization the location of the cloud base can to some degree alter the CAPE. For instance, assume the $\theta_{v,ad}$ profile is pitched down one level Δz and the gradient is unchanged. This will happen if even only a single thermal gets saturated at a lower height. Figure 5.4 already indicated what would happen if the cloud base was lowered and figure 5.8 schematically highlights the problem: the extra CAPE is approximately proportional to the area of a

(a) Hum2   (b) Hum4
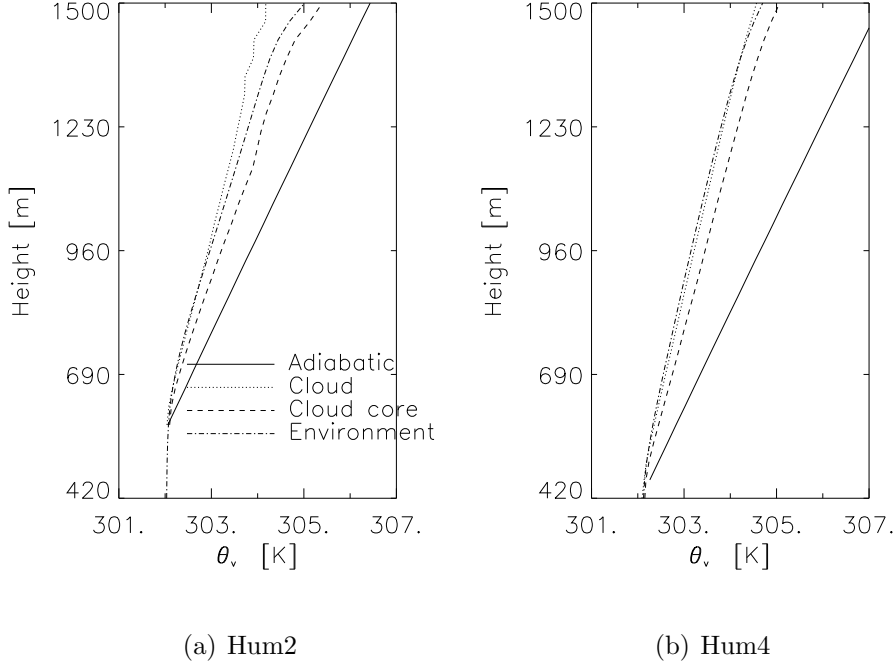
Figure 5.7: The virtual potential temperature of an adiabatically rising parcel, cloud decomposition, cloud core decomposition and the environment, time-averaged over the third hour. Profiles are from experiments Hum2 (a) and Hum4 (b) (for more details see table 4.1) and only from around the cloud base to the inversion. Line styles according to legends.

parallelogram, which is $\sim \Delta z[\theta_v(LOC) - \theta_v(LCL)]$, i.e. the difference in CAPE will approximately be $\Delta z(\theta_v(LOC) - \theta_v(LCL)g/\theta_0$, which is of the order of 10-20m^{2}s^{-2}. Without lowering the cloud base, estimates for CAPE are of the order 30-40m^{2}s^{-2}. In table 5.3 more estimates on CAPE of an adiabatically rising parcel is given together with the true CAPE using the cloud core and cloud decompositions. With these numbers for adiabatic CAPE we see that lowering the cloud base strongly influences the outcome. The figures for the true CAPE using the cloud decomposition are low, which is related to the fact that the cloud as a whole is only over a small depth positively buoyant with respect to the environment. Instead the CAPE as obtained by the cloud core decomposition should intuitively be used; the core dictates how tall a cloud can grow. The table also indicates how reliable the adiabatic CAPE is as indicator for the vertical velocity; both the vertical velocity as computed by equation (2.5) and the maximum velocity up from the LES model
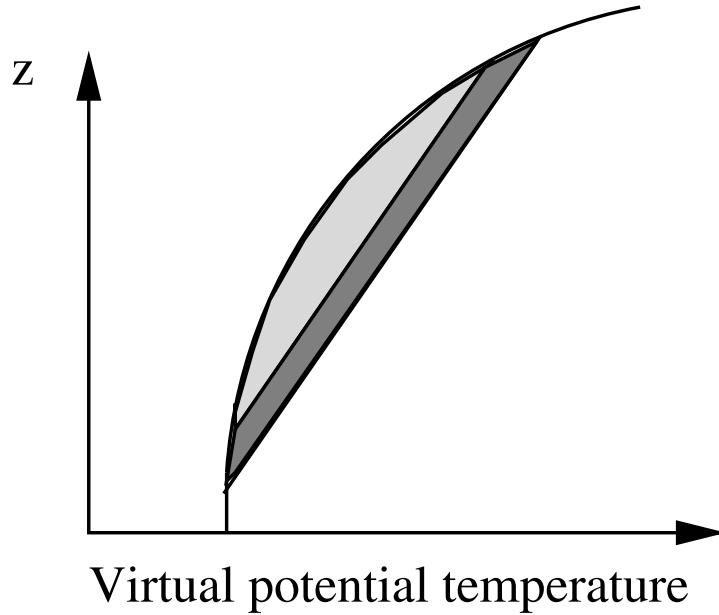
Figure 5.8: The light shaded area is the adiabatic CAPE. Lowering the cloud base yields extra CAPE, here shown as a dark shaded parallelogram.

	BOMEX	Hum1	Hum2	Hum3	Hum4	SF1	SF2	SF3	SF4
Core $[\mathrm{m^2s^{-2}}]$	11.0	9.6	9.9	12.8	13.1	4.9	9.2	10.5	14.1
Cloud $[\mathrm{m^2s^{-2}}]$	0.9	0.4	0.1	2.0	1.4	0.01	0.6	1.1	1.6
Adiabatic $[\mathrm{m^2s^{-2}}]$	27.4	23.4	20.8	36.5	44.7	18.5	23.9	32.1	34.9
$\max w_{\mathrm{core}}\ [\mathrm{ms^{-1}}]$	3.5	3.1	3.1	3.1	2.7	2.2	3.1	3.3	3.3
$\mathrm{w_{CAPE,ad}}\ [\mathrm{ms^{-1}}]$	7.4	6.8	6.5	8.5	9.5	8.0	8.4	6.9	6.1
$\mathrm{w_{CAPE,core}}\ [\mathrm{ms^{-1}}]$	4.7	4.4	4.4	5.1	5.1	6.1	6.9	8.0	8.4

Table 5.3: CAPE as computed by (2.4) using $\theta_{v,c} = \theta_{v,\mathrm{core}}$ or $\theta_{v,c} = \theta_{v,\mathrm{cloud}}$ and CAPE for an adiabatically rising parcel. All CAPE values have been calculated using instantaneous values and at the end averaged. The true CAPE, both decompositions, for experiment Hum4, which rises higher than Hum3, is too low; the error is attributed to the averaging process. Also shown are the numbers for the maximum velocity using equation (2.5) for the adiabatic and true (core) CAPE and from the LES output.

are given. These maximums are from the cloud base to the inversion; the same range over which the adiabatic CAPE is computed. When using the adiabatic CAPE the vertical velocity is overestimated drastically. When instead using the true CAPE under the core

decomposition the estimate for the maximum cloud vertical velocity becomes better, yet not satisfactory.

To assess how well the vertical velocity scales with CAPE, we have scaled the cloud and cloud core vertical velocity with the adiabatic CAPE. The core velocity is also scaled with the true CAPE. The results are shown with an offset in figure 5.9. We have not tried to scale the cloud velocity with the true CAPE since only a fraction of the cloud is positively buoyant. The figure shows that the vertical offset efficiently enough make the w_c profiles coincide; scaling seems to be redundant.

(a) w_{core}

(b) $w_{\mathrm{core}}/\sqrt{2CAPE_{\mathrm{ad}}}$
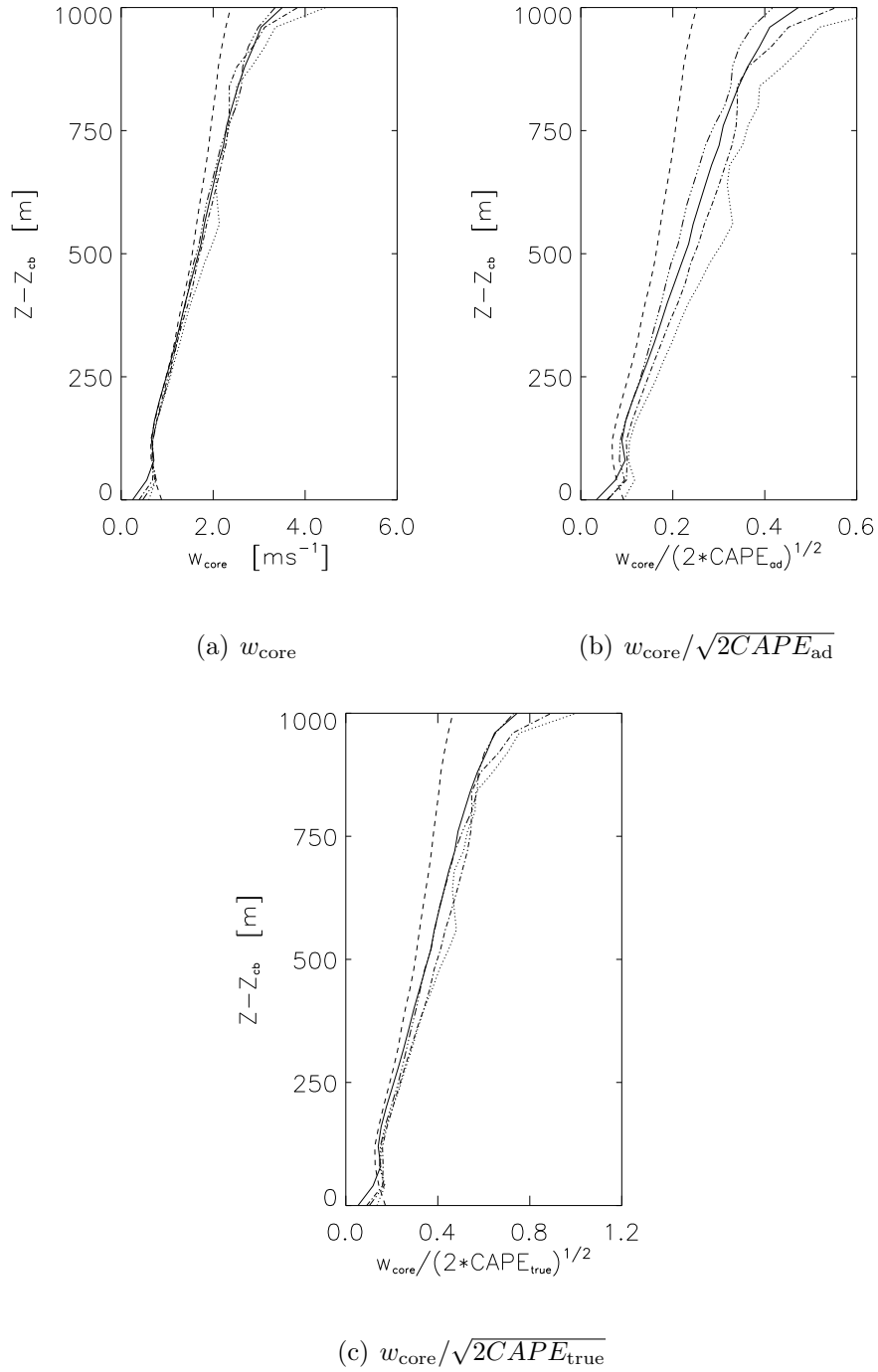
(c) $w_{\mathrm{core}}/\sqrt{2CAPE_{\mathrm{true}}}$

Figure 5.9: The cloud core vertical velocity unscaled (a), scaled with adiabatic CAPE (b) and scaled with true CAPE (c). All plots are with an vertical offset. Line styles as in figure 5.4.

Chapter 6

Conclusions and recommendations

6.1 Conclusions

Shallow cumulus clouds are important in the energy supply to the Hadley circulation and must therefore be included in climate models. They are furthermore too small to directly put into weather prediction models, parameterization is needed.

Derbyshire *et al.* (2004) have looked at the effect atmospheric humidity has on deep convection. Our question is to what degree atmospheric relative humidity influences the buoyancy of a parcel, the lateral entrainment and detrainment rates, and the cloud massflux while keeping the initial buoyancy profiles identical. In general circulation models properties of cumulus clouds are calculated by using the massflux approach. The massflux is determined by the in-cloud vertical velocity and the cloud fraction, the latter being a function of the atmospheric relative humidity. When trying out some hypothesis we noticed that special attention had to be paid to CAPE as well.

In our research we have carried out some sensitivity simulations with the BOMEX as a reference case; we initiated our simulations such that the initial mean buoyancy profiles were the same as for BOMEX. The latter has been widely studied, e.g. Siebesma and Cuijpers (1995). The sensitivity simulations are split into two sets: In the first set the initial mean total water content profiles were altered together with the temperature profiles in such a way that the virtual potential temperature remained unchanged. In the second set we altered the surface latent heat and sensible heat flux in such a way that the virtual potential temperature flux at the surface remained unchanged.

The results show that the buoyancy does not solely determine the cloud dynamics; the virtual potential temperatures between different simulations remained small, yet the dynamics differed significantly. When the initial profiles were made drier, the $\theta_{v,c} - \overline{\theta_v}$ excess

of a cloud soon became negative; cloudy parcels became negatively buoyant with respect to the environment. The same was found when the total water content supply from the surface, $\overline{w'q'_{t0}}$, was reduced. The explanation is as follows; say that a cloudy parcel mixes with a very dry atmosphere. The mixture will then easier become unsaturated, i.e. the liquid water evaporates whereby energy is consumed and the cloud parcel becomes colder. In standard literature (e.g. Holton, 1992) the convective available potential energy is used to estimate the vertical velocity. Buoyancy does not solely determine the vertical velocity, however; turbulence will reduce the transformation from potential energy to cloud upward velocity. The turbulent kinetic energy is affected by atmospheric humidity in the way that the TKE is reduced when the atmosphere is made drier. Turbulence is also responsible for lateral mixing, which consequently is affected by the atmospheric humidity as well; the drier the atmosphere gets the smaller the fractional entrainment rate becomes. Lateral mixing explains why calculating CAPE using an adiabatically rising parcel should be avoided. We have found that not only does the adiabatic CAPE grossly overestimate the cloud vertical velocity, small changes in atmospheric total water content and temperature profiles can change the height of the cloud base and in that way change the adiabatic CAPE by $\sim 25\%$. The cloud massflux is determined by the cloud vertical velocity and the cloud fraction, the latter being the most important factor. Readily we would expect of the cloud fraction to reduce when the atmosphere is made drier. The results confirm our expectation. Consequently the massflux is strongly dependent on the atmospheric humidity. Interesting for parameterization we have briefly introduced the fraction of downward moving cloud parcels versus the total number of cloud parcels. This ratio is given in figure 5.5(b). Another interesting issue that may be incorporated in parameterizations is the relation RH versus σ. In figure 6.1 a scatter plot combining figures 4.8(b) and 4.15(b) show how these two quantities are related

6.2   Recommendations

Buoyancy is the cloud's engine and the buoyancy flux is the fuel supply to that engine. It is therefore desirable to parameterize this flux in large scale models. Grant and Lock (2004) tried to do so using CAPE as one factor. According to our results the cloud dynamics, including CAPE, are affected by the atmospheric humidity. The buoyancy flux also depends on the cloud fraction, which is not incorporated in the scaling proposed by Grant and Lock. We still do not understand why the scaling works well for the simulations that they carried out.; the atmospheric relative humidity should be incorporated in the
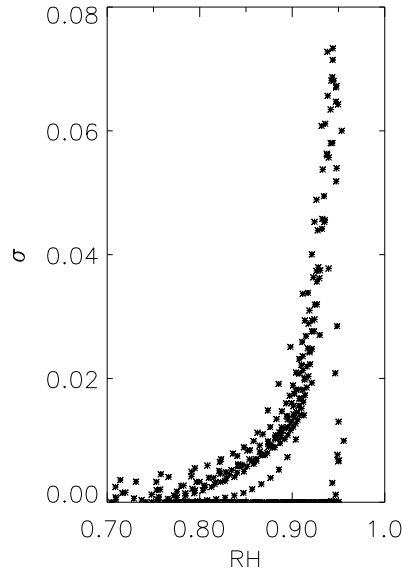
Figure 6.1: Scatter plot of *RH* versus σ for *all* simulations.

scaling.

In all our experiments we have used BOMEX as the reference state. The mean virtual potential temperature profile is such that the BOMEX case evolves to a steady state (Siebesma and Cuijpers, 1995), and we have found that with time our experiments migrate toward the BOMEX case. It would therefore be interesting to do the same research for some other virtual potential temperature profiles, not necessarily evolving to a steady state.

Appendix A

Thermodynamics

This appendix aims at introducing the thermodynamical equations as well as defining the variables used in investigation of cumulus convection. We will introduce the liquid water potential temperature and virtual potential temperature, θ_l and θ_v respectively, both important when describing a rising thermal. Specific humidities like total water content, q_t, and water vapor content, q_v are essential. The potential temperatures and specific humidities are important quantities in describing phase change, which inevitably drives the cumulus convection.

Before discussing the thermodynamical laws we first have to introduce the meaning of an *intensive* variable, an *extensive* variable and a *specific* variable: An intensive variable is one whose value does not depend on the amount of matter in the system. An extensive variable, on the other hand, depends on the size of the system. To obtain an intensive variable from an extensive one, simply divide the extensive variable by the mass. A specific variable is the same as an intensive variable; both terminologies will be used.

A *system* is a finite amount of material separated from its environment. Sometimes the system is simply an air particle. A system is described by a set of *thermodynamical coordinates*. Temperature, volume and pressure are examples of such thermodynamical coordinates.

A.1 A dry approach, the equation of state

The state diagram introduced above is constructed by the equation of state. If the state can be described by the thermodynamical coordinates $x_1, x_2, \cdots, x_n$ then the equation of state, f, reads

$$f(x_1, x_2, \cdots, x_n) = 0 \quad .$$

Its differential is then given by

$$\mathrm{d}f = \left(\frac{\partial f}{\partial x_1}\right)_{x_2,x_3\cdots,x_n} dx_1 + \left(\frac{\partial f}{\partial x_2}\right)_{x_1,x_3\cdots,x_n} dx_2 + \cdots + \left(\frac{\partial f}{\partial x_n}\right)_{x_1,x_2,x_3\cdots,x_{n-1}} dx_n \quad .$$

The subscripts indicate that those variables are kept constant under differentiation.
The atmosphere consists of nitrogene (75.5%), oxygene (23.2%), some carbondioxide (<1%) and other constituents like water vapor. This mixture resembles an ideal gas, which obeys the *ideal gas law*:

$$pV = \nu R^* T \quad .$$

Reading from left to right, the variables are pressure, (extensive) volume, number of moles of gas, $R^* = 8.341$ J mol^{-1}K^{-1} the universal gas constant and temperature, respectively. On intensive form, the gas law for *dry air*, i.e. no moisture, reads

$$p = \rho R_d T \quad . \tag{A.1}$$

Here $R_d = 287.05$ J kg^{-1}K^{-1} is the gas constant for dry air. The ideal gas law is an example of the equation of state. A more detailed discussion on the gas constant is found in Bohren and Albrecht (1998).

A.2 The first law of thermodynamics, heat capacity and enthalpy

The first law of thermodynamics relates the internal energy of a medium to the heat added and work performed by the medium. Using intensive variables where u and q denote internal energy and heat, respectively, the first law reads on differential form:

$$\mathrm{d}u = \mathrm{d}q - p\mathrm{d}v \quad . \tag{A.2}$$

The last term on the right hand side denotes the work performed by the system on its environment. If we let the internal energy be a function of temperature and volume, i.e. $u = u(v,T)$, then we can express the differential of u as

$$\mathrm{d}u = \left(\frac{\partial u}{\partial v}\right)_T \mathrm{d}v + \left(\frac{\partial u}{\partial T}\right)_v \mathrm{d}T \quad .$$

It can be shown that an ideal gas does not depend on its volume, i.e. $\partial u/\partial v = 0$ (e.g. Bohren and Albrecht, 1998), hence a comparison of the latter equation with equation (A.2) reveals that

$$\mathrm{d}q = \left(\frac{\partial u}{\partial T}\right)_v \mathrm{d}T + p\mathrm{d}v \quad .$$

The first term on the right hand side defines the specific heat capacity at constant volume

$$c_v \equiv \left(\frac{\partial u}{\partial T}\right)_v \quad . \tag{A.3}$$

This quantity specifies how much energy must be added to warm up one kilogram of air by one Kelvin when the system is kept at constant volume. A process in which the volume is constant is called an isometric process.

In a similar way, we introduce the specific heat capacity for an isobar process, i.e. $dp = 0$. In order to do so, we introduce the enthalpy, h, which is defined as

$$h = u + pv \quad . \tag{A.4}$$

Using this definition, the first law of thermodynamics can be written

$$\mathrm{d}u = \mathrm{d}q - \mathrm{d}(pv) + v\mathrm{d}p \Rightarrow \mathrm{d}(u + pv) = \mathrm{d}q + v\mathrm{d}p \Rightarrow \mathrm{d}h = \mathrm{d}q + v\mathrm{d}p \quad . \tag{A.5}$$

With the enthalpy the specific heat capacity of an isobaric process is defined as

$$c_p \equiv \left(\frac{\partial h}{\partial T}\right)_p \quad . \tag{A.6}$$

It can furthermore be shown that the two specific heat capacities for dry air are related through

$$c_p = c_v + R_d \quad .$$

Holton (1992) gives a physical interpretation of the enthalpy.

A.3 Entropy, the second law of thermodynamics and potential temperature

We have now come to the introduction of a crucial quantity called *entropy*, which is defined as

$$\mathrm{d}s = \mathrm{d}q/T \quad . \tag{A.7}$$

Let a system go from one state to another. The change of entropy depends on the initial and final state only, i.e. how the system got from the initial to the final state is unimportant. Thus we do not speak about entropy in one state or another, rather about changes in entropy. If the change in entropy after a process is zero, the process is said to be isentropic, i.e. $\mathrm{d}s = 0$. An adiabatic process is one in which the system does not exchange heat with

its surroundings, i.e. $\mathrm{d}q = 0$. It can be shown that the change in entropy can only be positive or zero, i.e. $\Delta s \geq 0$. This is what makes entropy useful; if a process results in a negative entropy change, then the process cannot take place. Equivalently, the process would violate the second law of thermodynamics.

Loosely speaking, *the second law of thermodynamics* states that energy cannot go from a low quality state to a high quality state by itself. In mathematical terms, this law can be derived by using the first law of thermodynamics and the entropy

$$\mathrm{d}u = \mathrm{d}q - p\mathrm{d}v \Rightarrow \mathrm{d}u = T\mathrm{d}s - p\mathrm{d}v \quad .$$

Finally, we incorporate the 'legality' of the process, i.e. the change of entropy cannot be negative

$$T\mathrm{d}s = \mathrm{d}u + p\mathrm{d}v \geq 0 \quad . \tag{A.8}$$

We start the introduction of the *potential temperature* with a short physical description. Picture a particle with temperature T at an arbitrary height. The potential temperature, θ, of the particle is the temperature the particle would have if we adiabatically (i.e. without heat exchange with the environment) displaced it downward to the surface. The pressure near the surface is denoted by reference pressure, p_0, often ascribed the value 1000 hPa.

Our starting point for deriving a mathematical expression for the potential temperature is the first law of thermodynamics (A.5). Since we assume no heat exchange with the surroundings, we have $\mathrm{d}q = 0$. Furthermore we will use $\mathrm{d}h = (\partial h/\partial T)_p \mathrm{d}T \equiv c_p \mathrm{d}T$ and divide equation (A.5) by T and utilize equation (A.1) to obtain

$$\frac{c_p}{T}\mathrm{d}T = \frac{R_d}{p}\mathrm{d}p \Rightarrow \mathrm{d}\ln T = \frac{R_d}{c_p}\mathrm{d}\ln p \quad .$$

In the state diagram we integrate from state (T_0, p_0) to (T, p)

$$\frac{T}{T_0} = \left(\frac{p}{p_0}\right)^{R_d/c_p} \Rightarrow Tp^{-R_d/c_p} = T_0 p_0^{-R_d/c_p} \quad .$$

But remember that the potential temperature was the temperature the particle would have at the reference pressure p_0, i.e. $\theta = T_0$. We thus end with

$$\theta = T\left(\frac{p_0}{p}\right)^{R_d/c_p} \quad . \tag{A.9}$$

A.4 Moist variables

So far we have introduced the variables necessary to describe a dry atmosphere. An essential part of the description of cumulus convection is the presence of moisture, which

inevitably leads to phase transformation.

The *water vapor pressure*, usually denoted by e, follows from the gas law

$$e = \rho_v R_v T \tag{A.10}$$

Here ρ_v and R_v are the density of water vapor and the humid gas constant, respectively. If the atmosphere cannot absorb more water vapor without forcing a condensation, it is said to be saturated. Its water vapor pressure is then e_s. The relative humidity $RH = e/e_s$ gives a measure of the actual vapor pressure to the saturated vapor pressure.

If we consider a control volume consisting of water (in any phase) and dry air, we define the ratio of water to dry air as the *mass mixing ratio*. On the other hand, the ratio of water to the total mass is called the *specific humidity*. Their mathematical expressions are given by

$$r_k = \frac{m_k}{m_d} \ , \ q_k = \frac{m_k}{m} \quad , \quad m = m_v + m_l + m_i + m_d \quad . \tag{A.11}$$

where $k \in \{v(\text{vapor}), l(\text{liquid}), i(\text{ice})\}$ and m_d is the of a dry air parcel.

A.5 The Clausius-Clapeyron equation

Water molecules are constantly coursing back and forth between phases; we will only consider the vapor and liquid phases. The rate at which water vapor molecules transfer to liquid water molecules is called the condensation rate. Similarly, the evaporation rate is the rate at which liquid water is transformed to water vapor. As air raises, it becomes colder due to adiabatic expansion and the evaporation rate decreases more rapidly than does the condensation rate, hence there is a net condensation.

Figure A.1 depicts a two dimensional phase diagram showing water in different phases.
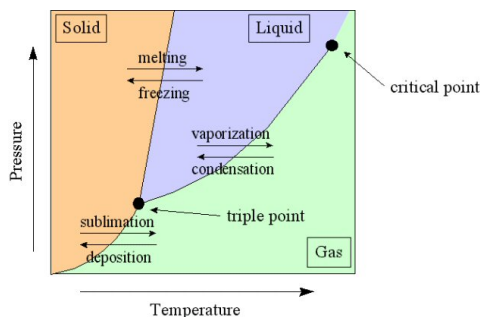

Figure A.1: State diagram for an ideal gas. Taken from Both and Christiansen (1995).

Let us look at a mixture of liquid water and water vapor confined within a cylinder fitted

with a piston which controls the volume of the cylinder; there is no heat exchange with the environment. Figure A.2 shows the phase transformation under an isotherm, four-step process. From 1 to 2 the pressure increases as the volume decreases. At point 2 the
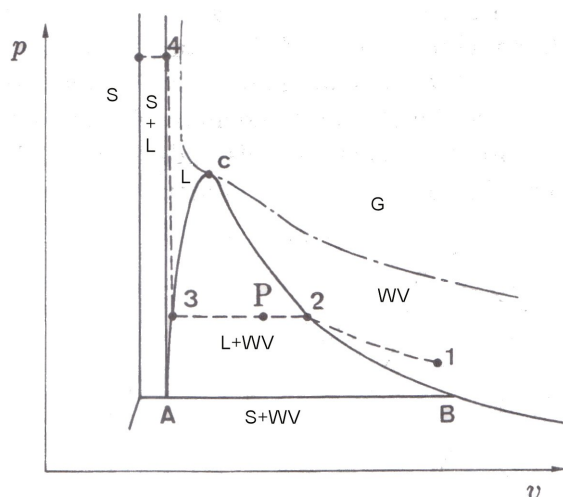
Figure A.2: pv-diagram showing border lines between different phases. S = solid, WV = water vapor, L = liquid and G = gas. Taken from Both and Christiansen (1995)

pressure equals the saturation pressure e_s. The next step, from 2 to 3, there is no change in pressure, rather the decrease in volume enforces a condensation of water vapor to liquid water. In between 2 and 3 both liquid water and saturated vapor is present. Finally arrived at point 3, all water vapor has become liquified. A subsequent volume decrease will result in a pressure increase, step 3 to 4.

The relationship between the temperature of a liquid and its vapor pressure is not a straight line. The vapor pressure of water, for example, increases significantly more rapidly than the temperature of the system. The rate of change of saturated water vapor pressure with respect to temperature (i.e. de_s/dT) determines the coefficient of the border line between vapor and liquid in the phase diagram. A simple way of deriving the Clausius-Clapeyron equation, which relates the pressure change to latent heat released upon condensation, is to start with the Maxwell relations. Following Both and Christiansen (1995), we start by introducing Helmholtz' free energy

$$f = u - Ts \quad .$$

73

With aid of equation (A.7) and the definition for the enthalpy (A.4), equation (A.5) can be written as

$$d(u + pv) = Tds + vdp$$

which after applying the chain rule of differentiation and rearranging reads

$$\mathrm{d}f = \mathrm{d}(u - Ts) = -s\mathrm{d}T - p\mathrm{d}v \quad . \tag{A.12}$$

Compare this expression with the differential of $\mathrm{d}f$ to obtain

$$\mathrm{d}f = \left(\frac{\partial f}{\partial T}\right)_v \mathrm{d}T + \left(\frac{\partial f}{\partial v}\right)_T \mathrm{d}v$$

$$\text{hence} \quad \left(\frac{\partial f}{\partial T}\right)_v \mathrm{d}T = -s \quad \text{and} \quad \left(\frac{\partial f}{\partial v}\right)_T \mathrm{d}v = -p \tag{A.13}$$

Cross-differentiate equation (A.13) and obtain

$$\left(\frac{\partial s}{\partial v}\right)_T = \left(\frac{\partial p}{\partial T}\right)_v \quad . \tag{A.14}$$

The latter equality constitutes one of four Maxwell relations. We can replace the pressure p by the saturated water vapor pressure e_s and since e_s and the temperature are independent of the volume during phase transition, we have $(\partial e_s/\partial T)_v = \mathrm{d}e_s/\mathrm{d}T$. If we choose the volume and temperature as free coordinates for the entropy, we can write

$$\mathrm{d}s = \left(\frac{\partial s}{\partial T}\right)_v \mathrm{d}T + \left(\frac{\partial s}{\partial v}\right)_T \mathrm{d}v \quad .$$

But the process was assumed isotherm, thus the first term on the right hand side drops out. Hence $(\partial s/\partial v)_T = ds/dv$. Combining the latter equation with (A.14) we get

$$\frac{\mathrm{d}s}{\mathrm{d}v} = \frac{\mathrm{d}e_s}{\mathrm{d}T} = \frac{\mathrm{d}q/T}{\mathrm{d}v} \quad .$$

Now use finite differences

$$\frac{de_s}{dT} = \frac{dq}{T(v_v - v_l)} = \frac{\ell_v}{T(v_v - v_l)} \quad , \tag{A.15}$$

where v_v and v_l are the specific volumes of the water vapor and liquid water, respectively. The finite heat $\mathrm{d}q$ is the heat released when vapor condenses, i.e. $\mathrm{d}q = \ell_v$ where $\ell_v = 2.5 \times 10^6\,\mathrm{J/kg}$ is the latent heat of evaporation. The volume of water vapor is much larger than that of liquid water, i.e. $v_v \gg v_l$. In the reminder of the text, we will therefore incorporate that approximation in the Clausius-Clapeyron equation:

$$\frac{\mathrm{d}e_s}{\mathrm{d}T} = \frac{\ell_v}{Tv_v} \quad . \tag{A.16}$$

This is the heat released when water vapor is condensed. It can be shown that the latent heat is related to the enthalpy through

$$\ell_v = h_v - h_l \quad . \tag{A.17}$$

Finally we will introduce an alternative expression for the Clausius-Clapeyron equation by dividing (A.16) by e_s and using equation (A.1)

$$\frac{d \ln e_s}{dT} = \frac{\ell_v}{R_d T^2} \quad . \tag{A.18}$$

A.6   'Wet' temperatures

An important law used to describing the pressure of a mixture of vapor, water and air is Dalton's law. Formally, it states that if a system consist of i constituents having partial pressures p_i, then the the total pressure of the system is $p = \sum_i p_i$. We will use this law to state that the pressure of air containing dry air and vapor (we neglect the effect of liquid water on the total pressure) is

$$p = p_d + e = \rho R_m T = \rho_d R_d T + \rho_v R_v T \quad . \tag{A.19}$$

By using the specific humidity introduced above, we can express the ratio of the density of dry air to the total density as

$$\frac{\rho_d}{\rho} = \frac{m_d}{m_d + m_v + m_l} = 1 - q_v - q_l \quad .$$

By aid of this equation, the gas constant for the mixture R_m can be expressed as

$$R_m = (1 - q_v - q_l) R_d + q_v R_v \quad ,$$

and hence the gas law can be written

$$p = \rho[(1 - q_v - q_l) R_d + q_v R_v] T = \rho R_d T_v \quad ,$$

which defines the *virtual temperature*

$$T_v = \left[1 - (1 - \frac{1}{\epsilon}) q_v - q_l \right] T \quad . \tag{A.20}$$

Here $\epsilon = R_d / R_v \approx 0.622$. Similar to the potential temperature defined above, we have a *virtual potential temperature*, given by

$$\theta_v = T_v \left(\frac{p_0}{p} \right)^{R_d/c_p} \quad . \tag{A.21}$$

The change in entropy for a parcel undergoing phase transformation is the sum of entropy change due to external processes and due to phase changes. This can be written

$$\mathrm{d}s = \frac{1}{m} \sum_i (m_i \mathrm{d}s_i + s_i \mathrm{d}m_i) \quad . \tag{A.22}$$

In deriving the potential temperature, we used the following equation, assuming an isentropic process

$$ds = c_p \mathrm{d}\ln T - R\mathrm{d}\ln p \quad .$$

Note that we have not specified whether we are looking at dry or moist air or liquid water. The first term on the right hand side can for the three phases be written

$$[c_{pd}\frac{m_d}{m} + c_{pv}\frac{m_v}{m} + c_{pl}\frac{m_l}{m}]\mathrm{d}\ln T = [c_{pd}(1 - q_t) + c_{pv}q_v + c_{pl}q_l]\mathrm{d}\ln T \quad .$$

The second term, however, only applies to dry and moist air since liquid water does not obey the ideal gas law, i.e. after omitting non-physical terms the right hand side reads

$$(1 - q_t)R_d\mathrm{d}\ln p_d + q_v R_v \mathrm{d}\ln e \quad .$$

During condensation the energy (heat) release is the latent heat of evaporation times the mass in question, i.e. $\mathrm{d}q = -\ell_v \mathrm{d}q_v$ where the sign indicates that the parcel gains energy since the change in water vapor is negative, $\mathrm{d}q_v < 0$. Thus for the entropy contribution coming from the phase change is $\mathrm{d}s = -\ell_v \mathrm{d}q_v/T$, which we use in (A.22). Then the total change in entropy becomes

$$\begin{aligned} \mathrm{d}s = &[c_{pd}(1 - q_t) + c_{pv}q_v + c_{pl}q_l]\mathrm{d}\ln T \\ &- \left[(1 - q_t)R_d\mathrm{d}\ln p_d + q_v R_v \mathrm{d}\ln e - \frac{\ell_v}{T}\mathrm{d}q_v\right] \quad . \end{aligned} \tag{A.23}$$

If we use the Clausius-Clapeyron equation (A.18) and

$$\frac{\mathrm{d}\ell_v}{\mathrm{d}T} = \frac{\mathrm{d}}{\mathrm{d}T}(h_v - h_l) = c_{pv} - c_{pl}$$

and introduce the following short-hand notation

$$\tilde{c}_p = c_{pd}(1 + q_t(c_{pl}/c_{pd} - 1)) \quad \text{and} \quad \tilde{R}_d = (1 - q_t)R_d \quad ,$$

we get for (A.22)

$$\mathrm{d}s = \tilde{c}_p \mathrm{d}\ln T - \tilde{R}_d \mathrm{d}\ln p_d + \mathrm{d}(\frac{\ell_v q_v}{T}) - q_v R_v \mathrm{d}\ln(e/e_s) \quad . \tag{A.24}$$

If we integrate this equation from a reference state ($p = 0$, $q_v = 0$, $q_l = q_t$) we obtain the *wet equivalent potential temperature*

$$\theta_q = T\left(\frac{p}{p_0}\right)^{-\tilde{R}_d/\tilde{c}_{pd}} e^{L_1 q_v/(T\tilde{c}_p)}$$

$$L_1 = \ell_v - R_v T \ln\frac{e}{e_s} \quad .$$

For a dry parcel the wet equivalent potential temperature reduces to the potential temperature. This potential temperature can be interpreted as the temperature an air parcel would have if isentropically transformed to a parcel having reference pressure and zero water vapor. θ_q is constant during isentropic transformation even when it involves phase changes, except when droplets enter or leave the parcel.

The saturated equivalent potential temperature can be further simplified by realizing that q_v, q_l and q_t are small quantities. They are all of order 10^{-2}, thus $\tilde{R}_d \approx R_d$, $\tilde{c}_{pd} \approx c_{pd}$ and the exponent is approximated as follows

$$\exp\left[\frac{L_1 q_v}{T c_{pd}}\right] \approx 1 + \frac{L_1 q_v}{T c_{pd}} = 1 + \frac{(\ell_v - R_v T \ln\frac{e}{e_s})q_v}{T c_{pd}}$$

$$\approx 1 + \frac{\ell_v q_v}{T c_{pd}}$$

The resulting *equivalent potential temperature* then becomes

$$\theta_e = \theta + \frac{\ell_v q_v}{\Pi c_{pd}} \quad , \quad \Pi = \theta/T \quad , \tag{A.25}$$

where Π is called the Exner function. Finally we introduce the *liquid potential temperature* θ_l, which is given by

$$\theta_l = \theta - \frac{\ell_v q_l}{\Pi c_{pd}} \quad . \tag{A.26}$$

This quantity is used in the LES model. Note that $\theta_e \approx \theta_l + \ell_v q_t/(c_{pd}\Pi)$

Appendix B

The governing equations

It is now time to use the variables introduced in appendix A in some equations. First we will look at the equations without imposing any approximations. Thereafter the Boussinesq approximation is applied and finally we will look at the equations after filtering. Filtering is the process in which we distinguish between resolved and subgrid scales.

B.1 The unfiltered equations

The *momentum equation* is given by the Navier-Stokes equations:

$$\underbrace{\frac{\mathrm{d}u_i}{\mathrm{d}t}}_{\text{Acceleration}} = \underbrace{-\frac{1}{\rho}\frac{\partial p}{\partial x_i}}_{\text{Pressure gradient}} - \underbrace{g\delta_{i3}}_{\text{Gravity}} - \underbrace{2\epsilon_{ijk}\Omega_j u_k}_{\text{Coriolis force}} + \underbrace{\nu_M \frac{\partial^2 u_i}{\partial x_j^2}}_{\text{Molecular diffusion}} \tag{B.1}$$

The left hand side tells us that the rate of change of velocity, i.e. acceleration, viewed by an observer following the particle, is given by the terms on the right. This description is called the Lagrangian description. However, making measurements at one location is much easier, thus we want a description which allows us to stay foot and not move with the particle. The Eulerian description is such an approach. The left hand side is the only one to change:

$$\frac{\mathrm{d}u_i}{\mathrm{d}t} = \underbrace{\frac{\partial u_i}{\partial t}}_{\text{Local acceleration}} + \underbrace{u_j \frac{\partial u_i}{\partial x_j}}_{\text{Advection}}$$

In absence of other forces, the pressure gradient force ensures that particles are accelerated from high pressure to low pressure. The earth pulls at each particle, and at the same time the centrifugal force tries to throw the same particle out into space. The sum of the latter two forces are combined into the gravitation term, which only works in the direction

perpendicular to the earth's surface. Due to the earth's rotation about its own axis, a 'fictive' force must be included in order to describe motion in a inertial coordinate system. $\Omega = 7.292 \cdot 10^{-5} \mathrm{s}^{-1}$ is the angular velocity of the earth. The last term on the right hand side of (B.1) describes dissipation due to molecular interaction between molecules; ν_M is the molecular kinematic viscosity coefficient.

The *continity equation* relates the inflow and outflow into a volume to the time rate of change of density:

$$\frac{\partial \rho}{\partial t} + u_j \frac{\partial \rho}{\partial x_j} = -\rho \frac{\partial u_j}{\partial x_j} \quad . \tag{B.2}$$

The *thermodynamic energy equation* is given by

$$\frac{\partial (c_p \theta)}{\partial t} + u_j \frac{\partial (c_p \theta)}{\partial x_j} = \underbrace{\nu_T \frac{\partial^2 (c_p \theta)}{\partial x_j^2}}_{\text{Molecular diffusion}} + \overbrace{\frac{1}{\rho} \frac{\partial R_j}{\partial x_j}}^{\text{Radiative transfer}} - \underbrace{\ell_v M}_{\text{Phase change}} \quad , \tag{B.3}$$

ν_T is the molecular kinematic viscosity coefficient and R the incoming radiation per unit area. Under phase change energy will be freed / absorbed, e.g. a water droplet needs to absorb energy in order to condense. In general circulation theory, radiation and phase change terms are often included in a broader source term, e.g. Holton (1992).

Lastly we will introduce the conservation law for water:

$$\frac{\partial q_t}{\partial t} + u_j \frac{\partial q_t}{\partial x_j} = \nu_q \frac{\partial^2 q_t}{\partial x_j^2} + S_{q_t} \quad . \tag{B.4}$$

On the right hand side the first term represents molecular diffusivity and the last term represents sources and sinks such as precipitation.

B.2 Boussinesq approximation

Across the lowest kilometer of the atmosphere the density varies only about 10% and the fluctuating component of density deviates from the basic state by only a few percent. However, setting the density constant should be avoided since density fluctuations are responsible for buoyancy forces. This forms the basis of the Boussinesq approximation; the density is kept constant in all terms except for the buoyancy term in the vertical momentum equation. We introduce a mean atmosphere (the whole layer) with density ρ_0 and fluctuations ρ'. Density can be translated to pressure, which in we will write as $p_0(z) + p$. The mean atmosphere has a corresponding mean virtual potential temperature

$\theta_{v,0}$. The continuity equation for a fluid with constant density becomes

$$\frac{\partial u_i}{\partial x_i} = 0 \quad .$$

(B.5)

With the approximation

$$\frac{\rho'}{\rho_0} = -\frac{\theta_v - \theta_{v,0}}{\theta_{v,0}}$$

(see van Dop (2004)) and hydrostatic balance, $\partial p_0 / \partial z = -\rho_0 g$, we obtain the following form of the momentum equation

$$\frac{\partial u_i}{\partial t} + \frac{\partial(u_j u_i)}{\partial x_j} = \frac{\theta_v - \theta_{v,0}}{\theta_{v,0}} g \delta_{ij} - \frac{1}{\rho_0}\frac{\partial p}{\partial x_i} + \nu_M \frac{\partial^2 u_i}{\partial x_j^2} \quad .$$

(B.6)

On comparison with equation (B.1) we see that the Coriolis force has been omitted. This is justified since the processes we investigate are rapid processes compared to the revolution of the earth. Under the Boussinesq approximation the thermodynamic energy equation (B.3) is linearized to :

$$\frac{\partial \theta}{\partial t} + \frac{\partial(u_j \theta)}{\partial x_j} = S_\theta \quad ,$$

(B.7)

where S_θ is a general source/sink term into which the radiation and the molecular dissipation terms have been absorbed. With aid of (B.5) and the chain rule of differentiation the conservation law for total water content reads

$$\frac{\partial q_t}{\partial t} + \frac{\partial(u_j q_t)}{\partial x_j} = S_q \quad ,$$

(B.8)

where all sink and source terms have been absorbed into the S_q-term.

B.3 Filtered equations

Equations have to be discretized when solved numerically. An xz-surface of a grid is shown in figure B.1. The notation is getting ugly but there is no way around it: resolved quantities are denoted by $\langle \psi \rangle$ and subgrid terms with a double prime ψ'' i.e.

$$\underbrace{\psi}_{\text{True value}} = \underbrace{\langle \psi \rangle}_{\text{Resolved}} + \underbrace{\psi''}_{\text{Subgrid}} \quad .$$

Filtering the Navier-Stokes equation will be explained in detail. The momentum equation under the Boussinesq approximation, is in (B.6) put on conservative form, which with the aid of (e.g. Deardorff, 1973)

$$\left\langle \frac{\partial u_i}{\partial t} \right\rangle = \frac{\partial \langle u_i \rangle}{\partial t} \quad \text{and} \quad \left\langle \frac{\partial u_i}{\partial x_j} \right\rangle = \frac{\partial \langle u_i \rangle}{\partial x_j}$$
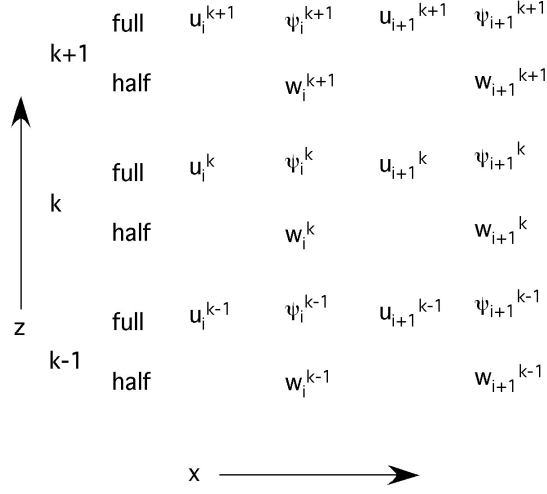
full u_i^{k+1} ψ_i^{k+1} u_{i+1}^{k+1} ψ_{i+1}^{k+1}

k+1

half w_i^{k+1} w_{i+1}^{k+1}

full u_i^{k} ψ_i^{k} u_{i+1}^{k} ψ_{i+1}^{k}

k

half w_i^{k} w_{i+1}^{k}

z

full u_i^{k-1} ψ_i^{k-1} u_{i+1}^{k-1} ψ_{i+1}^{k-1}

k-1

half w_i^{k-1} w_{i+1}^{k-1}

x $\longrightarrow$

Figure B.1:   Example of an equidistant staggered grid as is used in the Dutch LES model.

together with filtering rules

$$\langle\langle u_i\rangle\rangle = \langle u_i\rangle \quad \text{and} \quad \langle u_i''\rangle = 0 \quad,$$

can be rewritten as

$$\frac{\partial(\langle u_i\rangle + u_i'')}{\partial t} + \frac{\partial}{\partial x_j}\left[(\langle u_i\rangle + u_i'')(\langle u_j\rangle + u_j'')\right] =$$
$$-\frac{1}{\rho_0}\frac{\partial(\langle p\rangle + p'')}{\partial x_i} + \frac{g}{\theta_{v,0}}\left(\langle\theta_v\rangle + \theta_v'' - \theta_{v,0}\right)\delta_{i3} + \nu_M\frac{\partial^2(\langle u_i\rangle + u_i'')}{\partial x_j^2} \quad. \tag{B.9}$$

When this equation is filtered we are left with

$$\frac{\partial\langle u_i\rangle}{\partial t} + \frac{\partial}{\partial x_j}\left[\langle u_i\rangle\langle u_j\rangle + \langle u_i'' u_j''\rangle\right] = -\frac{1}{\rho_0}\frac{\partial\langle p\rangle}{\partial x_i} + \frac{g}{\theta_{v,0}}\left(\langle\theta_v\rangle - \theta_{v,0}\right)\delta_{i3} + \nu_m\frac{\partial^2\langle u_i\rangle}{\partial x_j^2} \quad. \tag{B.10}$$

Now make use of $\langle u_i'' u_j''\rangle = \langle u_i u_j\rangle - \langle u_i\rangle\langle u_j\rangle$ and the subgrid stress tensor τ_{ij} and π being the modified pressure:

$$\tau_{ij} = \langle u_i u_j\rangle - \langle u_i\rangle\langle u_j\rangle - \frac{2}{3}\delta_{ij}\langle e\rangle$$
$$\langle e\rangle = \frac{1}{2}\left[\langle u_k u_k\rangle - \langle u_k\rangle\langle u_k\rangle\right] \tag{B.11}$$
$$\langle\pi\rangle = \frac{\langle p\rangle}{\rho_0} + \frac{2}{3}\delta_{ij}\langle e\rangle \quad.$$

With these expressions the resolved prognostic momentum equation can be put on the following form, which in textbooks is the standard notation

$$\frac{\partial \langle u_i \rangle}{\partial t} + \frac{\partial \langle u_i \rangle \langle u_j \rangle}{\partial x_j} = -\frac{\partial \langle \pi \rangle}{\partial x_i} + \frac{g}{\theta_{v,0}}\big(\langle \theta_v \rangle - \theta_{v,0}\big)\delta_{i3} + \nu_M \frac{\partial^2 \langle u_i \rangle}{\partial x_j^2} - \frac{\partial \tau_{ij}}{\partial x_j} \quad . \qquad \text{(B.12)}$$

Note that on the resolved scale with high Reynolds number, which is the case for the atmosphere, there is no molecular dissipation. Energy passed on from the large eddies to smaller eddies is incorporated in the subgrid stress tensor τ_{ij}. For obtaining an expression for the subgrid TKE we will return to the first form, however; subtracting (B.10) from (B.9) yields the tendency equation for the subgrid velocity fluctuation:

$$\frac{\partial u_i''}{\partial t} + \frac{\partial}{\partial x_j}\big[\langle u_i \rangle u_j'' + u_i'' \langle u_j \rangle + u_i'' u_j'' - \langle u_i'' u_j'' \rangle\big] = -\frac{1}{\rho_0}\frac{\partial p''}{\partial x_i} + \frac{g}{\theta_{v,0}}\theta_v''\delta_{i3} + \nu_M \frac{\partial^2 u_i''}{\partial x_j^2} \quad , \text{(B.13)}$$

which we multiply by u_i'' and filter:

$$\left\langle \frac{\partial(\frac{1}{2}u_i''^2)}{\partial t} \right\rangle + \underbrace{\left\langle u_i'' \frac{\partial(\langle u_i \rangle u_j'')}{\partial x_j} \right\rangle}_{A} + \underbrace{\left\langle u_i'' \frac{\partial(u_i'' \langle u_j \rangle)}{\partial x_j} \right\rangle}_{B} + \underbrace{\left\langle u_i'' \frac{\partial(u_i'' u_j'')}{\partial x_j} \right\rangle}_{C} - \underbrace{\left\langle u_i'' \frac{\partial \langle u_i'' u_j'' \rangle}{\partial x_j} \right\rangle}_{D}$$

$$= -\left\langle \frac{u_i''}{\rho_0}\frac{\partial p''}{\partial x_i} \right\rangle + \left\langle \frac{g}{\theta_{v,0}}\theta_v'' u_i'' \delta_{i3} \right\rangle + \underbrace{\left\langle u_i'' \nu_M \frac{\partial^2 u_i''}{\partial x_j^2} \right\rangle}_{E} \quad \text{(B.14)}$$

Terms A-E can by aid of the chain rule of differentiation recast on the form

$$\text{A:} \quad \left\langle u_i'' \frac{\partial(\langle u_i \rangle u_j'')}{\partial x_j} \right\rangle = \left\langle u_i'' u_j'' \frac{\partial \langle u_i \rangle}{\partial x_j} + u_i'' \langle u_i \rangle \frac{\partial u_j''}{\partial x_j} \right\rangle = \langle u_i'' u_j'' \rangle \frac{\partial \langle u_i \rangle}{\partial x_j}$$

$$\text{B:} \quad \left\langle u_i'' \frac{\partial(u_i'' \langle u_j \rangle)}{\partial x_j} \right\rangle = \left\langle u_i''^2 \frac{\partial \langle u_j \rangle}{\partial x_j} \right\rangle + \left\langle u_i'' \langle u_j \rangle \frac{\partial u_i''}{\partial x_j} \right\rangle = \langle u_j \rangle \frac{\partial \langle \frac{1}{2}u_i''^2 \rangle}{\partial x_j}$$

$$\text{C:} \quad \left\langle u_i'' \frac{\partial(u_i'' u_j'')}{\partial x_j} \right\rangle = \left\langle u_i'' u_i'' \frac{\partial u_j''}{\partial x_j} \right\rangle + \left\langle u_i'' u_j'' \frac{\partial u_i''}{\partial x_j} \right\rangle = \frac{1}{2}\frac{\partial}{\partial x_j}\langle u_i'' u_j'' u_i'' \rangle$$

$$\text{D:} \quad \left\langle u_i'' \frac{\partial \langle u_i'' u_j'' \rangle}{\partial x_j} \right\rangle = \langle u_i'' \rangle \frac{\partial \langle u_i'' u_j'' \rangle}{\partial x_j} = 0$$

$$\text{E:} \quad \left\langle \nu_M u_i'' \frac{\partial^2 u_i''}{\partial x_j^2} \right\rangle = \left\langle \nu_M \frac{\partial}{\partial x_j}\big(u_i'' \frac{\partial u_i''}{\partial x_j}\big) \right\rangle - \left\langle \nu_M \big(\frac{\partial u_i''}{\partial x_j}\big)^2 \right\rangle$$

Equation (B.14) can thus be written as

$$\frac{\partial \langle \frac{1}{2}u_i''^2 \rangle}{\partial t} + \langle u_j \rangle \frac{\partial \langle \frac{1}{2}u_i''^2 \rangle}{\partial x_j} = -\langle u_i'' u_j'' \rangle \frac{\partial \langle u_i \rangle}{\partial x_j} - \left\langle \frac{u_i''}{\rho_0}\frac{\partial p''}{\partial x_i} \right\rangle - \frac{1}{2}\frac{\partial}{\partial x_j}\langle u_i'' u_j'' u_i'' \rangle$$

$$+ \frac{g\delta_{i3}}{\theta_{v,0}}\langle \theta_v'' u_i'' \rangle + \left\langle \nu_M \frac{\partial}{\partial x_j}\big(u_i'' \frac{\partial u_i''}{\partial x_j}\big) \right\rangle - \left\langle \nu_M \big(\frac{\partial u_i''}{\partial x_j}\big)^2 \right\rangle \quad . \quad \text{(B.15)}$$

We now introduce the definition for the subgrid TKE; $\langle e \rangle = \langle \frac{1}{2} u_i''^2 \rangle$ and rearrange. Furthermore, in order to use the subgrid stress tensor τ_{ij} we will subtract $(2/3)\delta_{ij}\langle e \rangle$ in the shear production term. This is allowed since $\delta_{ij}\langle e \rangle \partial \langle u_i \rangle / \partial x_j = \langle e \rangle \partial \langle u_j \rangle / \partial x_j = 0$. We get

$$\underbrace{\frac{\partial \langle e \rangle}{\partial t}}_{\text{Tendency}} + \underbrace{\langle u_j \rangle \frac{\partial \langle e \rangle}{\partial x_j}}_{\text{Resolved advection}} = \frac{g}{\theta_{v,0}} \langle \theta_v'' u_i'' \rangle \delta_{i3} \text{ Production/consumption due to buoyancy}$$

$$- [\langle u_i'' u_j'' \rangle - \frac{2}{3}\delta_{ij}\langle e \rangle]\frac{\partial \langle u_i \rangle}{\partial x_j} \text{ Shear production/consumption}$$

$$- \frac{\partial}{\partial x_j}\left[\frac{1}{2}\langle u_i'' u_j'' u_i'' \rangle\right] \text{ Redistribution of subgrid TKE}$$

$$- \frac{1}{\rho_0}\frac{\partial \langle p'' u_i'' \rangle}{\partial x_i} \text{ Redistribution of subgrid TKE by pressure fluctuations}$$

$$+ \frac{\partial}{\partial x_j}\left[\nu_M \left\langle u_i'' \frac{\partial u_i''}{\partial x_j} \right\rangle\right] - \nu_M \left\langle \left(\frac{\partial u_i''}{\partial x_j}\right)^2 \right\rangle \text{ Dissipation} \qquad .$$

We have also applied the chain rule of differentiation to the forth term on the right hand side. The shear production / consumption term can be written (see equation (B.11)) as $-[\langle u_i'' u_j'' \rangle - \frac{2}{3}\delta_{ij}\langle e \rangle]\frac{\partial \langle u_i \rangle}{\partial x_j} = -\tau_{ij}\frac{\partial \langle u_i \rangle}{\partial x_j}$. This term is the connection between resolved and subgrid motion. At the smallest scales, molecular diffusion is responsible for loss of energy. In the final result we therefore replace the two molecular dissipation terms with a general dissipation term ε

$$\frac{\partial \langle e \rangle}{\partial t} + \langle u_j \rangle \frac{\partial \langle e \rangle}{\partial x_j}$$

$$= \frac{g}{\theta_{v,0}}\langle \theta_v'' u_i'' \rangle \delta_{i3} - \tau_{ij}\frac{\partial \langle u_i \rangle}{\partial x_j} - \frac{\partial}{\partial x_j}\left[\frac{1}{2}\langle u_i'' u_j'' u_i'' \rangle\right] \qquad \text{(B.16)}$$

$$- \frac{1}{\rho_0}\frac{\partial \langle p'' u_i'' \rangle}{\partial x_i} - \varepsilon \qquad .$$

The filtered continuity equation becomes

$$\frac{\partial \langle u_i \rangle}{\partial x_i} = 0 \qquad . \qquad \text{(B.17)}$$

Lastly we will turn our attention to the filtered versions of the conservations laws (B.7) and (B.8). They both involve the same terms and for convenience we will express these equations with a general variable $\psi \in \{\theta_l, q_t\}$. On filtered form they become

$$\frac{\partial \langle \psi \rangle}{\partial t} + \frac{\partial (\langle u_j \rangle \langle \psi \rangle)}{\partial x_j} = \langle S_\psi \rangle \qquad . \qquad \text{(B.18)}$$

Appendix C

Decomposition and notation

C.1 Decompositions

In order to plot quantities such as cloud cover, we have to tell the computer which grid point are cloud points. There are different ways of sampling cloud points; a summary is given in table C.1. The choice of criteria depends on the matter being investigated; if bulk vertical transport inside a cloud is under investigation it is reasonable to apply the core decomposition ($q_l > 0$, $w > 0$ and $\theta_{v,c} > \overline{\theta_v}$) since the cloud core is responsible for most of the transport, whereas for radiation issues the presence of cloud droplets is more important and then the cloud decomposition ($q_l > 0$) is more reasonable

Decomposition	Criteria
Updraft	$w > 0$
Cloud	$q_l > 0$
Cloud updraft	$q_l > 0$ and $w > 0$
Cloud downdraft	$q_l > 0$ and $w < 0$
Cloud core	$q_l > 0$ and $w > 0$ and $\theta_{v,c} > \overline{\theta_v}$

Table C.1: When sampling, all grid points are tested against these criteria to determine if they are cloud-, updraft- or core points.

C.2 Symbols

Short	Mathematical notation	Description
CAPE	A	Convective Available Potential Energy
CIN		Convective Inhibition
CRM		Cloud Resolving Model
DNS		Direct Numerical Simulation
GCM		General Circulation Model
ITCZ		Intertropical Convergence Zone
LCL		Lifting condensation level
LES		Large Eddy Simulation
LFC		Level of free convection
LNB		Level of neutral buoyancy
LOC		Limit of convection
SCM		Single Column Model
TKE		Turbulent Kinetic Energy
	c_p, c_v	Heat capacity and constant pressure / volume
	p	Pressure
	q_t, q_l, q_v	Total and liquid water content, water vapor content
	M_c	Cloud mass flux
	M_b	Mass flux at cloud base
	R_d, R_v	Dry and wet gas constant
	RH	Relative humidity
	$\vec{u}$	Velocity vector
	θ	Potential temperature
	θ_v	Virtual potential temperature
	θ_l	Liquid potential temperature
	ψ_c	In-cloud mean of property ψ
	ψ_{env}	Environmental mean of property ψ

Table C.2: Notation used in text

Bibliography

Arakawa, A. and Schubert, W. H. 1974. Interaction of a cumulus cloud ensemble with the large-scale environment: textscP i. *J. Atmos. Sci.*, **31**, 674–701.

Bohren, C. F. and Albrecht, B. A. 1998. *Atmospheric Thermodynamics*. Oxford University Press. 402 pp.

Both, E. and Christiansen, G. 1995. *Termodynamik*. Den private Ingenioersfond, Danmarks Tekniske Universitet, third edition.

Bretherton, C. S., McCaa, J. R., and Grenier, H. 2003. A new parameterization for Shallow Cumulus Convection and its application to marine subtropical cloud-topped boundary layers. Part 1, Description and 1D results. *Mon. Weather Rev.*, **132**, 864–882.

Carter, L. J. 1969. Project bomex: Biggest weather study yet. *Science*, **1163**, 1435–1436.

Deardorff, J. W. 1973. Three-dimensional numerical modeling of the planetary boundary layer. In D. A. Haugen, editor, *Workshop on Micrometeorology*, pages 271–311. Amer. Met. Soc. Boston.

Derbyshire, S. H., Beau, I., Bechtold, P., Grandpeix, J. Y., Piriou, J. M., Redelsperger, J. L., and Soares, P. M. M. 2004. Sensitivity of moist convection to environmental humidity. *Q. J. R. Meteorol. Soc.*, **128**, 1–26.

Durran, D. R. 1998. *Numerical methods for wave equations in geophysical fluid dynamics*. New York:Springer, 1 edition. 465 pp.

Grant, A. L. M. and Brown, A. R. 1999. A similarity hypothesis for shallow-cumulus transports. *Q. J. R. Meteorol. Soc.*, **125**, 1913–1936.

Grant, A. L. M. and Lock, A. P. 2004. The turbulent kinetic energy budget for shallow cumulus convection. *Q. J. R. Meteorol. Soc.*, **130**, 401–422.

Gregory, D. 2001. Estimation of entrainment rate in simple models of convective clouds. *Q. J. R. Meteorol. Soc.*, **127**, 53–72.

Holland, J. Z. and Rasmusson, E. 1973. Measurements of the atmospheric mass energy and momentum budgets over a 500 kilometer square of tropical ocean. *Mon. Weather Rev.*, **101**, 44–55.

Holton, J. R. 1992. *An Introduction to Dynamic Meteorology*. Academic Press. 511 pp.

Houze, R. A. 1993. *Cloud Dynamics*. Academic Press, New York. 573 pp.

Houze, R. A., Hobbs, P. V., and Locatelli, J. D. 1976. Dynamics and cloud microphysics of the rainbands in an occluded frontal system. *J. Atmos. Sci.*, **35**, 1921–1936.

Johnson, R. H., Rickenback, R. M., Rutledge, S. A., Ciesielski, P. E., and Schubert, W. H. 1999. Trimodal characteristics of tropical convection. *J. Climate*, **12**, 2397–2418.

Nitta, T. and Esbensen, S. 1974. Heat and moisture budgets using bomex data. *Mon. Weather Rev.*, **102**, 17–28.

Norris, J. R. 1999. On trends and possible artifacts in global ocean cloud cover between 1952 and 1995. *J. Climate*, **12**, 1864–1870.

Paluch, I. R. 1979. The entrainment mechanism in colorado cumuli. *J. Atmos. Sci.*, **36**, 2467–2478.

Raga, G. B., Jensen, J. B., and Baker, M. B. 1990. Characteristics of cumulus band clouds off the coast of Hawaii. *J. Atmos. Sci.*, **47**, 338–355.

Rodts, S. M. A. 2001. *Shallow cumulus dynamics: Observations and parameterization*. Master's thesis, Utrecht University, Utrecht, 78 pp (Available from Utrecht University, Utrecht, The Netherlands).

Salby, M. L. 1996. *Fundamentals of Atmospheric Physics*. Academic Press, first edition edition. 627 pp.

Siebesma, A. P. 1997. On the mass flux approach for atmosphericconvection. pages unknown–unknown.

Siebesma, A. P. 1998. Shallow cumulus convection. In E. J. Plate, E. E. Fedorovich, D. X. Viegas, and J. C. Wyngaard, editors, *Buoyant Convection in Geophysical Flows*, volume 513, pages 441–486. Kluwer Academic Publishers.

Siebesma, A. P. and Cuijpers, J. W. M. 1995. Evaluation of parametric assumptions for shallow cumulus convection. *J. Atmos. Sci.*, **52**, 650–666.

Siebesma, A. P. and Holtslag, A. A. M. 1996. Model impacts of entrainment and detrainment rates in shallow cumulus convection. *J. Atmos. Sci.*, **53**, 2354–2364.

Siebesma, A. P., Bretherton, C. S., Brown, A., Chlond, A., Cuxart, J., Duynkerke, P. G., Jiang, H., Khairoutdinov, M., Lewellen, D., Moeng, C.-H., Sanchez, E., Stevens, B., and Stevens, D. E. 2003. A large eddy simulation intercomparison study of shallow cumulus convection. *J. Atmos. Sci.*, **60**, 1201–1219.

Siebesma, A. P., Jakob, C., and Co-authors 2004. Cloud representation in general circulation models over the northern pacific ocean: A EUROCS intercomparison study. *Q. J. R. Meteorol. Soc.* submitted for the EUROCS special issue.

Tiedtke, M. 1989. A comprehensive mass flux scheme for cumulus parameterization in large-scale models. *Mon. Weather Rev.*, **177**, 1779–1800.

van Dop, H. 2004. *Grenslaag Meteorologie.* Universiteit Utrecht. Lecture Notes, 72pp.

VanZanten, M. C. 2000. *Entrainment processes in stratocumulus.* Ph.D. thesis, Utrecht University, Utrecht, 139 pp (Available from Utrecht University, Utrecht, The Netherlands).